

Wireless Communications and Mobile Computing

# Advanced Wireless Technology for Ultrahigh Data Rate Communication

Lead Guest Editor: In-Ho Lee

Guest Editors: Jung-Bin Kim, Haejoon Jung, Seok-Chul Kwon,  
and Ernest Kurniawan





---

# **Advanced Wireless Technology for Ultrahigh Data Rate Communication**

Wireless Communications and Mobile Computing

---

# **Advanced Wireless Technology for Ultrahigh Data Rate Communication**

Lead Guest Editor: In-Ho Lee

Guest Editors: Jung-Bin Kim, Haejoon Jung, Seok-Chul Kwon,  
and Ernest Kurniawan



---

Copyright © 2019 Hindawi. All rights reserved.

This is a special issue published in “Wireless Communications and Mobile Computing.” All articles are open access articles distributed under the Creative Commons Attribution License, which permits unrestricted use, distribution, and reproduction in any medium, provided the original work is properly cited.

## Editorial Board

Javier Aguiar, Spain  
Ghufran Ahmed, Pakistan  
Wessam Ajib, Canada  
Muhammad Alam, China  
Eva Antonino-Daviu, Spain  
Shlomi Arnon, Israel  
Leyre Azpilicueta, Mexico  
Paolo Barsocchi, Italy  
Alessandro Bazzi, Italy  
Zdenek Becvar, Czech Republic  
Francesco Benedetto, Italy  
Olivier Berder, France  
Ana M. Bernardos, Spain  
Mauro Biagi, Italy  
Dario Bruneo, Italy  
Jun Cai, Canada  
Zhipeng Cai, USA  
Claudia Campolo, Italy  
Gerardo Canfora, Italy  
Rolando Carrasco, UK  
Vicente Casares-Giner, Spain  
Luis Castedo, Spain  
Ioannis Chatzigiannakis, Italy  
Lin Chen, France  
Yu Chen, USA  
Hui Cheng, UK  
Ernestina Cianca, Italy  
Riccardo Colella, Italy  
Mario Collotta, Italy  
Massimo Condoluci, Sweden  
Daniel G. Costa, Brazil  
Bernard Cousin, France  
Telmo Reis Cunha, Portugal  
Igor Curcio, Finland  
Laurie Cuthbert, Macau  
Donatella Darsena, Italy  
Pham Tien Dat, Japan  
André de Almeida, Brazil  
Antonio De Domenico, France  
Antonio de la Oliva, Spain  
Gianluca De Marco, Italy  
Luca De Nardis, Italy  
Liang Dong, USA  
Mohammed El-Hajjar, UK  
Oscar Esparza, Spain  
Maria Fazio, Italy  
Mauro Femminella, Italy  
Manuel Fernandez-Veiga, Spain  
Gianluigi Ferrari, Italy  
Ilario Filippini, Italy  
Jesus Fontecha, Spain  
Luca Foschini, Italy  
A. G. Fragkiadakis, Greece  
Sabrina Gaito, Italy  
Óscar García, Spain  
Manuel García Sánchez, Spain  
L. J. García Villalba, Spain  
José A. García-Naya, Spain  
Miguel Garcia-Pineda, Spain  
A.-J. García-Sánchez, Spain  
Piedad Garrido, Spain  
Vincent Gauthier, France  
Carlo Giannelli, Italy  
Carles Gomez, Spain  
Juan A. Gómez-Pulido, Spain  
Ke Guan, China  
Antonio Guerrieri, Italy  
Daojing He, China  
Paul Honeine, France  
Sergio Ilarri, Spain  
Antonio Jara, Switzerland  
Xiaohong Jiang, Japan  
Minho Jo, Republic of Korea  
Shigeru Kashihara, Japan  
Dimitrios Katsaros, Greece  
Minseok Kim, Japan  
Mario Kolberg, UK  
Nikos Komninos, UK  
Juan A. L. Riquelme, Spain  
Pavlos I. Lazaridis, UK  
Tuan Anh Le, UK  
Xianfu Lei, China  
Hoa Le-Minh, UK  
Jaime Lloret, Spain  
Miguel López-Benítez, UK  
Martín López-Nores, Spain  
Javier D. S. Lorente, Spain  
Tony T. Luo, Singapore  
Maode Ma, Singapore  
Imadeldin Mahgoub, USA  
Pietro Manzoni, Spain  
Álvaro Marco, Spain  
Gustavo Marfia, Italy  
Francisco J. Martinez, Spain  
Davide Mattera, Italy  
Michael McGuire, Canada  
Nathalie Mitton, France  
Klaus Moessner, UK  
Antonella Molinaro, Italy  
Simone Morosi, Italy  
Kumudu S. Munasinghe, Australia  
Enrico Natalizio, France  
Keivan Navaie, UK  
Thomas Newe, Ireland  
Wing Kwan Ng, Australia  
Tuan M. Nguyen, Vietnam  
Petros Nicopolitidis, Greece  
Giovanni Pau, Italy  
Rafael Pérez-Jiménez, Spain  
Matteo Petracca, Italy  
Nada Y. Philip, UK  
Marco Picone, Italy  
Daniele Pinchera, Italy  
Giuseppe Piro, Italy  
Vicent Pla, Spain  
Javier Prieto, Spain  
Rüdiger C. Pryss, Germany  
Sujan Rajbhandari, UK  
Rajib Rana, Australia  
Luca Reggiani, Italy  
Daniel G. Reina, Spain  
Jose Santa, Spain  
Stefano Savazzi, Italy  
Hans Schotten, Germany  
Patrick Seeling, USA  
Muhammad Z. Shakir, UK  
Mohammad Shojafar, Italy  
Giovanni Stea, Italy  
Enrique Stevens-Navarro, Mexico  
Zhou Su, Japan  
Luis Suarez, Russia  
Ville Syrjälä, Finland



---

Hwee Pink Tan, Singapore  
Pierre-Martin Tardif, Canada  
Mauro Tortonesi, Italy  
Federico Tramarin, Italy  
Reza Monir Vaghefi, USA

Juan F. Valenzuela-Valdés, Spain  
Aline C. Viana, France  
Enrico M. Vitucci, Italy  
Honggang Wang, USA  
Jie Yang, USA

Sherali Zeadally, USA  
Jie Zhang, UK  
Meiling Zhu, UK


# Contents

---



## **Advanced Wireless Technology for Ultrahigh Data Rate Communication**

In-Ho Lee , Jung-Bin Kim , Haejoon Jung , Seok-Chul (Sean) Kwon, and Ernest Kurniawan  
Editorial (2 pages), Article ID 9790853, Volume 2019 (2019)


## **Performance Evaluation of IEEE 802.11ad in Evolving Wi-Fi Networks**

Kien Nguyen , Mirza Golam Kibria, Kentaro Ishizu, and Fumihide Kojima  
Research Article (11 pages), Article ID 4089365, Volume 2019 (2019)

## **Outage Analysis of User Pairing Algorithm for Full-Duplex Cellular Networks**

Hyun-Ho Choi  and Wonjong Noh   
Research Article (12 pages), Article ID 4909450, Volume 2019 (2019)


## **Implementation and Field Trials of OFDM-Based Digital Video Broadcasting System in Commercial Broadcasting Network for Multichannel UHD Service**

Sang-Jung Ra, Myung-Sun Baek , Jin-Hyuk Song, Dong-Joon Choi, Joon-Young Jung, and Cheol-Sung Kim  
Research Article (9 pages), Article ID 1649413, Volume 2019 (2019)

## **Robust Shrinkage Range Estimation Algorithms Based on Hampel and Skipped Filters**

Chee-Hyun Park  and Joon-Hyuk Chang   
Research Article (9 pages), Article ID 6592406, Volume 2019 (2019)

## **Spatiotemporal Statistical Channel Model for Indoor Corridor at 14 GHz, 18 GHz, and 22 GHz Bands**

Nicholas O. Oyie  and Thomas J. O. Afullo  
Research Article (10 pages), Article ID 9656029, Volume 2018 (2019)

## **Development and Validation of New Reverberation Chamber for Wireless Devices**

Dong-Uk Sim , Sang Il Kwak, Jong Hwa Kwon, and Seong-Ook Park  
Research Article (12 pages), Article ID 7068601, Volume 2018 (2019)

## Editorial

# Advanced Wireless Technology for Ultrahigh Data Rate Communication

**In-Ho Lee** <sup>1</sup>, **Jung-Bin Kim** <sup>2</sup>, **Haejoon Jung** <sup>3</sup>,  
**Seok-Chul (Sean) Kwon**<sup>4</sup> and **Ernest Kurniawan**<sup>5</sup>

<sup>1</sup>Department of Electrical, Electronic and Control Engineering, Hankyong National University, Anseong 17579, Republic of Korea

<sup>2</sup>Electronics and Telecommunications Research Institute (ETRI), Daejeon 34129, Republic of Korea

<sup>3</sup>Department of Information and Telecommunication Engineering, Incheon National University, Incheon 22012, Republic of Korea

<sup>4</sup>Department of Electrical Engineering, California State University, Long Beach, CA 90840, USA

<sup>5</sup>Agency for Science, Technology and Research (A\*STAR), Singapore 138632

Correspondence should be addressed to Haejoon Jung; [haejoonjung@inu.ac.kr](mailto:haejoonjung@inu.ac.kr)

Received 13 February 2019; Accepted 13 February 2019; Published 4 March 2019

Copyright © 2019 In-Ho Lee et al. This is an open access article distributed under the Creative Commons Attribution License, which permits unrestricted use, distribution, and reproduction in any medium, provided the original work is properly cited.

According to a strong demand for high-speed services in various 5G deployment scenarios, the key performance requirements for IMT-2020 (5G technical specification) have included the peak data rate of 20 Gbps in downlink and 10 Gbps in uplink as well as the user experienced data rate of 100 Mbps in downlink and 50 Mbps in uplink, and then greatly higher target performance can be intuitively expected for beyond-5G. The main challenges to realize such high data rate are to fully exploit the radio resources (e.g., time, frequency, space, power, and polarization), fully cooperate with other transmitters or receivers, and fully utilize microwave and millimeter-wave spectrum. In practice, these challenges may be restricted by the availability of radio resources and collaborative transmitters or receivers, the capability of transceiver, the accuracy of available channel state information, and so on.

For the past decade, attractive wireless technologies have been presented to fulfill high data rate. The representative technologies involve digital/analog beamforming, multihop transmission, coordinated multipoint transmission/reception, nonorthogonal multiple access, massive multiple-input-multiple-output (MIMO), cognitive radio, millimeter-wave, and so on. However, an independent use of these technologies has induced a limit to improvement in achievable data rate, which has encouraged many researchers to focus on combining and optimizing the wireless technologies so as to extremely enhance the data rate. Although numerous

combined technologies for further performance improvement have been proposed up to the present, more innovative combination and optimization should be consistently studied as the target performance for the next-generation communication becomes continuously improved.

Furthermore, the real wireless communication environments, in particular, regarding 5G New Radio and beyond-5G, introduce new practical issues in implementing the combined and optimized wireless technologies as follows: channel estimation capability with the associated reference signal design, transmission/reception collaboration capability, transmitter/receiver complexity, channel state information feedback, MIMO beamforming codebook design, new waveforms, wireless channel characteristics, and so on. Hence, the practical issues in the implementation of technology need to be addressed with the research on advanced wireless technology. In this context, the accepted papers to be published are focused on combining and/or optimizing the wireless technologies to enhance the achievable data rate, covering both theoretical, and implementation aspects.

The first paper “Development and Validation of New Reverberation Chamber for Wireless Devices” by D.-U. Sim *et al.* has proposed a reverberation chamber (RC) structure with new reflectors and mode stirrers for electromagnetic compatibility and wireless terminal measurements. The main parameters for the reflectors and mode stirrers have been determined through a logical approach based on standard



deviation and eigenfrequency shift analysis by 3D simulations. It has been shown that the proposed RC design method is an effective solution to predict the actual measured results, satisfying all of the requirements defined. Consequently, it is expected that the performance of the proposed RC could be a highly effective solution to measure and evaluate the performance of commercial wireless terminals.

The second paper “Spatiotemporal Statistical Channel Model for Indoor Corridor at 14 GHz, 18 GHz, and 22 GHz Bands” by N. O. Oyie and T. J. O. Afullo has proposed a measurement-based channel model considering both delay and angular domains of an indoor corridor channel. For the cluster identification purpose at different frequency bands, a nonparametric Gaussian kernel density estimation (KDE) method is exploited. The authors have proposed a spatiotemporal model assuming dependence in delay and spatial domains and have presented the proposed model under characterization parameters. It has been demonstrated that both clusters and multipath components can be, respectively, estimated by probability density functions following Gaussian and Laplacian fits in the spatial domain for indoor corridor environments.

The third paper “Robust Shrinkage Range Estimation Algorithms Based on Hampel and Skipped Filters” by C.-H. Park and J.-H. Chang has investigated robust shrinkage range estimation algorithms using Hampel filter, skipped filter, PBM, and BS estimators. The concepts of robustness for the Hampel filter and skipped filter have been combined with shrinkage for the positive blind minimax and Bayes shrinkage estimation. The performance of the proposed schemes in terms of the mean square error (MSE) is substantially improved beyond that of conventional median-based shrinkage algorithms. Further, the proposed algorithms can be represented in a closed-form expression, which guarantee lower complexity compared to the iteration-based methods.

The fourth paper “Implementation and Field Trials of OFDM-Based Digital Video Broadcasting System in Commercial Broadcasting Network for Multichannel UHD Service” by S.-J. Ra *et al.* has presented an OFDM-based digital video broadcasting system test platform for multichannel ultrahigh definition (UHD) broadcasting services. Measured by a commercial STB and signal analyzer, the authors have observed that the implemented OFDM-based digital video broadcasting transmitter can achieve the 51.6 Mbps transmission rate for multichannel UHD broadcasting services. Furthermore, the authors have presented received signal spectrum, BER performance, and CNR of 4096QAM related to the performance and physical network status. These test results can better guide OFDM-based digital video broadcasting technology in many countries and the development of a next-generation digital broadcasting system.

The fifth paper “Outage Analysis of User Pairing Algorithm for Full-Duplex Cellular Networks” by H.-H. Choi and W. Noh has delved into a user pairing problem to minimize outage probability and formulated it as a nonconvex optimization problem in a full-duplex (FD) cellular network. The authors have proposed a low-complexity algorithm in a way that the uplink (UL) user reduces its transmit power to satisfy the SINR threshold for minimizing the interuser interference

and the downlink (DL) user with a worse signal quality preferentially selects its UL user who gives less interference for outage minimization. Using stochastic geometry, the performance of the user pairing algorithm has been analyzed. Both simulation and analysis have indicated that the proposed scheme can vastly reduce the interuser interference and enhance the DL outage performance while satisfying the requirement of UL signal-to-interference-plus-noise ratio. Therefore, the results in this paper can be exploited for the protocol design and implementation of the future FD cellular network.

The sixth paper “Performance Evaluation of IEEE 802.11ad in Evolving Wi-Fi Networks” by K. Nguyen *et al.* has presented an experimental study on IEEE 802.11ad links in a typical indoor environment with different network and interference conditions. The measured results have shown that off-the-shelf IEEE 802.11ad hardware can achieve the Gbps-level throughput of the transmission control protocol (TCP) and user datagram protocol (UDP) under the constraints of signal strength, MCSs, and MTUs. In addition, to mitigate the link maintenance issue, they have proposed using MPTCP for a fast switchover between an IEEE 802.11ad to a legacy Wi-Fi link, which has been evaluated through experiments.

## Conflicts of Interest

The guest editorial team declares that they do not have any possible conflicts of interest or private agreement with companies regarding the special issue for Wireless Communications and Mobile Computing.

*In-Ho Lee*  
*Jung-Bin Kim*  
*Haejoon Jung*  
*Seok-Chul (Sean) Kwon*  
*Ernest Kurniawan*

## Research Article

# Performance Evaluation of IEEE 802.11ad in Evolving Wi-Fi Networks

Kien Nguyen <sup>1</sup>, Mirza Golam Kibria,<sup>2</sup> Kentaro Ishizu,<sup>2</sup> and Fumihide Kojima<sup>2</sup>

<sup>1</sup>Graduate School of Engineering, Chiba University, 1-33, Yayoi-cho, Inage-ku, Chiba-shi, Chiba 263-8522, Japan

<sup>2</sup>Wireless System Laboratory, National Institute of Information and Communications Technology, 3-4 Hikarinooka, Yokosuka, Kanagawa 239-0847, Japan

Correspondence should be addressed to Kien Nguyen; [nguyen@chiba-u.jp](mailto:nguyen@chiba-u.jp)

Received 2 November 2018; Revised 28 December 2018; Accepted 4 February 2019; Published 14 February 2019

Guest Editor: In-Ho Lee

Copyright © 2019 Kien Nguyen et al. This is an open access article distributed under the Creative Commons Attribution License, which permits unrestricted use, distribution, and reproduction in any medium, provided the original work is properly cited.

The IEEE 802.11ad technology, which allows wireless devices to communicate in the unlicensed 60 GHz ISM band, promisingly provides multi-Gbps data rates for bandwidth-intensive applications. After years of research and development, we are now observing an increasing number of commodity IEEE 802.11ad radios that motivate researchers to exploit the IEEE 802.11ad capability for applications. This work first conducts an empirical study on the IEEE 802.11ad performance. In particular, we characterize the performance of IEEE 802.11ad links considering the variation of network parameters and interference. Secondly, we investigate the possibility of introducing IEEE 802.11ad to an evolving Wi-Fi network. The evaluation results show that our off-the-shelf IEEE 802.11ad hardware can achieve the Gbps level throughput of the transmission control protocol (TCP) and user datagram protocol (UDP). However, the evolution is not trivial since the hardware can not well maintain the 60 GHz link. The main reason is lacking the fast switchover function between an IEEE 802.11ad and a legacy Wi-Fi link. We then seek the potential of multipath TCP (MPTCP) for the expected switchover. The default MPTCP, which enables data transmissions on both the IEEE 802.11ad and Wi-Fi links, is harmful to the IEEE 802.11ad throughput. Meanwhile, the backup mode of MPTCP, in which the Wi-Fi link acts as a backup for IEEE 802.11ad one, can maintain the comparable performance. Therefore, we propose to adopt MPTCP with the backup mode in the evolving Wi-Fi networks. The efficiency of MPTCP-based switchover is confirmed by conducting real experiments.

## 1. Introduction

In recent years, the popularity of wireless devices and the explosion of wireless traffic require ever-increasing demands on better network performance [1]. Accordingly, there are ongoing efforts in realizing the next generation of mobile wireless networks (i.e., 5G), which is expected to provide significantly high peak performance indicators (i.e., 1000 times better than the current 4G) [2, 3]. The new network is also envisioned to support the next generation of bandwidth-intensive applications such as 4K, 8K video streaming, real-time gaming, and virtual and augmented reality. It is widely agreed that leveraging the underutilized radio spectrum of millimeter wave (mmWave) band (i.e., between 30 GHz and 300 GHz) is one of the most promising approaches to satisfy the bandwidth demand [4–6]. Within the mmWave band, there is a vast amount of bandwidth (up to 14 GHz) that is allocated as the unlicensed 60 GHz band (i.e., 57–71 GHz

spectrum). The 60 GHz band communication is supported by the IEEE 802.11ad standard [7, 8], which aims to bring multi-Gbps data rates to the next generation Wi-Fi network.

The IEEE 802.11ad physical layer uses 2.16 GHz-width channels that theoretically provide data rate up to 6.76 Gbps per single channel. Moreover, the IEEE 802.11ad radio with directional beams can improve the spatial use. The IEEE 802.11ad signal, however, incurs much higher attenuation than the one of legacy Wi-Fi. To compensate for the path loss, the IEEE 802.11ad device uses high gain antenna arrays, which on the other hand introduces a new challenge of link maintenance (e.g., when blockage exists). The maintenance is expected to be realized by switching to a legacy Wi-Fi link when the IEEE 802.11ad link is not available. Accordingly, numerous efforts in research and development have led to the advent of low-cost, low power, off-the-shelf IEEE 802.11ad devices [9]. The advent motivates many experimental studies that aim to exploit the 60 GHz opportunity in evolving

Wi-Fi networks. The previous works provide not only valuable insights of 60 GHz communication and IEEE 802.11ad features [10, 11] but also new use cases of IEEE 802.11ad [12, 13]. Although much has been understood, there is a lack of common understanding about the characterization of IEEE 802.11ad performance (esp. the feasible multi-Gbps throughput), as well as, evolvability of IEEE 802.11ad on Wi-Fi networks.

This work first addresses the issue of performance characterization; we empirically evaluate an off-the-shelf IEEE 802.11ad hardware in a typical office environment towards the achieved multi-Gbps throughput. The performance metrics of IEEE 802.11ad links have been extensively investigated under the variation of different network parameters and interference. In particular, we consider the existence and nonexistence of two typical types of IEEE 802.11 interferences (i.e., cochannel and adjacent channel). Moreover, we also scrutinize the network parameters such as signal strength, modulation and coding scheme (MCS), Maximum Transmission Unit (MTU), and traffic types (i.e., TCP and UDP). Thanks to the support of the IEEE 802.11ad driver and associated tools, we can find the multi-Gbps throughput (for both TCP, UDP) following the conditions of modulation and coding scheme (MCS) set, signal strength, and MTU. We also quantify the traditional interference effects on the throughput and lost packet metrics.

Secondly, targeting the evolvability issue, thoroughly investigate the capacity of link maintenance (i.e., the most significant challenge of 60 GHz communication). Our evaluation shows that the IEEE 802.11ad link itself can neither bypass the blockage nor handle the change of antenna direction. That is because there is a lack of the function of fast switchover between the IEEE 802.11ad and a legacy Wi-Fi link. We then seek the possibility of multipath TCP (MPTCP), which is capable of exploiting multiple wireless links concurrently, for the switchover. Our investigation points out that the default MPTCP (i.e., full mesh mode) that simultaneously uses the IEEE 802.11ad and Wi-Fi links for data transmission is not efficient. The overall throughput is largely varied and is always smaller than the TCP throughput of IEEE 802.11ad link. On the other hand, the backup mode of MPTCP, in which the IEEE 802.11ad and Wi-Fi links are in an active/standby state, guarantees the comparable throughput. Therefore, we propose to adopt MPTCP with the backup mode for the switchover. The efficiency of MPTCP-based switchover has been confirmed by conducting the real experiments.

The remainder of this paper can be outlined as follows. The following section presents related works. In Section 3, we introduce the imperial investigation on IEEE 802.11ad. Section 4 introduces an evolving Wi-Fi network with MPTCP. Finally, Section 5 concludes the paper.

## 2. Related Works

The experimental study is a popular method for understanding the performance characterization in IEEE 802.11 (Wi-Fi) networks. The method has shown its usability with different IEEE 802.11 versions such as IEEE 802.11n [14]

or IEEE 802.11ac [15]. Additionally, the same technique is also efficient in finding the conditions of significant IEEE 802.11 features (e.g., channel bonding in IEEE 802.11n [16]). With IEEE 802.11ad, there have been several early works, which use the experimental study [17–20]. Those works focus on modeling channel propagation characteristics using dedicated hardware for 60 GHz communications. In [10], the authors investigate the performance of 60 GHz links under conditions of introducing blockage and different antenna orientations. However, they use the non-802.11ad hardware and measure the performance of IP-over-wireless-HDMI. Hence, the results do not adequately reflect the characteristics of IEEE 802.11ad link. The work in [11] has profiled the indoor 60 GHz links by using a software-defined radio platform. Although the work offers many valuable insights (e.g., about the potential capabilities and limitations of flexible beams), it may not reflect the behavior of the real IEEE 802.11ad hardware (because of using a channel width of 245 MHz).

On the other hand, the off-the-shelf IEEE 802.11ad hardware is gaining popularity after years of efforts in R & D. That attracts the experimental studies on the IEEE 802.11ad performance. The most related one to ours is [21], in which the authors experiment IEEE 802.11ad radios in an indoor environment. Their results indicate the advantages of IEEE 802.11ad development in overcoming blockage and establishing suitable communication ranges. However, the feasibility of multi-Gbps IEEE 802.11ad link has not been fully confirmed. In fact, the measured throughput values are all below 1 Gbps. The reason may be the effects of autorate algorithm, which can not be disabled on the investigated hardware. Moreover, the authors use TCP traffic; hence the TCP congestion control may affect the performance. Additionally, some throughput values are reported indirectly via the PHY rates, which may not reflect the real ones correctly. We aim to complement the work [21] in the context of introducing the multi-Gbps IEEE 802.11ad link on evolving Wi-Fi networks. The difference in ours which initiated from the previous work [22] is that we consider the other influenced factors including interference, packet size, as well as, both the UDP, TCP traffic. Comparing to [22], this paper additionally includes more results such as the performance of interferer links under TCP and UDP.

The link maintenance capability, which is critical for the evolution of IEEE 802.11ad, has been investigated in several related works. In [23, 24], the authors present the implementation and evaluation of Fast Session Transfer (FST) within the IEEE 802.11ad standard. The evaluation results have shown the successful switch of continuous UDP flow between the 60 GHz and 5 GHz bands. However, those works are all simulation-based (i.e., [23] is with the OPNET environment while [24] is with ns-3), they may not correctly reflect the real IEEE 802.11ad hardware. On the other hand, MPTCP that simultaneously utilizes multiple wireless links for data transmission is a candidate for the expected switchover. In fact, the MPTCP-based switchover has been useful in many use cases such as Wi-Fi/LTE [25], virtual Wi-Fi/virtual Wi-Fi [26], Wi-Fi/Wi-Fi [27]. This work deeply investigates the capability of MPTCP in bypassing the problem of 60 GHz link maintenance. The feasibility of switching back-and-forth

a multi-Gbps transmission between an IEEE 802.11ad and a legacy Wi-Fi link has been initially presented in [28]. This work provides the detailed comparison with a new performance metric aiming to affirm the efficacy of MPTCP further.

### 3. Empirical Study on IEEE 802.11ad Performance

In this section, we first describe the overview of IEEE 802.11ad. After that, we present the experiment environment and the measurement results.

*3.1. IEEE 802.11ad Overview.* The IEEE 802.11ad standard supports peer-to-peer and infrastructure connections. In an IEEE 802.11ad link, each end's physical layer executes a beam-forming mechanism to form directional transmit/receive beams using a phased-array antenna. There are four types of PHY layers in the standard (i.e., control PHY, OFDM PHY, Single Carrier (SC) PHY, and Low Power SC PHY), each of which supports a set of MCSs. In the 2012 version, the channel list for IEEE 802.11ad operation in the 57-63 GHz band includes four channels as presented in Table 1. Recently, the Federal Communication Commission (FCC) of the US has announced that the 7 GHz band between 64 and 71 GHz is unlicensed aiming to be used by IEEE 802.11ad [29].

The 60 GHz link has a problem with blockage vulnerability. Moreover, the antenna direction may change in operation. Therefore, the link maintenance is vital to efficiently evolve IEEE 802.11ad on Wi-Fi networks. For that purpose, the IEEE 802.11ad standard defines the Fast Session Transfer (FST) protocol [7]. The protocol is supposedly equipped with multiband devices that have an IEEE 802.11ad and a legacy Wi-Fi radio. FST concurrently manages the radios, which are either in a transparent or nontransparent mode (i.e., having the same MAC address or different MAC addresses, respectively). FST defines a procedure of switching traffic between two links operating on different bands. The standard also specifies another mode of FST, in which the data transmission can concurrently happen over two bands (i.e., for link aggregation).

*3.2. Experiment Environment.* We conduct our investigation using a testbed deployed in a typical office environment. Each IEEE 802.11ad link is constructed by a pair of radio modules, which are produced by Panasonic Inc., Japan. Each module is connected to an Ubuntu 14.04 LTS machine that includes the supporting drivers and monitoring utilities. The radio module can run in the client or personal basic service set (PBSS) control point (PCP)/access point (AP) modes. The IEEE 802.11ad defines antenna beams as narrow as 2.86-degree. However, the investigated IEEE 802.11ad module uses 50-degree beam width [9]. Therefore, the throughput measurements in our study are probably the lower bounds of achievable performance of IEEE 802.11ad link. The module contains an implementation of single carrier PHY, that supports nine transmission rates (i.e., MCS indices 1 to 9). The basic information and theoretical PHY rate of MCSs are

presented in Table 2. In the 60 GHz band, the module can operate on channel 2 and channel 3 indicated in Table 1. The maximum value of supported MTU is 7912 bytes. We use the popular tool *iperf3* [30] for generating and collecting TCP and UDP traffic flows. The *iperf3* server, client runs on the machine associated with IEEE 802.11ad AP/PCP, client mode, respectively. The traffic flow typically lasts ten seconds. *iperf3* supports storing traffic information in the *json* format that is easy to parse for further processing and analysis. In order to conveniently experiment, we wrote custom scripts for easily controlling the settings of MCS, MTU, and collecting, extracting, and processing the measurement data such as Received Signal Strength Indicator (RSSI) provided by the IEEE 802.11 driver, etc.

*3.3. Investigation of IEEE 802.11ad Capability.* The investigation begins with checking the signal quality of IEEE 802.11ad link (i.e., ranges of RSSI values) in our environment. To identify the range of RSSI, we record the RSSI values every 0.1 seconds while varying the distance and direction between the pair of IEEE 802.11ad radios. We found that the IEEE 802.11ad link can communicate within the signal range of (-41 dBm, -69 dBm). In the following experiments, we define the strong signal scenario where the RSSI value is kept within (-41 dBm, -43 dBm) and the RSSI value in the weak one is within (-65 dBm, -69 dBm).

We then investigate the TCP and UDP throughput of IEEE 802.11ad link under the combination of all supported MCSs and the link quality scenarios. We also consider different sizes of MTU since they largely affect the throughput. For the high throughput purpose, the link should use the maximum supported MTU. Besides, there are cases of communicates to a far destination (e.g., more than one hop or accessing the Internet). In such cases, the communication is likely limited by a common MTU on the end-to-end path. Therefore, we select the value of 1500-byte MTU, which is typical on Wi-Fi networks and the Internet. We then evaluate the maximum supported MTU (7912 bytes) to observe the full capability provided by the hardware. The evaluation results expose distinct patterns in the behavior of throughput concerning different traffic types, MCSs, and MTUs. We provide a representative subset of our results that show the patterns as mentioned earlier in Figures 1, 2, 3, and 4. In each figure, the average throughput value at each MCS collected and calculated from ten measurements is shown. Moreover, the error bar shows the distance between maximum and minimum values.

The measured throughput of UDP and TCP traffic with 1500-byte MTU in the different signal scenarios are shown in Figures 1 and 2, respectively. Comparing the UDP throughput in the two figures, we can draw a common observation; that is, the UDP throughput is not directly affected by the signal strength. When the IEEE 802.11ad sends at the same speed (i.e., the same MCS value), the results are comparable in the two scenarios. We also have another important observation; that is, the UDP throughput reaches around 1 Gbps with MCS8 and MCS9. On the other hand, the weak signal negatively affects the TCP transmission, especially at the high transmission rates. That is indicated by the visible error bars

TABLE 1: IEEE 802.11ad channel list.

Channel	Center (GHz)	Minimum (GHz)	Maximum (GHz)	Bandwidth (GHz)
1	58.32	57.24	59.4	2.16
2	60.48	59.4	61.56	2.16
3	62.64	61.56	63.72	2.16
4	64.8	63.72	65.88	2.16

TABLE 2: Supported single carrier PHY modulation and coding scheme.

MCS Index	Modulation	Repetitions	Coding Rate	Rate (Mbps)
1	$\pi/2$ BPSK	2	1/2	385.0
2	$\pi/2$ BPSK	1	1/2	770.0
3	$\pi/2$ BPSK	1	5/8	962.5
4	$\pi/2$ BPSK	1	3/4	1155.0
5	$\pi/2$ BPSK	1	13/16	1251.0
6	$\pi/2$ QPSK	1	1/2	1540.0
7	$\pi/2$ QPSK	1	5/8	1925.0
8	$\pi/2$ QPSK	1	3/4	2310.0
9	$\pi/2$ QPSK	1	13/16	2502.0

on the right side of Figure 2. Moreover, the TCP throughput values are much smaller than not only the ones of UDP but also the level of 1 Gbps. The reasons include the limitation of MTU size and the sequencing transmissions of TCP. It is obvious that the IEEE 802.11ad link is not able to achieve the multi-Gbps performance with the 1500-byte MTU.

However, we have a different observation in the case of 7912-byte MTU as shown in Figures 3 and 4, which include many multi-Gbps values in both the strong and weak signal scenarios. In the former situation (Figure 3), the TCP and UDP throughput monotonically increase along with the higher transmission rates within each MCS set. The throughput values of UDP and TCP become higher than 1Gbps with the rate provided by MCS6 and MCS7, respectively. In the latter scenario (Figure 4), the increasing trend of UDP throughput is similar except for the case of the maximum supported rate (MCS9). In that case, the big MTU size gets more negative effects than the small MTU. However, it may be efficiently fixed by an algorithm of rate selection that never sends at the maximum speed with the weak signal. On the other hand, the negative effects of the weak signal on TCP are more severe than the ones on UDP. The TCP throughput starts to be significantly degraded from MCS8. That is caused by the behavior of TCP congestion control, which reduces the transmission rate due to lost packets.

From the above observations, we can conclude that the multi-Gbps throughput of IEEE 802.11ad link has been achievable with both the TCP and UDP traffic. However, those high throughput values depend on the signal strength, PHY rates, and MTU on the system.

*3.4. Impact of Adjacent Channel and Cochannel Interference.* This section investigates the effects of conventional interference factors (i.e., adjacent channel interference (ACI)

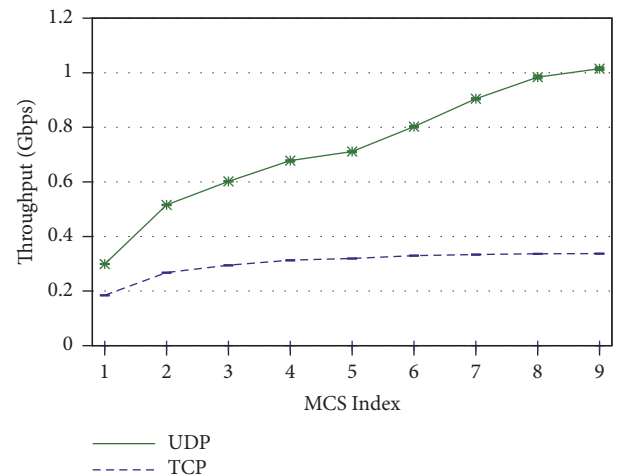


FIGURE 1: Throughput in strong signal and 1500-byte MTU scenario.

and cochannel interference (CCI) on the IEEE 802.11ad performance. ACI means wireless transmission on a specific channel suffers interference from channel leakage of its adjacent channels. Meanwhile, CCI indicates the effect of two communications that share a channel without being aware due to the known hidden terminal problem. The hidden terminal problem occurs when two transmitters are not in the transmission range of each other but the carrier sensing range. Due to the beamforming, the nearby position of an IEEE 802.11ad transmitter is within the carrier sensing range if it is outside of the directional transmission.

We set up an additional IEEE 802.11ad link with the strong signal as the interferer to evaluate the interference effects. An *iperf3*'s UDP flow over the link runs at the maximum

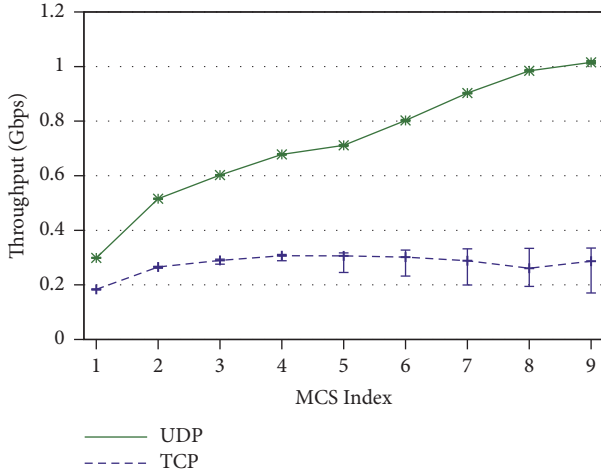


FIGURE 2: Throughput in weak signal and 1500-byte MTU scenario.

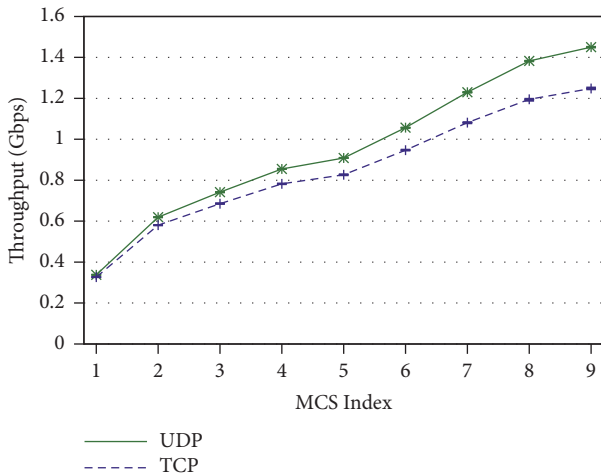


FIGURE 3: Throughput in strong signal and 7912-byte MTU scenario.

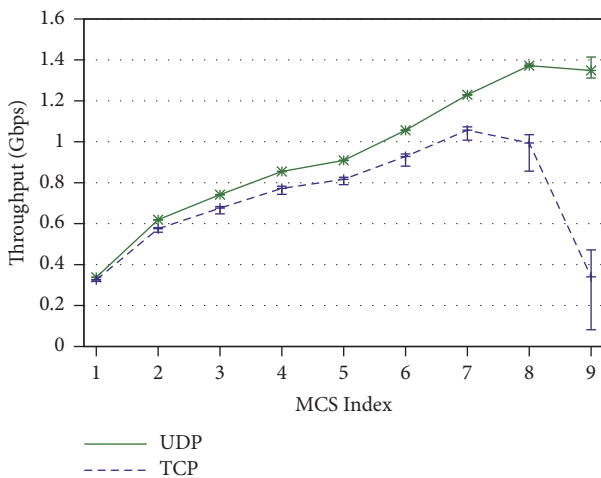


FIGURE 4: Throughput in weak signal and 7912-byte MTU scenario.

speed. The link is therefore supposed to fully occupy the wireless medium when there is no other transmission. The interference link is configured to operate on channels 3 and 2 for the investigation of ACI and CCI respectively. We use the 7912-byte MTU aiming to observe the variation of the multi-Gbps link. Similar to the previous experiments, we run our custom scripts, which enable the use of all supported MCSs. With each MCS, the associated experiment is also repeated ten times. We make the comparison with two metrics: the normalized throughput and the percentage of lost packets. The normalized throughput is defined as follows:

$$Th_{normalized} = \frac{Th_{measured}}{Th_{expected}} \quad (1)$$

in which  $Th_{measured}$  and  $Th_{expected}$  are the measurement throughput and the expected throughput, respectively. At each MCS, we choose  $Th_{expected}$  as the maximum throughput derived from the previous section. The average, minimum, and maximum values of normalized throughput and the percentage of lost packets are plotted in Figures 5 and 6.

In Figure 5, the normalized throughput values are all less than 1. That means ACI and CCI have negative impacts on the performance of IEEE 802.11ad link. Moreover, the average value (i.e., in the box plots) decreases along with the increase of data rates provided by MCSs; meanwhile, the values of measured throughput in fact increase. That indicates the higher transmission rates, the more serious impacts of interference. In the ACI scenario, the normalized throughput becomes less than 80% when the MCS index is higher than 5. On the other hand, similar degradation happens at MCS2 in the CCI scenario. CCI obviously has heavier influence than ACI. More specifically, the measured throughput in the ACI scenario is approximately 1 Gbps with MCS8 and MCS9. However, in the CCI scenario, the throughput values regardless of MCSs are all under the 1Gbps level. Another observation (in Figure 5) is that the interference effects cause big fluctuations in the IEEE 802.11ad throughput in different runs (i.e., in the error bars), especially in the CCI scenario. In order to avoid the fluctuations, the algorithms of careful network planning or interference mitigation may be necessary.

In Figure 6, the percentage of lost packets also shows a similar trend. When transmitting at low data rates (i.e., up to MCS5), the percentage values in the ACI and CCI scenarios are as small as the ones in the no-interference situation. However, when the data is transmitted at the higher rates, more lost packets appear in the two interference scenarios. The maximum percentage of the lost packet in the ACI scenario is about 1%. In the CCI scenario, the value of the maximum one is nearly 5%. The values are seemingly reasonable in comparing to the existing IEEE 802.11 networks in terms of percentage. The absolute amount of lost traffic, however, needs to be considered when deploying the multi-Gbps capability.

We further investigate ACI and CCI with the same setup of two IEEE 802.11ad links (i.e., strong signal, 7912-byte MTU); the traffic characteristic over the two links is however different. In this case, we try to start the traffic flows on the

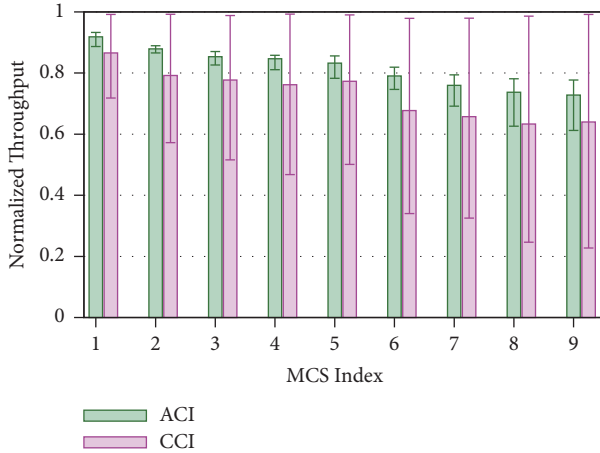


FIGURE 5: Comparison of UDP normalized throughput.

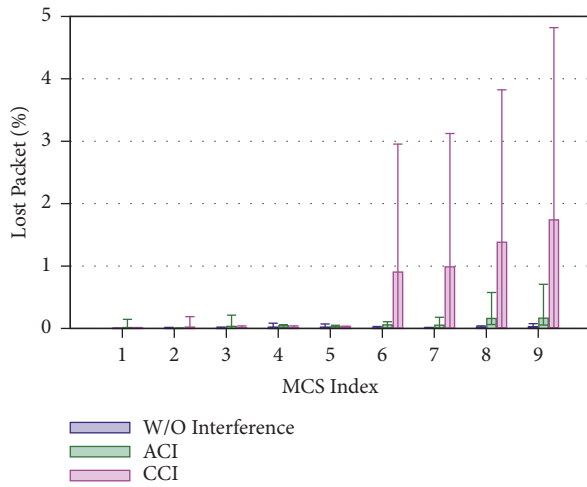


FIGURE 6: Comparison of lost packets.

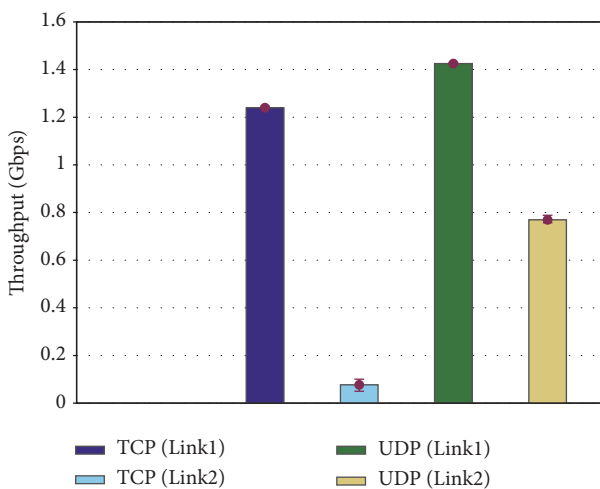


FIGURE 7: Throughput comparison in ACI scenario with concurrent start of two flows.

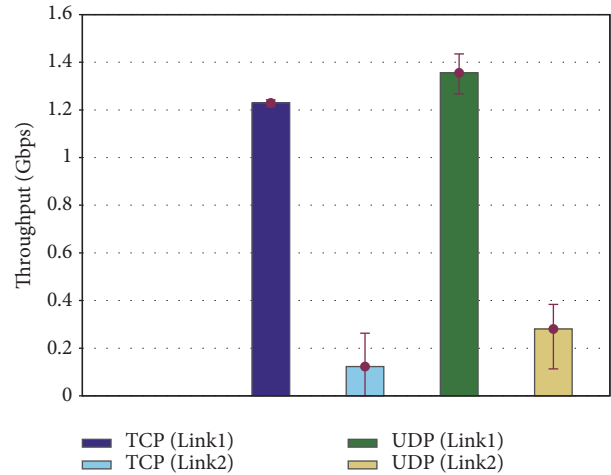


FIGURE 8: Throughput comparison in CCI scenario with concurrent start of two flows.

two links concurrently with both TCP and UDP traffic. In each experiment, when the *iperf3* process starts on Link1, it will enable remote access that initiates a similar *iperf3* process on Link2. In the same condition, an experiment is repeated ten times. We then plot the average, minimum, and maximum throughput values of UDP and TCP over the two IEEE 802.11ad links in the ACI and CCI scenarios in Figures 7 and 8. We can again observe that ACI and CCI cause significant degradation of the throughput of Link2. There is seemingly no fairness between the two links, probably due to a slower initialization of *iperf3* on Link2. In both ACI and CCI, the lost packets on the Link2 are severe that even makes the TCP traffic inefficient. The UDP throughput of Link2 is better than the TCP one. However, comparing to the noninterference scenario, the UDP throughput of Link2 equals half and one-fourth in case of ACI and CCI, respectively. Therefore, an efficient interference mitigation algorithm is necessary to guarantee the throughput performance.

#### 4. Evolving IEEE 802.11ad on Wi-Fi Networks with MPTCP

This section first investigates the capability of link maintenance in IEEE 802.11ad. We then present a method of realizing the link maintenance using MPTCP.

**4.1. Link Maintenance Capability and MPTCP Potential.** The link maintenance is critical in IEEE 802.11ad since the antenna may temporarily change directions or incur blockage. We hence check the ability of link maintenance on our hardware. We set up a traffic flow running over the IEEE 802.11ad link in 60 seconds. During the period, we observe the variation of traffic under two events: temporary introducing blockage and turning antenna directions. The throughput variation is plotted in Figure 9, which shows a common behavior in both cases. When the events occur the IEEE 802.11ad link is disabled and the throughput goes to zero; the link maintenance problem has not yet solved.

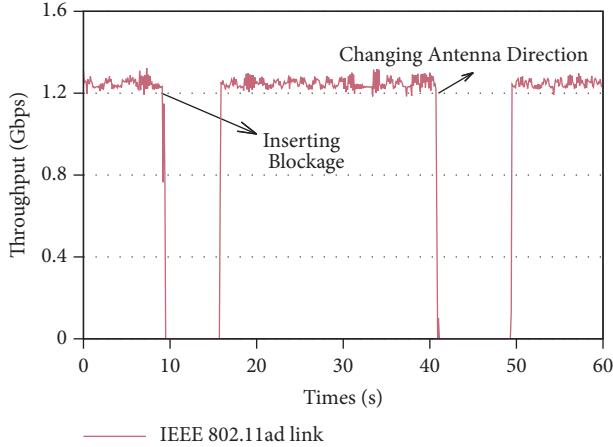


FIGURE 9: Throughput variation with introducing blockage and changing antenna direction.

It is necessary to bypass that problem to introduce the IEEE 802.11ad link in evolving Wi-Fi networks. The standard approach is getting the assistance from a legacy Wi-Fi link on the same device since the Wi-Fi link does not insist the mentioned events. However, the Fast Session Transfer (FST) function, which cooperates with IEEE 802.11ad and Wi-Fi links, is not supported by the hardware. Therefore, a replacement method is expected with the primary goal of achieving a fast switchover function between an IEEE 802.11ad link and legacy Wi-Fi link. MPTCP, which has recently standardized by IETF, shows a lot of potential in providing the switchover.

MPTCP introduces an additional layer between the application layer and the transport layer in the networking stack. MPTCP does not require any modification in the application or lower layers. MPTCP divides the application data into several subflows (i.e., similar to TCP connections), each of which contains data packets following a different path from a sender to a receiver. The received packets at the receiver are restructured based on their data sequence number. The default operation mode of MPTCP (i.e., full mesh) aims to maximize the usage of all available paths for throughput improvements. In the other modes, MPTCP can use a subset of available paths while putting the remaining paths in a standby condition. With the different modes of operation, as well as two levels of sequencing (i.e., subflow and data), MPTCP theoretically supports the automatic switching and shifting traffic between paths.

MPTCP is however designed for the LTE/Wi-Fi environment. Its potentiality and applicability in the evolving Wi-Fi network (i.e., with IEEE 802.11ad) in practice are not yet known. Besides, the legacy Wi-Fi and IEEE 802.11ad link have the significant difference in characteristics, which may cause unexpected harmful behaviors (e.g., bad packet reordering, inflated or false retransmission timeout, link overshoot, etc.) during the switchover. Addressing those, we investigate two possible operational modes of MPTCP (i.e., namely, full mesh and backup) in the evolving Wi-Fi network. In the former mode, the Wi-Fi and IEEE 802.11ad links

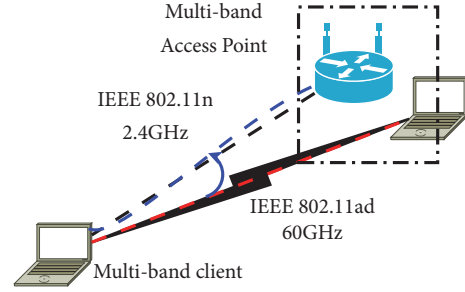


FIGURE 10: Evolving Wi-Fi network.

are concurrently used for transmitting data (i.e., supporting active/active switchover). In the latter, one link is a backup for the other (i.e., active/standby switchover).

**4.2. Evolving Wi-Fi Network with MPTCP.** We construct an evolving Wi-Fi network that includes IEEE 802.11ad, legacy Wi-Fi link, and MPTCP to investigate the capability of MPTCP. The network is shown in Figure 10 in which the multiband (MB) client has an IEEE 802.11n radio (i.e., on the 2.4 GHz band) and an IEEE 802.11ad radio. The MB can communicate with the multiband access point (AP) via both the 2.4 GHz and 60 GHz links. The AP and the MB client are equipped with the MPTCP kernel version 0.90 [31]. The appropriate routing policy has been configured to route packets correctly over two wireless links. In each experiment, we use *iperf3* to generate a TCP flow from the MB client to the AP in 60 seconds.

We initially explored the MPTCP's two modes in normal conditions (without link error) in the network. The performance metric under investigation is inherited from the aggregation benefit function, which has been proposed in the literature [32]. We slightly modify the function to include this case, where MPTCP uses two links IEEE 802.11ad and 802.11n. If we denote  $Ben(mode)$  as the aggregation benefit function in an operation *mode* of MPTCP, the function is as follows.

$$Ben(mode) = \begin{cases} \frac{T_{mode} - L_{max}}{\sum_{i=1}^2 L_i - L_{max}}, & \text{if } T_{mode} \geq L_{max} \\ \frac{T_{mode} - L_{max}}{L_{max}}, & \text{if } T_{mode} < L_{max} \end{cases} \quad (2)$$

where  $L_i$  is the link capacity of the link  $i$ ,  $L_{max}$  is the highest capacity among all links, and  $T_{mode}$  is the measured throughput value of MPTCP with *mode*. In the investigated network,  $L_{max}$  is always the throughput over the IEEE 802.11ad link. We denote  $L_{11ad}$  and  $L_{11n}$  as the link capacity of IEEE 802.11ad and IEEE 802.11n link, respectively.  $Ben(mode)$  in (2) can be transferred to

$$Ben(mode) = \begin{cases} \frac{T_{mode} - L_{11ad}}{L_{11n}}, & \text{if } T_{mode} \geq L_{11ad} \\ \frac{T_{mode} - L_{11ad}}{L_{11ad}}, & \text{if } T_{mode} < L_{11ad} \end{cases} \quad (3)$$



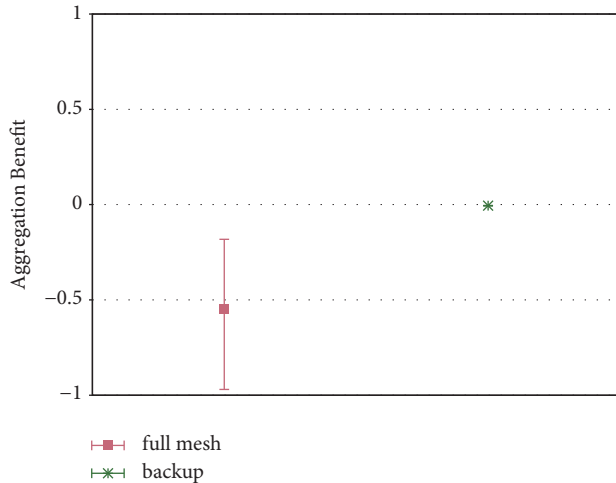


FIGURE 11: Comparison of aggregation benefit.

It is obvious that the values of  $Ben(m)$  are in the range  $[-1, 1]$ . If  $Ben(m) \geq 0$ , MPTCP has a positive benefit and vice versa.

To identify  $L_{11ad}$  and  $L_{11n}$  in (3), we run *iperf3* with TCP over each wireless link; each experiment is repeated ten times. In this case with the maximum supported speed at MCS9 of IEEE 802.11ad, we selected the maximum throughput among all runs, which is 1.316 Gbps. Similarly, we got the IEEE 802.11n's maximum throughput at 46.16 Mbps. In the MPTCP experiment, either the full mesh or backup mode, a batch of ten experiments is executed and we collect all the measured MPTCP throughput. We calculate and show the average, minimum, and maximum values of  $Ben(fullmesh)$  and  $Ben(backup)$  in Figure 11. In the figure, the values of  $Ben(fullmesh)$  are not only always negative but also largely varied. On the other hand, the values of  $Ben(backup)$  are stable around zero, which means the performance is comparable to the TCP throughput over the IEEE 802.11ad. We also calculate the average, minimum, and maximum throughput of TCP and two different modes of MPTCP in the investigated cases. The comparative values are shown in Figure 12. We can see that the throughput values of TCP on IEEE 802.11ad and the MPTCP backup are almost similar. That is because the difference between the two is only the handshaking period. However, the full mesh mode has a bad performance compared to the others and the Gbps level. While the backup mode's throughput values are always at the multi-Gbps level, the full mesh's ones are unstable. The worst value of the full mesh throughput approximates the throughput of IEEE 802.11n. In this case, the reason is mainly due to the different characteristics of two wireless links. The MTU of IEEE 802.11ad is 7912 bytes, while the IEEE 802.11n's MTU is 1500 bytes. The MTU sizes confuse the packet scheduler of MPTCP full mesh at the high transmission rate, consequently reducing the overall throughput.

We then explore the effects of MTU size on the throughput performance of MPTCP. We aim to change the MTU value on each wireless link and to repeat the previous *iperf3* experiments. We have modified our previous scripts to include the MTU configuration using the *ip* utility (e.g.,

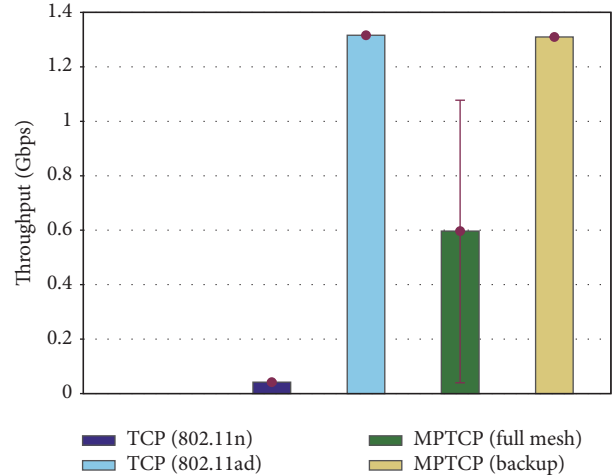


FIGURE 12: Throughput comparison between MPTCP in two modes and TCP.

change the MTU of *wigig0* to the size 3000 bytes: *ip link set dev wigig0 mtu 3000*). Since the maximum supported MTU for the transmission between the Wi-Fi card and AP is 1500 bytes, we can not have a bigger value of MTU on the IEEE 802.11n link. We hence decided to vary the MTU on the IEEE 802.11ad link for the performance evaluation. More specifically, we consider the MTU size in the set of  $\{1500, 3000, 4500, 6000\}$  (bytes). We collect and plot the throughput values in Figure 13. In the figure, we show the average throughput of MPTCP backup since the collected values are quite stable. Meanwhile, we show the maximum values of the MPTCP full mesh. In both modes, the throughput increases along with the MTU size. At the 1500- and 3000-byte MTU, we have a different observation as the previous comparison. The full mesh performance is better than the one of backup with the small MTU sizes. That means the aggregation benefit of MPTCP has been positive due to the efficient operation of the scheduler. However, the aggregate throughput is far less than the 1 Gbps level. Additionally, the wireless resource of both link has been used in the full mesh mode. Therefore, the usage of such MTU sizes for applications should take into consideration that trade-off. On the other hand, when the MTU values are either 4500 or 6000 bytes, it is seen that the MPTCP backup mode's performance is better. Therefore, the backup mode is likely adopted for the sakes of high throughput and resource efficiency.

We further observe the throughput of MPTCP full mesh with all the supported MCSs in comparison to the one of TCP over IEEE 802.11ad link, which is similar to the MPTCP backup throughput. At each PHY rate, we collect and calculate the average, minimum, and maximum values of measured throughput of ten runs. We show the values in Figure 14. The figure indicates that except MCS1, with all other PHY rates in our experiment, the MPTCP full mesh's average throughput is smaller than the TCP throughput. In particular, the higher the physical rate is, the worse the measured throughput becomes. With MCS1,

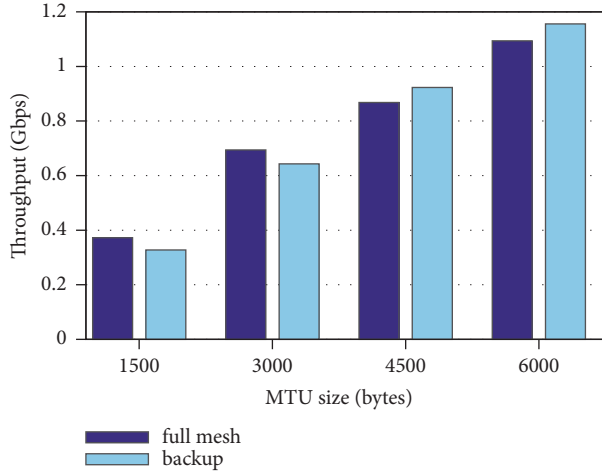


FIGURE 13: Throughput comparison between the full mesh and backup modes with different MTU sizes.

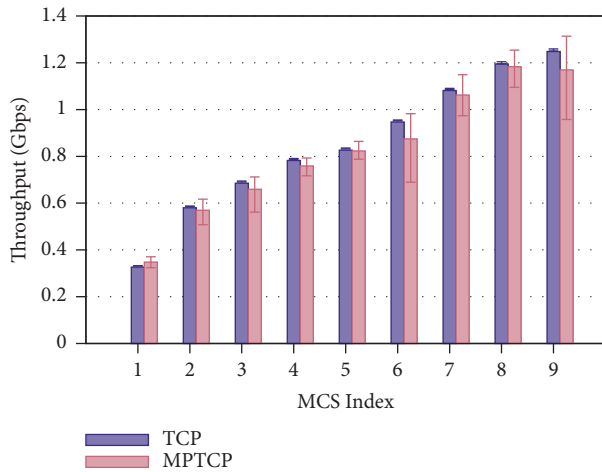


FIGURE 14: Comparison of TCP/MPTCP backup and MPTCP full mesh.

the MPTCP throughput is slightly better than the TCP throughput. On the other hand, MPTCP with the full mesh mode uses more networking resources than TCP since the two wireless links are both active for data transmissions. Therefore, we conclude that MPTCP full mesh (with the 7912-byte MTU of IEEE 802.11ad link) is not suitable for the expected switchover in the evolving Wi-Fi network.

In the following, we investigate the performance of MPTCP with the backup mode in the context of achieving the switchover in the evolving Wi-Fi network. The backup mode lets the IEEE 802.11n link be in a standby state for MPTCP packets in a normal condition. The IEEE 802.11n link will be active for MPTCP transmission when the IEEE 802.11ad link is not available. In this investigation, we keep the traffic condition similar to the previous one in the MPTCP evaluation. However, we additionally introduce the events of inactive, reactive links as follows. A period after starting the experiment, we change the direction of the

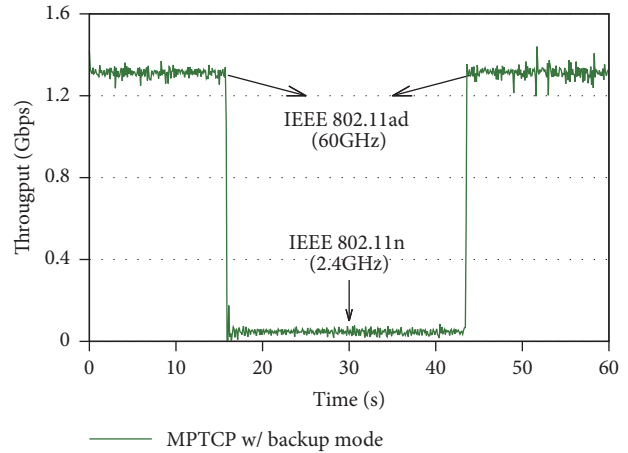


FIGURE 15: Achieving switchover with MPTCP backup.

IEEE 802.11ad radio on the MB until the IEEE 802.11ad link becomes inactive (i.e., note that this event is considerably similar to inserting blockage). After another period, we turn the radio back to the original direction for reactivating the IEEE 802.11ad link. During the experiment, we track the instantaneous throughput values at every 0.1 seconds; we then show them in Figure 15. The figure shows that the *iperf3* traffic is automatically switched from the IEEE 802.11ad link (i.e., in the 60 GHz band) to the IEEE 802.11n link (i.e., in the 2.4 GHz band) when the IEEE 802.11ad link is unavailable. Furthermore, after the recovery of IEEE 802.11ad link, the traffic is shifted back to the IEEE 802.11ad link and the application enjoys the higher bandwidth. In other words, MPTCP with the backup mode has efficiently achieved the expected switchover of IEEE 802.11ad.

## 5. Conclusion

With the advent of new off-the-shelf IEEE 802.11ad wireless devices, which can provide Gbps “wire like” experience to Wi-Fi networks, it is necessary to investigate the capacity of IEEE 802.11ad hardware to introduce the multi-Gbps capability to evolving Wi-Fi networks efficiently. This work first provides an in-depth experimental study on IEEE 802.11ad links in a typical office environment under the variation of network and interference conditions. We confirm the multi-Gbps throughput of both the UDP and TCP traffic with the constraints of signal strength, MCSs, and MTUs. Secondly, we verified that the link maintenance problem (e.g., due to blockage or changing antenna directions) still exists. To solve the problem, we propose to use MPTCP as a mean that provides a fast switchover between an IEEE 802.11ad to a legacy Wi-Fi link. Our evaluation results show that the IEEE 802.11ad radios can evolve on an existing Wi-Fi network. In particular, MPTCP with the backup mode could efficiently switch the multi-Gbps traffic on IEEE 802.11ad to a legacy Wi-Fi (i.e., IEEE 802.11n) link and vice versa.

## Data Availability

The experimental data used to support the findings of this study are available from the corresponding author upon request.

## Disclosure

The preliminary results of this research have been presented in the 2017 IEEE International Conference on Communications Workshops (ICC Workshops) [22] and the 2017 IEEE 86th Vehicular Technology Conference (VTC2017-Fall) [28]. Mirza Golam Kibria is now with SIGCOM Research Group, SnT, University of Luxembourg.

## Conflicts of Interest

The authors declare that they have no conflicts of interest.

## Acknowledgments

This research was conducted under a contract of R&D for Expansion of Radio Wave Resources, organized by the Ministry of Internal Affairs and Communications, Japan. Additionally, the first author is supported by the Leading Initiative for Excellent Young Researchers (LEADER) program from the Ministry of Education, Culture, Sports, Science and Technology, Japan.

## References

- [1] CISCO, "Cisco visual networking index: global mobile data traffic forecast update, 2016-2021," <http://www.cisco.com/c/en/us/solutions/collateral/service-provider/visual-networking-index-vni/mobile-white-paper-cl1-520862.pdf>.
- [2] J. G. Andrews, S. Buzzi, W. Choi et al., "What will 5G be?" *IEEE Journal on Selected Areas in Communications*, vol. 32, no. 6, pp. 1065–1082, 2014.
- [3] M. Shafi, A. F. Molisch, P. J. Smith et al., "5G: A tutorial overview of standards, trials, challenges, deployment, and practice," *IEEE Journal on Selected Areas in Communications*, vol. 35, no. 6, pp. 1201–1221, 2017.
- [4] T. Rappaport, S. Sun, R. Mayzus et al., "Millimeter wave mobile communications for 5G cellular: it will work!" *IEEE Access*, vol. 1, pp. 335–349, 2013.
- [5] K. Sakaguchi, T. Haustein, S. Barbarossa et al., "Where, when, and how mmwave is used in 5G and beyond," *IEICE Transactions on Electronics*, vol. E100.C, no. 10, pp. 790–808, 2017.
- [6] A. M. Hamed and R. K. Rao, "Spectral and energy efficiencies in mmwave cellular networks for optimal utilization," *Wireless Communications and Mobile Computing*, vol. 2018, Article ID 3097094, 11 pages, 2018.
- [7] "IEEE Std 802.11ad-2012 (Amendment to IEEE Std 802.11-2012, as Amended by IEEE Std 802.11ae-2012 and IEEE Std 802.11aa-2012. Part 11: Wireless LAN Medium Access Control (MAC) and Physical Layer (PHY) Specifications Amendment 3: Enhancements for Very High Throughput in the 60 GHz Band," pp. 1–628, 2012.
- [8] T. Nitsche, C. Cordeiro, A. B. Flores, E. W. Knightly, E. Perahia, and J. C. Widmer, "IEEE 802.11ad: Directional 60 GHz communication for multi-gigabit-per-second Wi-Fi," *IEEE Communications Magazine*, vol. 52, no. 12, pp. 132–141, 2014.
- [9] N. Saito, T. Tsukizawa, N. Shirakata et al., "A fully integrated 60-GHz CMOS transceiver chipset based on WiGig/IEEE 802.11ad with built-in self calibration for mobile usage," *IEEE Journal of Solid-State Circuits*, vol. 48, no. 12, pp. 3146–3159, 2013.
- [10] X. Tie, K. Ramachandran, and R. Mahindra, "On 60 GHz wireless link performance in indoor environments," *Lecture Notes in Computer Science (including subseries Lecture Notes in Artificial Intelligence and Lecture Notes in Bioinformatics): Preface*, vol. 7192, pp. 147–157, 2012.
- [11] S. Sur, V. Venkateswaran, X. Zhang, and P. Ramanathan, "60 GHz indoor networking through flexible beams: A link-level profiling," in *Proceedings of the ACM SIGMETRICS International Conference on Measurement and Modeling of Computer Systems, SIGMETRICS 2015*, pp. 71–84, ACM, June 2015.
- [12] D. Halperin, S. Kandula, J. Padhye, P. Bahl, and D. Wetherall, "Augmenting data center networks with multi-gigabit wireless links," in *Proceedings of the ACM SIGCOMM 2011 Conference, SIGCOMM'11*, pp. 38–49, Toronto, Canada, August 2011.
- [13] Y. Zhu, Z. Zhang, Z. Marzi et al., "Demystifying 60GHz outdoor picocells," in *Proceedings of the 20th ACM Annual International Conference on Mobile Computing and Networking, MobiCom 2014*, pp. 5–16, September 2014.
- [14] L. Kriara, M. K. Marina, and A. Farshad, "Characterization of 802.11n wireless LAN performance via testbed measurements and statistical analysis," in *Proceedings of the 2013 10th Annual IEEE Communications Society Conference on Sensing and Communication in Wireless Networks, SECON 2013*, pp. 158–166, June 2013.
- [15] E. Costa Molero, L. Kriara, and T. Gross, "Poster: regression-based characterization of 802.11Ac indoor performance," in *Proceedings of the ACM MobiCom*, pp. 254–256, Paris, France, September 2015.
- [16] L. Deek, E. Garcia-Villegas, E. Belding, S.-J. Lee, and K. Almeroth, "Intelligent channel bonding in 802.11n WLANs," *IEEE Transactions on Mobile Computing*, vol. 13, no. 6, pp. 1242–1255, 2014.
- [17] P. F. M. Smulders and L. M. Correia, "Characterisation of propagation in 60 GHz radio channels," *Electronics and Communication Engineering Journal*, vol. 9, no. 2, pp. 73–80, 1997.
- [18] C. R. Anderson and T. S. Rappaport, "In-building wideband partition loss measurements at 2.5 and 60 GHz," *IEEE Transactions on Wireless Communications*, vol. 3, no. 3, pp. 922–928, 2004.
- [19] P. F. M. Smulders, "Statistical characterization of 60-GHz indoor radio channels," *IEEE Transactions on Antennas and Propagation*, vol. 57, no. 10, pp. 2820–2829, 2009.
- [20] A. Maltsev, R. Maslennikov, A. Sevastyanov, A. Khoryaev, and A. Lomayev, "Experimental investigations of 60 GHz WLAN systems in office environment," *IEEE Journal on Selected Areas in Communications*, vol. 27, no. 8, pp. 1488–1499, 2009.
- [21] S. K. Saha, V. V. Vira, A. Garg, and D. Koutsonikolas, "Multi-Gigabit indoor WLANs: Looking beyond 2.4/5 GHz," in *Proceedings of the 2016 IEEE International Conference on Communications, ICC 2016*, IEEE, May 2016.
- [22] K. Nguyen, M. G. Kibria, K. Ishizu, and F. Kojima, "Empirical investigation of IEEE 802.11ad network," in *Proceedings of the 2017 IEEE International Conference on Communications*

- Workshops (ICC Workshops)*, pp. 192–197, Paris, France, May 2017.
- [23] C. Cordeiro, D. Akhmetov, and M. Park, “IEEE 802.11ad: introduction and performance evaluation of the first multi-gbps wifi technology,” in *Proceedings of the 2010 ACM International Workshop*, pp. 3–8, ACM, Chicago, Illinois, USA, September 2010.
- [24] H. Assasa and J. Widmer, “Implementation and evaluation of a WLAN IEEE 802.11ad model in ns-3,” in *Proceedings of the 8th Workshop on Network Simulator (ns-3), WNS3 2016*, pp. 57–64, USA, June 2016.
- [25] C. Paasch, G. Detal, F. Duchene, C. Raiciu, and O. Bonaventure, “Exploring mobile/WiFi handover with multipath TCP,” in *Proceedings of the ACM SIGCOMM Workshop on Cellular Networks: Operations, Challenges, and Future Design (CellNet '12)*, pp. 31–36, Helsinki, Finland, August 2012.
- [26] K. Nguyen, Y. Ji, and S. Yamada, “A cross-layer approach for improving WiFi performance,” in *Proceedings of the 2014 International Wireless Communications and Mobile Computing Conference (IWCMC)*, pp. 458–463, Nicosia, Cyprus, August 2014.
- [27] Y.-S. Lim, Y.-C. Chen, E. M. Nahum, D. Towsley, and K.-W. Lee, “Cross-layer path management in multi-path transport protocol for mobile devices,” in *Proceedings of the 33rd IEEE Conference on Computer Communications, IEEE INFOCOM 2014*, pp. 1815–1823, May 2014.
- [28] K. Nguyen, M. G. Kibria, K. Ishizu, and F. Kojima, “Feasibility study of providing backward compatibility with MPTCP to WiGig/IEEE 802.11ad,” in *Proceedings of the 86th IEEE Vehicular Technology Conference, VTC Fall 2017*, pp. 1–5, September 2017.
- [29] Federal Communications Commission, “Notice of proposed rulemaking,” [https://apps.fcc.gov/edocs\\_public/attachmatch/FCC-15-138A1.pdf](https://apps.fcc.gov/edocs_public/attachmatch/FCC-15-138A1.pdf).
- [30] ESnet / Lawrence Berkeley National Laboratory, “iperf3: A TCP, UDP, and SCTP network bandwidth measurement tool,” <https://github.com/esnet/iperf>.
- [31] C. Paasch, S. Barre et al., “Multipath TCP in the linux kernel,” <http://www.multipath-tcp.org>.
- [32] D. Kasper, *Multipath Aggregation of Heterogeneous Networks [Ph.D. thesis]*, University of Oslo, 2011.

## Research Article

# Outage Analysis of User Pairing Algorithm for Full-Duplex Cellular Networks

Hyun-Ho Choi <sup>1</sup> and Wonjong Noh <sup>2</sup>

<sup>1</sup>Department of Electrical, Electronic and Control Engineering, Hankyong National University, Anseong 17579, Republic of Korea

<sup>2</sup>Department of Electronics and Communication Engineering, GTEC, Siheung 15073, Republic of Korea

Correspondence should be addressed to Wonjong Noh; [wonjong.noh@gmail.com](mailto:wonjong.noh@gmail.com)

Received 10 August 2018; Revised 3 October 2018; Accepted 16 December 2018; Published 2 January 2019

Guest Editor: Jung-Bin Kim

Copyright © 2019 Hyun-Ho Choi and Wonjong Noh. This is an open access article distributed under the Creative Commons Attribution License, which permits unrestricted use, distribution, and reproduction in any medium, provided the original work is properly cited.

In a full-duplex (FD) cellular network, a base station transmits data to the downlink (DL) user and receives data from uplink (UL) users at the same time; thereby the interference from UL users to DL users occurs. One of the possible solutions to reduce this interuser interference in the FD cellular network is *user pairing*, which pairs a DL user with a UL user so that they use the same radio resource at the same time. In this paper, we consider a user pairing problem to minimize outage probability and formulate it as a nonconvex optimization problem. As a solution, we design a low-complexity user pairing algorithm, which first controls the UL transmit power to minimize the interuser interference and then allows the DL user having a worse signal quality to choose first its UL user giving less interference to minimize the outage probability. Then, we perform theoretical outage analysis of the FD cellular network on the basis of stochastic geometry and analyze the performance of the user pairing algorithm. Results show that the proposed user pairing significantly decreases the interuser interference and thus improves the DL outage performance while satisfying the requirement of UL signal-to-interference-plus-noise ratio, compared to the conventional HD mode and a random pairing. We also reveal that there is a fundamental tradeoff between the DL outage and UL outage according to the user pairing strategy (e.g., throughput maximization or outage minimization) in the FD cellular network.

## 1. Introduction

Full-duplex (FD) technologies enable a wireless node to transmit and receive data on the same radio resource at the same time so that the system capacity can be increased up to two times in theory. However, this FD operation causes co-channel interferences between entities using the same resource, whereas the conventional half-duplex (HD) mode does not create such interferences. In FD cellular network, two types of co-channel interference occur: *self-interference* occurs from the transmit (Tx) antenna to the receive (Rx) antenna at the base station (BS) and *interuser interference* occurs from the uplink (UL) user to the downlink (DL) user [1, 2].

In an FD transceiver, the self-interference signal from its transmitter is typically 100 dB stronger than the intended receiving signal. This strong self-interference in the FD transceiver obviously makes the radio chain at the receiver

saturated and the received data cannot be decoded properly [3]. However, this self-interference problem has recently been solved by advanced technologies of analog and digital signal processing. It is now feasible to achieve up to 110 dB self-interference cancellation (SIC) capability [4]. Thus, the self-interference is mostly reduced to the same level as the signal of interest before going through the decoding chain at the receiver; thus, data decoding is possible. In practice, there are many real-time prototypes demonstrated for FD communications [5–8].

Although a single-link FD transmission has become technically feasible, it is still expensive to equip SIC functionality with above 100 dB to all user equipment (UE) for the deployment of FD cellular network. Thus, most of the UEs may still operate in HD mode and it is more practical to suppose that only BSs operate in FD mode. As a result, coexistence of both UL and DL transmission on the same channel at the same time in the FD cellular network causes

so-called interuser interference from UL users to DL users. Therefore, smart interference management techniques are necessary to manage this interuser interference and several algorithms including resource management, power control, user pairing/scheduling, and their optimization have been investigated to enhance performances in terms of system throughput, outage probability, and coverage [9–20].

Related to the resource allocation algorithm, a joint resource allocation was considered to reduce the interuser interference in FD cellular networks [9]. In [10], a simple two-user FD network was investigated and a noncooperative game was presented for resource allocation. In [11], energy efficient resource allocation was invented to minimize total transmit power in FD cellular networks. Regarding the power control, the transmit powers of the UL UE, BS, and relay were coordinated to mitigate the interference in an FD relay-enhanced cellular network [12]. In [13], an effective power control scheme was proposed to suppress interference between D2D and cellular communications for FD relay-assisted device-to-device communication. In [14], a distributed power control algorithm was suggested based on Fast-Lipschitz optimization to maximize the sum spectral efficiency in the three-node FD transmission mode.

Furthermore, various user pairing/scheduling algorithms for an FD network were investigated [15]. In [16], a cooperative FD relays- (FDRs-) based scheduling technique was proposed to achieve additional throughput by using cooperative FDRs. In [17], a suboptimal heuristic joint user scheduling and channel allocation algorithm with low complexity were devised in FD cellular networks. In [18], two kinds of user pairing schemes were presented to maximize throughput and minimize outage in a single-cell FD network. Thereafter, the throughput performance of the first throughput-maximizing user pairing algorithm was analyzed [19]. Moreover, a joint optimization problem was investigated by considering mode selection, user pairing, subcarrier allocation, and power control in order to maximize the aggregate network throughput in FD heterogeneous networks [20].

As an important issue, the user pairing problem has also been studied in other network scenarios [21–26]. A cross-layering method was proposed to solve the pairing problem for collaborative spatial multiplexing in IEEE 802.16 networks [21]. A user pairing scheme was proposed based on the generalized lattice code to improve the average sum rate in an amplify-and-forward multiway relay network [22]. User pairing stability was analyzed in device-to-device-relay networks and a metric to quantize it was proposed [23]. A distributed matching algorithm was proposed to optimize the user pairing in a downlink nonorthogonal multiple access (NOMA) network [24]. A low-complexity user pairing algorithm was proposed using a heuristic approach for NOMA-based cellular network [25]. Impact of user pairing was analyzed considering imperfect channel state information in NOMA-based energy harvesting relaying networks [26].

Many studies on user pairing approaches in FD networks have been conducted, where the throughput performance is mostly analyzed and optimized but the outage performance is relatively less studied. Unlike [18], this study considers a new multicell structure and performs a mathematical analysis on

the basis of stochastic geometry for the outage-minimizing user pairing algorithm presented previously. Compared to the throughput analysis in [19], we here perform a new outage analysis on existing user pairing algorithms considering different system configurations, which have not been dealt with in [18, 19].

In this paper, we propose a user pairing algorithm to reduce the interuser interference from UL to DL users in FD cellular networks. We describe a user pairing problem for minimizing outage probability. To solve this problem, a very highly complexity is required and we devise a suboptimal algorithm with low complexity from a practical point of view. The basic approach of the proposed user pairing is that it first reduces the transmit power of UL users to satisfy the signal-to-interference-plus-noise ratio (SINR) threshold for minimizing the inter-user interference, and then makes the DL user having a worse signal quality select first its UL user who gives less interference for outage minimization. We perform an outage analysis of the FD network by using stochastic geometry to identify the influence of the user pairing algorithms. Results show that the FD system using the proposed pairing algorithm greatly improves outage probability compared to the conventional user pairing algorithms.

The remainder of this paper is organized as follows. In Section 2, the system of the considered FD cellular network is described. In Section 3, the user pairing algorithm for outage minimization is explained. In Section 4, a stochastic geometry-based analysis in terms of DL and UL outage probabilities is provided. In Section 5, simulation and analysis results are provided. Finally, we present our concluding remarks in Section 6.

## 2. System Model

We consider a multicell network where each cell is adjacent to  $N$  neighboring cells, as illustrated in Figure 1. The BS uses FD mode whereas DL and UL users use HD mode owing to the limited implementation cost of UE. We assume that there are total  $2M$  users in each cell and both the numbers of UL users and of DL users are  $M$  evenly. In addition, one transmission frame has  $M$  resource blocks (RBs) and each user is allocated only one RB within a frame to transmit or receive data. This RB allocation is conducted in a way of round-robin in order to provide some degree of fairness for all users [27].

As shown in Figure 1, each channel coefficient is defined as follows.

- (i)  $h_{i0}$ : channel from serving BS<sub>0</sub> to DL user  $i$
- (ii)  $h_{0j}$ : channel from the UL user  $j$  to serving BS<sub>0</sub>
- (iii)  $g_{00}$ : channel from Tx to Rx in the serving BS<sub>0</sub>
- (iv)  $g_{0n}$ : channel from neighboring BS  $n$  to serving BS<sub>0</sub>
- (v)  $g_{in}$ : channel from neighboring BS  $n$  to DL user  $i$
- (vi)  $f_{ij}$ : channel from UL user  $j$  to DL user  $i$
- (vii)  $f_{in}$ : channel from UL user in the  $n$ -th neighboring cell to DL user  $i$
- (viii)  $f_{0n}$ : channel from UL user in the  $n$ -th neighboring cell to serving BS<sub>0</sub>

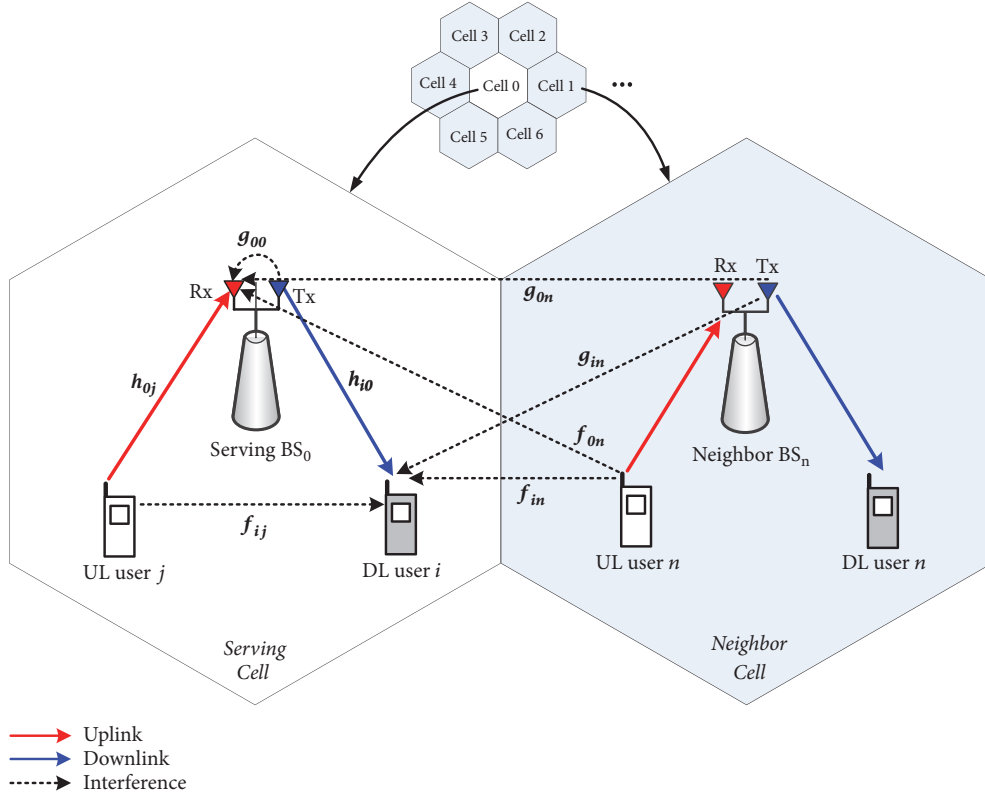


FIGURE 1: System model for full-duplex cellular networks considered.

Here, we assume that all the channel coefficients follow  $\mathcal{E}\mathcal{N}(0, \sigma^2/d_{ij}^\alpha)$  where  $d_{ij}$  is the physical distance of the corresponding  $ij$  link and  $\alpha$  is the path loss exponent. Further,  $n_i$  is the additive white Gaussian noise with zero mean and  $N_0$  variance.

Since both the DL and UL users send data on the same frequency at the same time, the DL user suffers from three different interferences from (1) the UL user who uses the same RB within the serving cell, (2) the Tx of neighbor BSs, and (3) the UL users who use the same RB in neighbor cells. Thus, the received signal of DL user  $i$  is represented as

$$\begin{aligned}
 y_i = & \sqrt{P_0}h_{i0}x_i + \underbrace{\sqrt{P_j}f_{ij}x_j}_{\text{inter-user intf.}} + \underbrace{\sum_{n=1}^N \sqrt{P_0}g_{in}\hat{x}_n}_{\text{intf. from neighbor BSs}} \\
 & + \underbrace{\sum_{n=1}^N \sqrt{P_n}f_{in}\check{x}_n}_{\text{intf. from neighbor UL users}} + n_i
 \end{aligned} \quad (1)$$

where  $P_0$  and  $P_j$  are the transmission power of the serving BS and UL user  $j$ , respectively. Moreover,  $x_i$ ,  $x_j$ , and  $x_n$  are the signals transmitted from the serving BS<sub>0</sub>, the UL user  $j$  with the same RB, and the  $n$ -th neighboring cell, respectively.

Furthermore, the Rx of the BS suffers from three different interferences from (1) the Tx of the serving BS, (2) the Tx of neighbor BSs, and (3) the UL users who use the same RB in

neighbor cells. Accordingly, the received signal at the serving BS<sub>0</sub> from the UL user  $j$  is represented as

$$\begin{aligned}
 y_j = & \sqrt{P_j}h_{0j}x_j + \underbrace{\sqrt{P_0}g_{00}x_i}_{\text{self-interference}} + \underbrace{\sum_{n=1}^N \sqrt{P_0}g_{0n}\hat{x}_n}_{\text{intf. from neighbor BSs}} \\
 & + \underbrace{\sum_{n=1}^N \sqrt{P_n}f_{0n}\check{x}_n}_{\text{intf. from neighbor UL users}} + n_0.
 \end{aligned} \quad (2)$$

In the FD network, the BS's receiver suffers from severe interferences from the transmitters both the serving and neighbor BSs. (Relatively, we can regard the interferences from the Txs of UL users in the neighboring cells as weak interferences because the transmit power of UE is small and the UL signal is greatly attenuated by the long distance [16–20, 28].) However, the FD BS can remove these interference components through the interference cancellation and channel estimation techniques [4, 28]. For this channel estimation, we suppose that the Rx of the BS utilizes pilot symbols transmitted from the Txs of the serving BS<sub>0</sub> and neighbor BSs. Therefore, the received interference strength can be decreased to a similar level to the noise floor of receiver after sequentially applying analog and digital cancellation schemes [5–8]. In addition, we can estimate the channel coefficients  $g_{00}$  and  $g_{0n}$  by applying an appropriate channel estimation method [29]. (Details about channel estimation

technique are out of the scope in this paper and the channel estimation at the BS is assumed to be perfect.) Based on the knowledge of the signals received from the serving BS<sub>0</sub> and neighbor BSs via the wired backhaul and the interference channel estimation, the Rx of the serving BS<sub>0</sub> can remove such interference components from the received signal. After interference cancellation, the signal of UL user  $j$  is given by

$$\begin{aligned} \hat{y}_j &= \sqrt{P_j} h_{0j} x_j + \sqrt{P_0} (g_{00} - \hat{g}_0) x_i \\ &+ \sum_{n=1}^N \sqrt{P_0} (g_{0n} - \hat{g}_{0n}) \hat{x}_n + \sum_{n=1}^N \sqrt{P_n} f_{0n} \tilde{x}_n + n_0 \end{aligned} \quad (3)$$

where  $\hat{g}_0$  and  $\hat{g}_{0n}$  correspond to the estimated channel coefficients.

Using (1) and (3), the SINRs of the received signals  $y_i$  and  $\hat{y}_j$  are, respectively, given by

$$\Gamma_i = \frac{P_0 \|h_{i0}\|^2}{P_j \|f_{ij}\|^2 + \sum_{n=1}^N P_0 \|g_{in}\|^2 + \sum_{n=1}^N P_n \|f_{in}\|^2 + N_0}, \quad (4)$$

$$\begin{aligned} \Gamma_j &= \frac{P_j \|h_{0j}\|^2}{P_0 \|g_{00} - \hat{g}_0\|^2 + \sum_{n=1}^N P_0 \|g_{0n} - \hat{g}_{0n}\|^2 + \sum_{n=1}^N P_n \|f_{0n}\|^2 + N_0}. \end{aligned} \quad (5)$$

In the conventional HD mode that does not generate self-interference and interuser interference, the SINRs of DL user  $i$  and UL user  $j$  are, respectively, described as

$$\Gamma_i^{\text{HD}} = \frac{P_0 \|h_{i0}\|^2}{\sum_{n=1}^N P_0 \|g_{in}\|^2 + N_0}, \quad (6)$$

$$\Gamma_j^{\text{HD}} = \frac{P_j \|h_{0j}\|^2}{\sum_{n=1}^N P_n \|f_{0n}\|^2 + N_0}. \quad (7)$$

### 3. Proposed User Pairing Algorithm

On the basis of SINR expressions for DL and UL users given as (4) and (5), the controllable parameters are explicitly  $P_j$  and  $f_{ij}$ . The other parameters are generally fixed or are determined by the node position. Here, the channel coefficient  $f_{ij}$  depends on how we pair UL user  $j$  and DL user  $i$  to use the same RB. Namely, the user pairing determines the amount of interuser interference and directly influences the DL SINR  $\Gamma_i$ . In this context, we propose an effective user pairing algorithm to improve the system performance in the considered FD cellular network.

Our objective is to minimize the outage probability. Since the outage occurs when the SINR does not satisfy the required SINR, the outage probabilities of the DL user  $i$  and the UL user  $j$  are, respectively, defined as

$$P_{out}^{\text{DL}} \triangleq \mathbb{P} \{ \Gamma_i < \theta \} \quad \text{for } i \in \{1, 2, \dots, M\}, \quad (8)$$

$$P_{out}^{\text{UL}} \triangleq \mathbb{P} \{ \Gamma_j < \theta \} \quad \text{for } j \in \{1, 2, \dots, M\} \quad (9)$$

where  $\theta$  is the required SINR threshold [30]. For the purpose of minimizing the outage probability of all users, the optimization problem can be formulated as

$$\pi_k = \arg \max_{(i,j) \in \pi_k} \min \{ \Gamma_i, \Gamma_j \} \quad \text{for } i, j \in \{1, 2, \dots, M\}. \quad (10)$$

Here, we denote  $(i, j)$  as a user pair of DL user  $i$  and UL user  $j$  using the same RB and define  $\mathbf{\Pi}$  as the set of all possible user pairs  $(i, j)$  for  $i, j \in \{1, 2, \dots, M\}$ . Also we denote  $\pi_k$  as the  $k$ -th element of  $\mathbf{\Pi}$  where  $k = 1, 2, \dots, M!$ .

Available user pairs are determined by selecting a number  $i$  in  $\{1, 2, \dots, M\}$  and a number  $j$  in  $\{1, 2, \dots, M\}$  under the condition that the selected number cannot be chosen again. Thus, the number of possible configurations for user pairing becomes  $M!$ . For instance of  $M = 3$ ,  $\mathbf{\Pi}$  becomes

$$\mathbf{\Pi} = \begin{bmatrix} \pi_1 \\ \pi_2 \\ \pi_3 \\ \pi_4 \\ \pi_5 \\ \pi_6 \end{bmatrix} = \begin{bmatrix} \{(1, 1), (2, 2), (3, 3)\} \\ \{(1, 1), (2, 3), (3, 2)\} \\ \{(1, 2), (2, 1), (3, 3)\} \\ \{(1, 2), (2, 3), (3, 1)\} \\ \{(1, 3), (2, 1), (3, 2)\} \\ \{(1, 3), (2, 2), (3, 1)\} \end{bmatrix} \quad (11)$$

where six configurations exist. To solve this combinatorial problem, we must search the total  $M!$  configurations. This complexity is  $O(M!)$  and exponentially increases as the number of users ( $M$ ) increases. Hence, we need to design a suboptimal pairing algorithm with low complexity from the practical point of view.

We can have an intuition for designing a new user pairing algorithm from (4) and (5). In (5), the SINR of UL user,  $\Gamma_j$ , is not relevant to DL users. If we suppose that both the interference cancellation and channel estimation are perfect and the interference from neighbor UL users is negligible,  $\Gamma_j$  is affected by mainly UL channel  $h_{0j}$  and UL transmit power  $P_j$ . On the other hand, the SINR of DL user,  $\Gamma_i$ , is relevant to the DL channel ( $h_{i0}$ ), the direct channel from UL user  $j$  to DL user  $i$  ( $f_{ij}$ ), and the UL transmit power ( $P_j$ ). Namely, the user pairing affects the SINR of DL user  $\Gamma_i$  only. Therefore, the first parameter that can be adjusted to reduce the outage is the UL transmit power,  $P_j$ . Since the UL transmission gives the interference to the DL user, it is preferable that the UL user  $j$  controls its transmission power  $P_j$  to satisfy  $\Gamma_j = \theta$ . This UL power control is effective to reduce the interference from UL user to DL user and thus decreases the outage probability of DL users while satisfying the UL SINR requirement.

In addition, to avoid the outage from the perspective of DL users, it is reasonable to make the DL user with a worse signal quality receive less interference [31]. Thus, we make the DL users with a worse signal quality (i.e., a lower value of  $\Gamma_i^{\text{HD}}$ ) select first the UL user causing a smaller interference (i.e.,  $P_j \|f_{ij}\|^2$ ) as its partner. By the way, if the SINR of DL user  $i$ ,  $\Gamma_i$ , is smaller than  $\theta$  although the best UL user is selected by this strategy, the DL user is convinced of its outage and does not finally select the corresponding UL user. Thus, we make this outage DL user yield its option to the next DL user and choose a UL user later among the remaining unpaired UL



```

Ensure:  $\theta =$  SINR threshold
1: Initialize:
    $P_j \leftarrow \frac{\theta N_0}{\|h_{0j}\|^2}, j = 1, 2, \dots, M$ 
    $U_j \leftarrow 0, j = 1, 2, \dots, M$  /* flag for selected or not */
2: Sort the DL users in order of low  $\Gamma_i^{HD}$  value
3: for  $i =$  [sorted DL users] do
4:   Unpaired UL users  $\leftarrow$  find( $U_j = 0$ )
5:   Measure the interference from unpaired UL user  $j$  to DL user  $i$  ( $P_j \|f_{ij}\|^2$ ) where  $j \in \{1, 2, \dots, M\}$ 
6:   Choose the UL user  $j$  causing the smallest interference  $P_j \|f_{ij}\|^2$  among unpaired UL users
7:   if  $\Gamma_i > \theta$  when choosing the UL user  $j$  then
8:      $U_j \leftarrow 1$ 
9:     Complete the user pair ( $i, j$ )
10:  else
11:    Outage DL users  $\leftarrow i$ 
12:  end if
13: end for
14: for  $i =$  [sorted outage DL users] do
15:   Unpaired UL users  $\leftarrow$  find( $U_j = 0$ )
16:   Choose the UL user  $j$  causing the smallest interference  $P_j \|f_{ij}\|^2$  among unpaired UL users
17:    $U_j \leftarrow 1$ 
18:   Complete the user pair ( $i, j$ )
19: end for

```

ALGORITHM 1: Proposed user pairing algorithm.

users. For the outage DL users, the same policy is used with the remaining unpaired UL users in a way of maximizing the minimum SINR. Since this proposed user pairing approach gives more opportunities to the DL users with a lower signal quality, the outage probability can be decreased effectively.

The details of the proposed user pairing algorithm are described as Algorithm 1. Initially, the transmission power of all UL users is set to the minimum value to satisfy the SINR threshold (i.e.,  $P_j = \theta N_0 / \|h_{0j}\|^2$ ), in order to minimize the interuser interference from UL user to DL user. Moreover, the flag means whether the UL user is selected or not and is initially set to zero for all  $j$ . Then, the algorithm sorts the DL users from the lowest to the highest DL SINR value and runs in the order of these sorted DL users. For DL user  $i$ , the pairing algorithm measures the interference from the unpaired UL user  $j$  to the DL user  $i$ ,  $P_j \|f_{ij}\|^2$ . Thereafter, the UL user with the smallest interuser interference  $P_j \|f_{ij}\|^2$  among the unpaired UL users is chosen for pairing. If the DL SINR for this selected pair is greater than the SINR threshold, the flag of this UL user  $j$  is set to one. Namely, the DL user  $i$  and selected UL user  $j$  become a partner with each other. Otherwise, the DL user  $i$  belongs to the outage DL user. This pairing operation is iterated until all DL users are handled. If there is any outage DL user, there is additional user pairing between the outage DL users and the unpaired UL users. The rule is the same as Lines 3-13, but there is no requirement to satisfy the SINR threshold, as shown. In this way, the user pairing is completed to minimize the outage of all users. Notice that the proposed pairing algorithm performs one iteration and one search in each iteration for  $M$  users; thus, its

computational complexity is  $O(M^2)$ , which is much less than the complexity of an exhaustive search (i.e.,  $O(M!)$ ).

For designing the proposed pairing algorithm, we assumed that the number of DL users and UL users are the same and the BS knows the necessary channel information. However, if the number of DL users and UL users is different, the excess link users will not be able to participate in pairing for FD and will have to operate in HD mode. This can lead to performance degradation. In addition, for the operation of the proposed algorithm, the UL user must report the amount of interference received from each DL user to the BS. This results in UL feedback overhead. Therefore, to realize the proposed pairing algorithm in an actual environment, we need to consider these practical issues to reduce such performance degradation and overhead, which are left as a future study.

## 4. Outage Analysis

**4.1. Notations and Assumptions.** For the analysis based on stochastic geometry, we suppose a homogeneous cellular network consisting of macrocell BSs and users [19]. The BSs are arranged in accordance with a Poisson point process (PPP) of density  $\lambda$  in the Euclidean plane [32, 33]. We also suppose that both DL and UL users are distributed independently with a homogeneous PPP of the same density  $\lambda$ . Therefore, the BS allocates one DL user and one UL user simultaneously during a given RB [33, 34]. And each user is associated with its nearest BS.

Figure 2 exhibits the system model where an FD BS<sub>0</sub> serves its DL user  $u_0$  and UL user  $u_1$  at the same time.

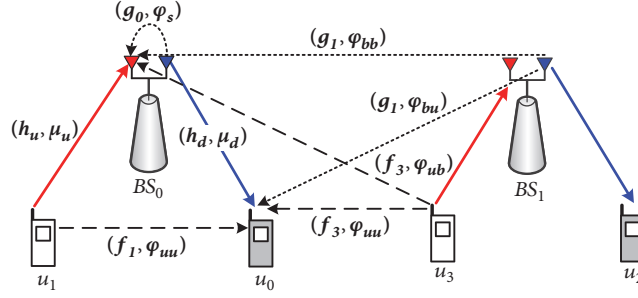


FIGURE 2: System model and notations.

$u_0$  experiences interferences from  $u_1$ ,  $u_3$ , and  $BS_1$  and  $u_1$  experiences interferences from  $u_3$ ,  $BS_0$ , and  $BS_1$  while  $u_0$  receives and  $u_1$  transmits a signal from and to a  $BS_0$  simultaneously. Solid line with  $(h, \cdot)$  indicates the signal channel, dotted line with  $(g, \cdot)$  indicates the interference channels by the neighboring BSs, and dashed line with  $(f, \cdot)$  denotes the interference channels by users. Here, we suppose that a serving BS and its users experience Rayleigh fading with unit mean and they use a fixed transmission power of  $1/\mu$ . Moreover, the received signal strength at a certain node with a distance  $r$  to its BS is set to  $hr^{-\alpha}$  where  $h$  follows an Exponential distribution with mean  $1/\mu$  (i.e.,  $h \sim \exp(\mu)$ ), which is denoted as  $(h, \mu)$ . Also the path loss exponent of all BSs and users is denoted as  $\alpha$ , and additive noise power is set to  $\sigma^2$ . All results are limited to the case of a single transmit/receive antenna.

**4.2. Downlink Outage Probability.** When a DL user,  $u_0$ , has a distance  $r$  and fading strength  $h_d \sim \exp(\mu_d)$  from its serving BS,  $u_0$  receives a signal with a strength of  $h_d r^{-\alpha}$ . Moreover,  $u_0$  receives cumulative interference  $I_b$  and  $I_u$  from its neighbors. Here,  $I_b$  represents the total sum of the received powers from all neighboring BSs. When  $u_0$  has a distance  $r_i$  and fading strength  $g_i \sim \exp(\varphi_{bu})$  from the neighboring BS  $i$ ,  $I_b$  is expressed as

$$I_b = \sum_{i \in \Phi_b} g_i r_i^{-\alpha} \quad (12)$$

where  $\Phi_b$  denotes the set of all interfering BSs. Moreover,  $I_u$  represents the total sum of the received powers from all other UL users. When  $u_0$  has a distance  $r_i$  and fading strength  $f_i \sim \exp(\varphi_{uu})$  from the other UL user  $i$ ,  $I_u$  is expressed as

$$I_u = \sum_{i \in \Omega_u} f_i r_i^{-\alpha} \quad (13)$$

where  $\Omega_u$  is the set of all interfering users. Then, the SINR of DL user  $u_0$  is given by

$$\Gamma_{DL} = \frac{h_d r^{-\alpha}}{I_b + I_u + \sigma^2}. \quad (14)$$

The outage probability of DL user is exactly represented as the cumulative distribution function (CDF) of SINR over the entire network, as follows.

$$P_{out}^{DL}(\lambda, \theta) = \mathbb{P}[\Gamma_{DL} < \theta]. \quad (15)$$

Since the probability that the nearest BS has a distance  $r$  being  $e^{-\lambda \pi r^2} 2\pi \lambda r$ , the outage probability is formulated as

$$\begin{aligned} P_{out}^{DL}(\lambda, \theta) &= 1 - \int_{r>0} \mathbb{P}[h_d \geq \theta r^\alpha (I_b + I_u + \sigma^2) | r] \\ &\cdot e^{-\lambda \pi r^2} 2\pi \lambda r dr = 1 - \int_{r>0} e^{-\lambda \pi r^2 - \mu_d \theta r^\alpha \sigma^2} \\ &\cdot \mathcal{L}_{I_b}(\mu_d \theta r^\alpha) \cdot \mathcal{L}_{I_u}(\mu_d \theta r^\alpha) \cdot 2\pi \lambda r dr. \end{aligned} \quad (16)$$

Here, the Laplace transform of  $I_b$  is calculated as

$$\begin{aligned} \mathcal{L}_{I_b}(\mu_d \theta r^\alpha) &= \exp\left(-2\pi \lambda \int_r^\infty \left(1 - \frac{\varphi_{bu}}{\varphi_{bu} + \mu_d \theta r^\alpha v^{-\alpha}}\right) v dv\right) \\ &= \exp\left(-2\pi \lambda \int_r^\infty \frac{\beta_{d,bu} \theta}{\beta_{d,bu} \theta + (v/r)^\alpha} v dv\right) \\ &= \exp\left(-2\pi \lambda \int_r^\infty \frac{1}{1 + (\beta_{d,bu} \theta)^{-1} (v/r)^\alpha} v dv\right) \\ &= \exp(-\pi r^2 \lambda \rho_{db}(\theta)) \end{aligned} \quad (17)$$

where  $\rho_{db}(\theta) = (\beta_{d,bu} \theta)^{2/\alpha} \int_{(\beta_{d,bu} \theta)^{-2/\alpha}}^\infty 1/(1 + u^{\alpha/2}) du$  is used for calculation. In the same way, the Laplace transform of  $I_u$  is obtained as

$$\mathcal{L}_{I_u}(\mu_d \theta r^\alpha) = \exp(-\pi r^2 \lambda \rho_{du}(\theta)) \quad (18)$$

where  $\rho_{du}(\theta) = (\beta_{d,uu} \theta)^{2/\alpha} \int_0^\infty 1/(1 + u^{\alpha/2}) du$ .

Therefore, when a randomly located mobile user experiences Exponential interference, the outage probability for DL users is characterized as

$$\begin{aligned} P_{out}^{DL}(\lambda, \theta) &= 1 - \int_{r>0} e^{-\lambda \pi r^2 - \mu_d \theta r^\alpha \sigma^2} \cdot e^{-\pi r^2 \lambda \rho_{db}(\theta)} \\ &\cdot e^{-\pi r^2 \lambda \rho_{du}(\theta)} \cdot 2\pi \lambda r dr = 1 \\ &- \pi \lambda \int_0^\infty e^{-\lambda \pi v(1 + \rho_{db}(\theta) + \rho_{du}(\theta)) - \mu_d \theta \sigma^2 v^{\alpha/2}} dv. \end{aligned} \quad (19)$$

4.3. *Uplink Outage Probability.* When a UL user  $u_1$  has a distance  $r$  and fading strength  $h_u \sim \exp(\mu_u)$  to its serving BS,  $u_1$  receives a signal with a strength of  $h_u r^{-\alpha}$ . In addition,  $u_1$  receives cumulative interference  $I_b$ ,  $I_u$ , and  $I_s$ . Here,  $I_b$  represents the total sum of the received powers from all neighboring BSs. When the serving BS of  $u_1$  has a distance  $r_i$  and fading strength  $g_i \sim \exp(\varphi_{bb})$  from the neighboring BS  $i$ ,  $I_b$  is expressed as

$$I_b = \sum_{i \in \Phi_b} g_i r_i^{-\alpha} \quad (20)$$

where  $\Phi_b$  is the set of all interfering BSs. Moreover,  $I_u$  represents the total sum of the received powers from all other UL users. When the serving BS of  $u_1$  has a distance  $r_i$  and fading strength  $f_i \sim \exp(\varphi_{ub})$  from the interfering UL user  $i$ ,  $I_u$  is expressed as

$$I_u = \sum_{i \in \Omega_u} f_i r_i^{-\alpha} \quad (21)$$

where  $\Omega_u$  is the set of all interfering users. Also,  $I_s$  indicates the self-interference in the serving BS of user  $u_1$  and we simply assume that  $I_s$  becomes  $\eta$  times as much as the noise power (i.e.,  $I_s = \eta\sigma^2$ ). Therefore, the SINR of typical UL user  $u_1$  is given by

$$\Gamma_{UL} = \frac{h_u r^{-\alpha}}{I_b + I_u + I_s + \sigma^2}. \quad (22)$$

The outage probability of UL user is exactly represented as the CDF of SINR over the entire network, as follows.

$$P_{out}^{UL}(\lambda, \theta) = \mathbb{P}[\Gamma_{UL} < \theta]. \quad (23)$$

Since the probability that the closest BS has a distance  $r$  being  $e^{-\lambda\pi r^2} 2\pi\lambda r$ , the outage probability is formulated as

$$\begin{aligned} P_{out}^{UL}(\lambda, \theta) &= 1 \\ &- \int_{r>0} \mathbb{P}[h_u \geq \theta r^\alpha (\sigma^2 + I_b + I_u + I_s) \mid r] \\ &\cdot e^{-\lambda\pi r^2} 2\pi\lambda r dr = 1 - \int_{r>0} e^{-\lambda\pi r^2 - \mu_u \theta r^\alpha (\sigma^2 + \eta\sigma^2)} \\ &\cdot \mathcal{L}_{I_b}[\mu_u \theta r^\alpha] \cdot \mathcal{L}_{I_u}[\mu_u \theta r^\alpha] \cdot 2\pi\lambda r dr. \end{aligned} \quad (24)$$

Here, the Laplace transform of  $I_b$  is calculated as

$$\begin{aligned} \mathcal{L}_{I_b}(\mu_u \theta r^\alpha) &= \exp\left(-2\pi\lambda \int_r^\infty \left(1 - \frac{\varphi_{bb}}{\varphi_{bb} + \mu_u \theta r^\alpha v^{-\alpha}}\right) v dv\right) \quad (25) \\ &= \exp\left(-2\pi\lambda \int_r^\infty \frac{\beta_{u,bb}\theta}{\beta_{u,bb}\theta + (v/r)^\alpha} v dv\right) \quad (26) \\ &= \exp\left(-2\pi\lambda \int_r^\infty \frac{1}{1 + (\beta_{u,bb}\theta)^{-1} (v/r)^\alpha} v dv\right) \quad (27) \\ &= \exp(-\pi r^2 \lambda \rho_{ub}(\theta)) \quad (28) \end{aligned}$$

where  $\rho_{ub}(\theta) = (\beta_{u,bb}\theta)^{2/\alpha} \int_{(\beta_{u,bb}\theta)^{-2/\alpha}}^\infty 1/(1 + u^{\alpha/2}) du$ . In the same way, the Laplace transform of  $I_u$  is calculated as

$$\mathcal{L}_{I_u}(\mu_u \theta r^\alpha) = \exp(-\pi r^2 \lambda \rho_{uu}(\theta)) \quad (29)$$

where  $\rho_{uu}(\theta) = (\beta_{u,ub}\theta)^{2/\alpha} \int_{(\beta_{u,ub}\theta)^{-2/\alpha}}^\infty 1/(1 + u^{\alpha/2}) du$ .

When a randomly located mobile user experiences exponential interference, the outage probability of UL users is finally characterized as

$$\begin{aligned} P_{out}^{UL}(\lambda, \theta) &= 1 - \int_{r>0} e^{-\lambda\pi r^2 - \mu_u \theta r^\alpha (\sigma^2 + \eta\sigma^2)} \cdot e^{-\pi r^2 \lambda \rho_{ub}(\theta)} \\ &\cdot e^{-\pi r^2 \lambda \rho_{uu}(\theta)} \cdot 2\pi\lambda r dr = 1 \\ &- \pi\lambda \int_0^\infty e^{-\lambda\pi v(1 + \rho_{ub}(\theta) + \rho_{uu}(\theta)) - \mu_u \theta (\sigma^2 + \eta\sigma^2) v^{\alpha/2}} dv. \end{aligned} \quad (30)$$

## 5. Results and Discussions

For comparison, we consider (1) the typical *HD mode* where the BS does not employ the FD mode and the DL and UL resources are equally divided [35], (2) the FD with the *random pairing* that pairs a DL user with a UL user randomly, (3) *maximizing throughput (MaxThr)* method proposed in [18, 19] that determines the user pairs in a way that the DL user with better channel quality receives a smaller inter-user interference for the purpose of maximizing the sum throughput, and (4) the FD with the *optimal pairing* that optimally pairs users by exhaustive search. For a fair comparison, because the HD mode uses only half of the resource, its SINR,  $\Gamma^{\text{HD}}$  in (6) and (7), is recalculated as  $\Gamma_{\text{new}}^{\text{HD}} = \sqrt{1 + \Gamma^{\text{HD}}} - 1$  from the relationship of  $\log(1 + \Gamma_{\text{new}}^{\text{HD}}) = (1/2) \log(1 + \Gamma^{\text{HD}})$ , and its outage probability is redefined as  $P_{out}^{\text{HD}} \triangleq \mathbb{P}\{(1/2) \log(1 + \Gamma^{\text{HD}}) < \log(1 + \theta)\}$ .

The parameters used for evaluation are listed in Table 1 [19]. We evaluate the system rate by varying the user density  $\lambda$  from 0.1 to 1. Here, the users with  $\lambda = 1$  correspond to the density of one user in 100  $m^2$  on average [34]. Also we use the same network configuration in the simulation as in the analysis [28]. The same number of DL and UL users is distributed randomly with varying the density  $\lambda$  in the multicell coverage. We consider the SINR threshold of 0 dB by default and change its range from -10 to 40 dB to determine the outage performance. Here, the channel parameter from UL user to serving BS,  $\mu_u$ , and the channel parameter from UL user to DL user,  $\varphi_{uu}$ , are affected by user pairing algorithms so that their values are determined by the simulation after applying each user pairing algorithm. Moreover, we set the associated channel values (i.e.,  $\varphi_{bu}$ ,  $\varphi_{ub}$ , and  $\varphi_{bb}$ ) to be large enough to minimize the influence from neighboring cells.

Figure 3(a) plots the CDF of the interuser interference when the number of DL/UL users ( $M$ ) is 10 and the SINR threshold ( $\theta$ ) is 0 dB. The distribution of interuser interference is important to check whether the user pairing algorithm operates properly. Here, the interuser interference level is measured by simulation when each user pairing

TABLE 1: Parameter setup.

Parameter	Description	Value
$\lambda$	User density	0.1~1 (default=0.5)
$\theta$	SINR threshold	-10~40 dB (default=0 dB)
$\sigma^2$	Noise power	1
$\alpha$	Path loss exponent	2~4 (default=3)
$\eta$	Self-interference ratio	0~10 (default=0)
$\mu_d$	Channel parameter from serving BS to DL user	0.01
$\mu_u$	Channel parameter from UL user to serving BS	0.01~1 (determined by simulation)
$\varphi_{bu}$	Channel parameter from neighbor BS to DL user	100
$\varphi_{ub}$	Channel parameter from neighbor UL user to serving BS	100
$\varphi_{bb}$	Channel parameter from neighbor BS to serving BS	100
$\varphi_{uu}$	Channel parameter from UL user to DL user	1~100 (determined by simulation)

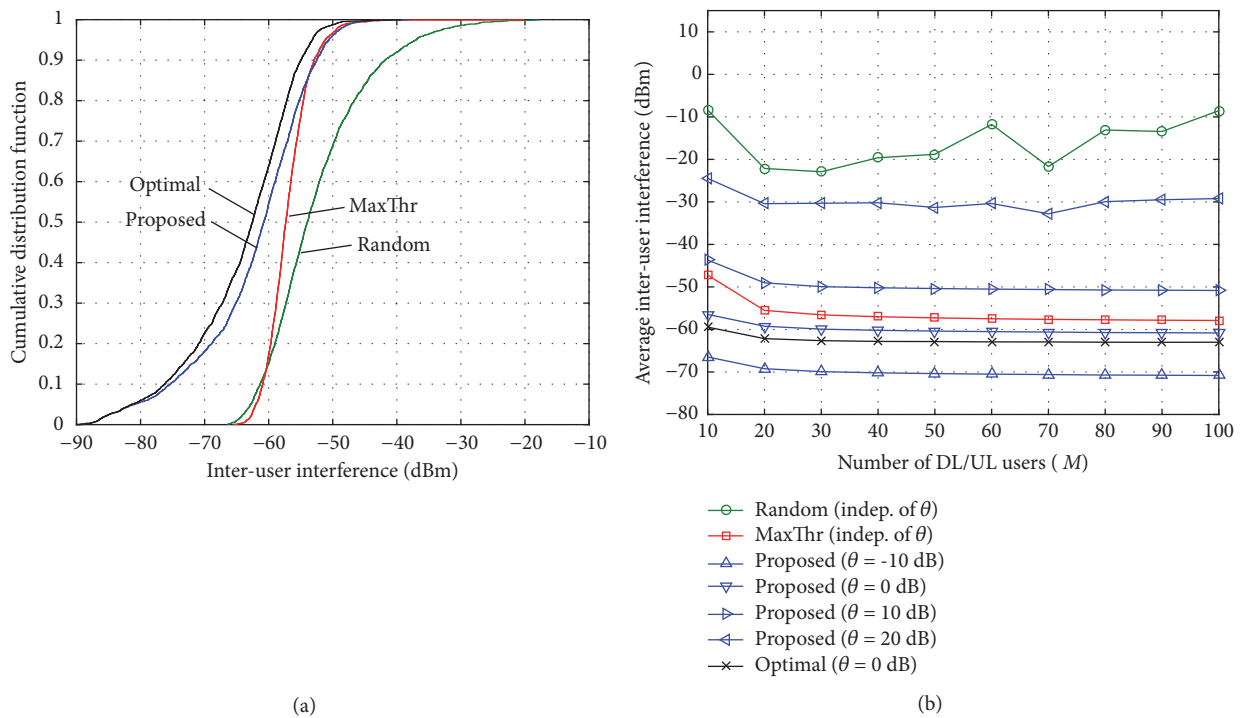


FIGURE 3: (a) CDF of interuser interference when  $M = 10$  and  $\theta = 0$  dB and (b) average inter-user interference versus number of DL/UL users ( $M$ ).

algorithm is applied. Compared with the random pairing, the proposed pairing algorithm significantly decreases the interuser interference. This is because the proposed pairing selects the UL user with low interference as much as possible by considering the amount of interuser interference. Moreover, the proposed pairing shows even smaller interuser interference than MaxThr because it uses UL transmit power control and so reduces the interuser interference to the DL users effectively. Note that there is a slight difference between the proposed and the optimal pairing algorithms.

Figure 3(b) exhibits the average inter-user interference level versus the number of DL/UL users,  $M$ . At  $\theta = 0$  dB, the proposed pairing is much better than the random pairing and is slightly better than MaxThr, regardless of the number

of users, as shown in Figure 3(a). Note that the interuser interference in the random and MaxThr pairing algorithms are independent of the SINR threshold  $\theta$ . However, the SINR threshold affects the transmit power of UL users in the proposed pairing. That is, the higher is the SINR threshold, the greater is the UL transmit power. Thus, the average interuser interference level increases as the SINR threshold increases in the proposed algorithm. Overall, the interuser interference decreases slightly when the number of users initially increases because the user diversity occurs as the number of users increases and so MaxThr and the proposed algorithm have more chance to have a user pair with less interuser interference. On the other hand, in the case of the random pairing, the interuser interference is

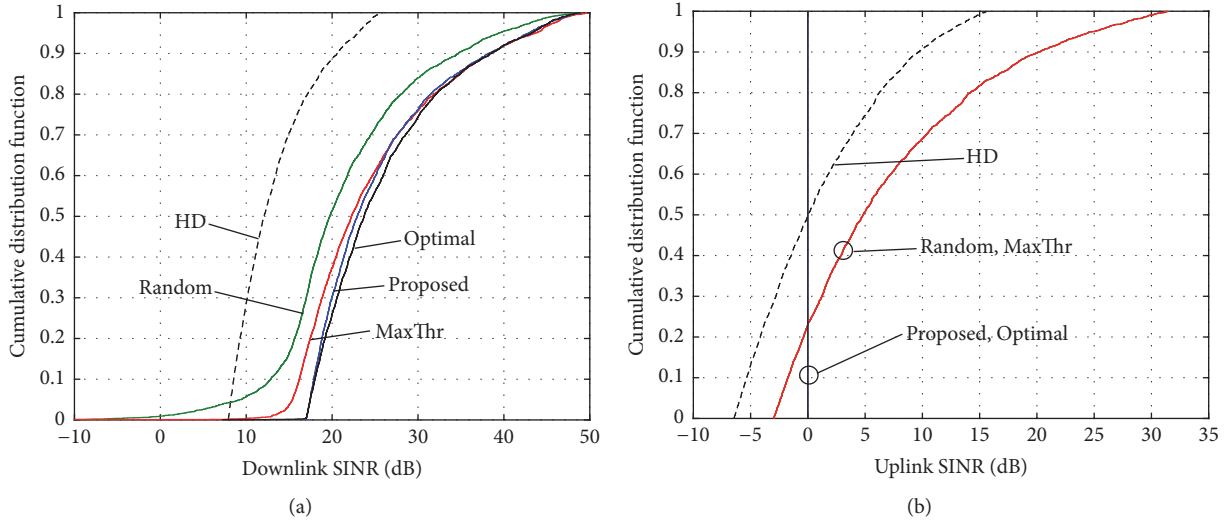


FIGURE 4: (a) CDF of DL SINR and (b) CDF of UL SINR when  $M = 10$  and  $\theta = 0$  dB.

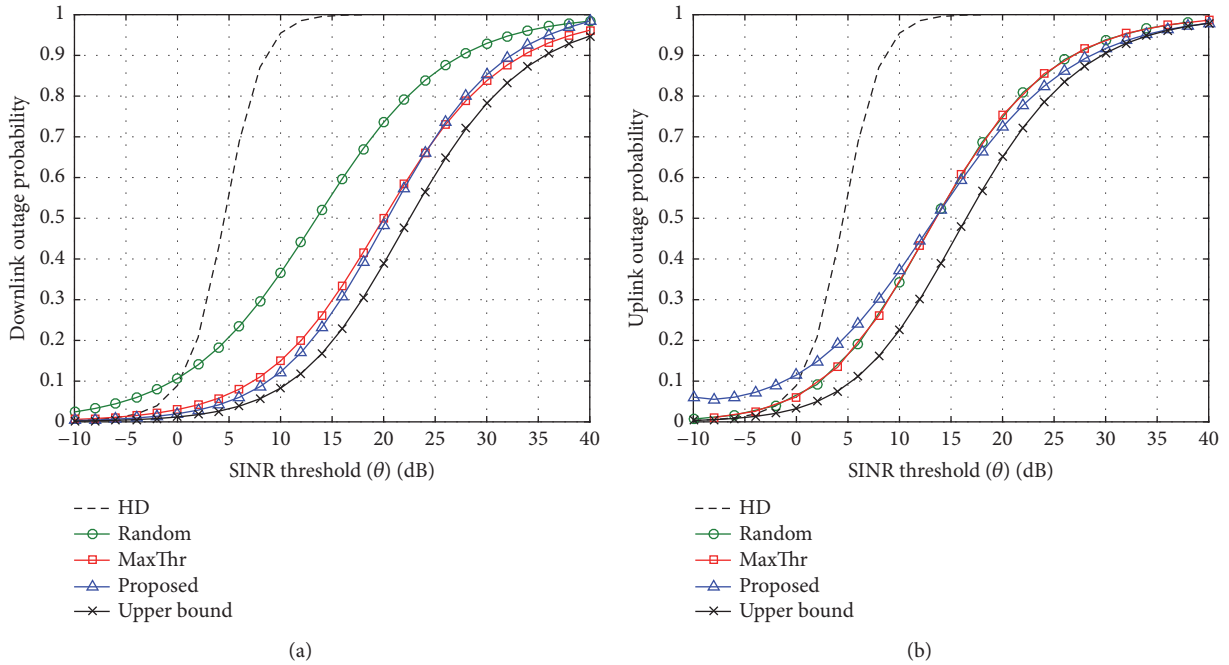


FIGURE 5: (a) DL outage probability and (b) UL outage probability versus SINR threshold ( $\theta$ ) when  $\lambda = 0.5$ .

fluctuated between -8 and -22 dBm because it often generates uncontrolled stronger interferences between the randomly selected DL and UL users as the number of users increases.

Figure 4 plots the CDF of the DL SINR and UL SINR when  $M = 10$  and  $\theta = 0$  dB. In the case of DL SINR, the proposed pairing shows better SINR than MaxThr and random pairing because it experiences the lower interuser interference. The HD mode has a significantly lower SINR and also the proposed scheme is close to optimal. In the case of UL SINR, the proposed and optimal pairing algorithms show that all UL users have the same UL SINR as 0 dB because their UL transmit power is adjusted to the SINR threshold.

This result clearly shows that the proposed pairing algorithm significantly improves the DL SINR at the expense of the UL SINR to minimize the outage probability.

Figure 5 shows the DL and UL outage probabilities versus the SINR threshold when  $\lambda$  is fixed to 0.5. These outage probabilities are obtained from the numerical analysis in Section 4 and the used channel parameters for this result are derived from the simulation of the considered user pairing algorithms. Here, the performance of upper bound indicates the perfect FD assuming that there is no interuser interference and the reduction of UL transmit power. The proposed pairing algorithm improves the DL

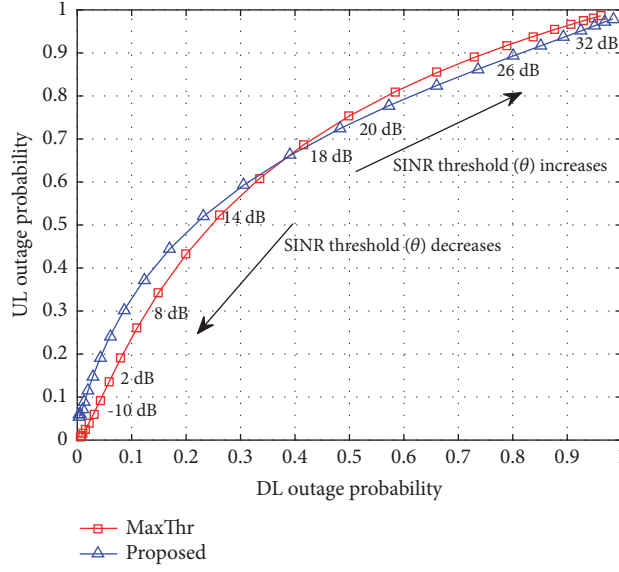


FIGURE 6: UL outage probability versus DL outage probability according to the change of SINR threshold ( $\theta$ ).

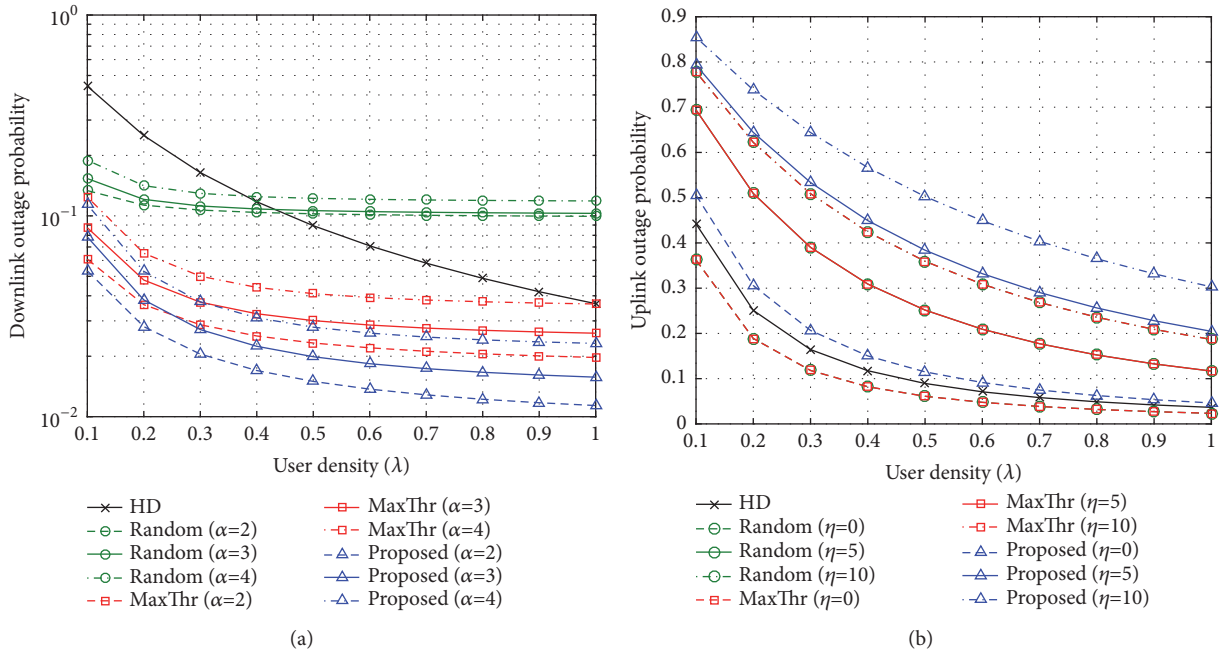


FIGURE 7: (a) DL outage probability and (b) UL outage probability versus user density ( $\lambda$ ) when  $\theta = 0$  dB.

outage probability compared to the random pairing. The random pairing and MaxThr pairing have the same UL outage probability because they do not control UL transmit power equally. Compared to MaxThr, the proposed scheme shows the tradeoff performance according to the SINR threshold. When the SINR threshold is small, the DL outage of the proposed pairing is better than that of MaxThr but the UL outage is not. On the contrary, when the SINR threshold is large, the UL outage of the proposed pairing is better than that of MaxThr but the DL outage is not. As the SINR threshold increases, the proposed pairing should increase

the UL transmit power to satisfy the UL SINR requirement. This decreases the UL outage probability, but increases the interuser interference, thereby increasing the DL outage probability.

Figure 6 plots the UL outage probability versus the DL outage probability as the SINR threshold changes from -10 to 40 dB. This graph clearly shows the tradeoff performance between MaxThr and the proposed pairing according to the SINR threshold. As the SINR threshold decreases, the proposed pairing decreases the UL transmit power to satisfy the UL SINR requirement. This eventually decreases

the interuser interference and so decreases the DL outage probability. Therefore, the proposed scheme has the smaller DL outage than the MaxThr scheme when the SINR threshold decreases. On the contrary, as the SINR threshold increases, the proposed pairing increases the UL transmit power, which increases the interuser interference; thereby increasing the DL outage probability. Hence, the proposed scheme shows the smaller UL outage of the MaxThr scheme when the SINR threshold increases. Therefore, there exists a cross point between two schemes and there is a fundamental tradeoff between the DL outage and UL outage performances in the considered user pairing algorithms in the FD cellular network.

Figure 7 shows the DL and UL outage probabilities versus the user density ( $\lambda$ ) when  $\theta$  is fixed to 0 dB according to the variation of related parameters: path loss exponent ( $\alpha$ ) and self-interference ratio ( $\eta$ ). The user density corresponds to the number of users and means how many pairing opportunities are given. Thus, the outage probabilities decrease as the user density increases. Regarding the path loss exponent  $\alpha$ , the DL outage probability in all schemes increases as  $\alpha$  increases because all SINRs become smaller with the greater  $\alpha$ . Regarding the self-interference ratio,  $\eta$  greater than zero means that there remains the self-interference at the BS using FD. Thus, the UL outage probability increases in all the FD schemes as  $\eta$  increases. This implies that the UL outage performance depends heavily on the SIC capability at the BS.

## 6. Conclusion

In this study, we dealt with user pairing problems in FD cellular networks. We proposed a low-complexity user pairing algorithm to minimize outage probability. The proposed pairing algorithm was invented in a way that the UL user reduces its transmit power to satisfy the SINR threshold for minimizing the interuser interference and the DL user with a worse signal quality preferentially selects its UL user who gives less interference for outage minimization. The simulation and analysis results showed that the proposed algorithm significantly decreased the interuser interference and thus improves the DL outage performance while satisfying the UL SINR requirement, compared to the conventional HD mode and a random user pairing. It is also observed that there is a tradeoff between the DL outage and UL outage probabilities according to the user pairing strategy. We expect that the considered user pairing algorithms and their analysis results will be applicable for the protocol design and implementation of the future FD cellular network.

## Data Availability

The data used to support the findings of this study are available from the corresponding author upon request.

## Conflicts of Interest

The authors declare that there are no conflicts of interest regarding the publication of this paper.

## Acknowledgments

This research was supported in part by the Basic Science Research Program through the National Research Foundation of Korea (NRF) funded by the Ministry of Science, ICT & Future Planning (NRF-2016R1C1B1016261) and in part by ‘The Cross-Ministry Giga KOREA Project’ grant funded by the Korea government (MSIT) (no. GK18S0400, Research and Development of Open 5G Reference Model).

## References

- [1] R. Li, Y. Chen, G. Y. Li, and G. Liu, “Full-Duplex Cellular Networks,” *IEEE Communications Magazine*, vol. 55, no. 4, pp. 184–191, 2017.
- [2] G. Noh, H. Wang, C. Shin et al., “Enabling Technologies toward Fully LTE-Compatible Full-Duplex Radio,” *IEEE Communications Magazine*, vol. 55, no. 3, pp. 188–195, 2017.
- [3] S. Hong, J. Brand, J. Choi II et al., “Applications of self-interference cancellation in 5G and beyond,” *IEEE Communications Magazine*, vol. 52, no. 2, pp. 114–121, 2014.
- [4] D. Bharadia, E. McMillin, and S. Katti, “Full duplex radios,” in *Proceedings of the Annual Conference of the ACM Special Interest Group on Data Communication on the Applications, Technologies, Architectures, and Protocols for Computer Communication (ACM SIGCOMM '13)*, vol. 43, no. 4, pp. 375–386, Hong Kong, August 2013.
- [5] J. Choi II, M. Jain, K. Srinivasan, P. Levis, and S. Katti, “Achieving single channel, full duplex wireless communication,” in *Proceedings of the 16th Annual Conference on Mobile Computing and Networking (MobiCom '10)*, pp. 1–12, ACM, September 2010.
- [6] M. Duarte and A. Sabharwal, “Full-duplex wireless communications using off-the-shelf radios: feasibility and first results,” in *Proceedings of the 44th Asilomar Conference on Signals, Systems and Computers (Asilomar '10)*, pp. 1558–1562, IEEE, Pacific Grove, Calif, USA, November 2010.
- [7] Huawei, “Full-duplex technology for 5G,” *Huawei Innovation Research Program J*, pp. 62–69, 2015.
- [8] M. Chung, M. S. Sim, J. Kim, D. K. Kim, and C.-B. Chae, “Prototyping real-time full duplex radios,” *IEEE Communications Magazine*, vol. 53, no. 9, pp. 56–63, 2015.
- [9] Z. Liu, Y. Liu, and F. Liu, “Joint resource scheduling for full-duplex cellular system,” in *Proceedings of the 22nd International Conference on Telecommunications (ICT '15)*, pp. 85–90, Sydney, Australia, April 2015.
- [10] M. Al-Imari, M. Ghorashi, P. Xiao, and R. Tafazolli, “Game theory based radio resource allocation for full-duplex systems,” in *Proceedings of the 81st IEEE Vehicular Technology Conference (VTC Spring '15)*, pp. 1–5, Scotland, UK, May 2015.
- [11] Y. Sun, D. W. Ng, and R. Schober, “Multi-Objective Optimization for Power Efficient Full-Duplex Wireless Communication Systems,” in *Proceedings of the GLOBECOM 2015 - 2015 IEEE Global Communications Conference*, pp. 1–6, San Diego, CA, USA, December 2015.
- [12] X. Huang, K. Yang, F. Wu, and S. Leng, “Power Control for Full-Duplex Relay-Enhanced Cellular Networks with QoS Guarantees,” *IEEE Access*, vol. 5, pp. 4859–4869, 2017.
- [13] J. F. Shi, M. Chen, Z. H. Yang, H. Xu, and Y. Wang, “Power control and performance analysis for full-duplex relay-assisted D2D communication underlying fifth generation cellular networks,” *IET Communications*, vol. 11, no. 18, pp. 2729–2734, 2017.

- [14] J. M. B. Da Silva, G. Fodor, and C. Fischione, "Fast-Lipschitz Power Control and User-Frequency Assignment in Full-Duplex Cellular Networks," *IEEE Transactions on Wireless Communications*, vol. 16, no. 10, pp. 6672–6687, 2017.
- [15] D. Kim, H. Lee, and D. Hong, "A survey of in-band full-duplex transmission: from the perspective of PHY and MAC layers," *IEEE Communications Surveys & Tutorials*, vol. 17, no. 4, pp. 2017–2046, 2015.
- [16] Q. Gao, G. Chen, L. Liao, and Y. Hua, "Full-duplex cooperative transmission scheduling in fast-fading MIMO relaying wireless networks," in *Proceedings of the International Conference on Computing, Networking and Communications (ICNC '14)*, pp. 771–775, Honolulu, Hawaii, USA, February 2014.
- [17] G. Yu, D. Wen, and F. Qu, "Joint user scheduling and channel allocation for cellular networks with full duplex base stations," *IET Communications*, vol. 10, no. 5, pp. 479–486, 2016.
- [18] H.-H. Choi, "On the design of user pairing algorithms in full duplexing wireless cellular networks," in *Proceedings of the 5th International Conference on Information and Communication Technology Convergence (ICTC '14)*, pp. 490–495, Busan, Korea, October 2014.
- [19] W. Noh, W. Shin, and H.-H. Choi, "Performance Analysis of User Pairing Algorithm in Full-Duplex Cellular Networks," *Hindawi Mobile Information Systems*, vol. 2017, Article ID 8182150, 12 pages, 2017.
- [20] R. Sultan, L. Song, K. G. Seddik, Y. Li, and Z. Han, "Mode selection, user pairing, subcarrier allocation and power control in full-duplex OFDMA HetNets," in *Proceedings of the 2015 ICC - 2015 IEEE International Conference on Communications Workshops (ICC)*, pp. 210–215, London, United Kingdom, June 2015.
- [21] N. Aggarwal, R. S. Manickam, and C. S. R. Murthy, "Cross-layer user pairing for CSM in IEEE 802.16 networks," *IEEE Communications Letters*, vol. 15, no. 5, pp. 515–517, 2011.
- [22] S. N. Islam, "Optimal user pairing to improve the sum rate of a pairwise AF multi-way relay network," *IEEE Wireless Communications Letters*, vol. 4, no. 3, pp. 261–264, 2015.
- [23] Y. Zeng, H. Hu, T. Xu, and B. Jia, "User Pairing Stability in D2D-Relay Networks," *IEEE Communications Letters*, vol. 21, no. 10, pp. 2278–2281, 2017.
- [24] W. Liang, Z. Ding, Y. Li, and L. Song, "User Pairing for Downlink Non-Orthogonal Multiple Access Networks Using Matching Algorithm," *IEEE Transactions on Communications*, vol. 65, no. 12, pp. 5319–5332, 2017.
- [25] J. He and Z. Tang, "Low-complexity user pairing and power allocation algorithm for 5G cellular network non-orthogonal multiple access," *IEEE Electronics Letters*, vol. 53, no. 9, pp. 626–627, 2017.
- [26] Y. Zhang and J. Ge, "Impact analysis for user pairing on NOMA-based energy harvesting relaying networks with imperfect CSI," *IET Communications*, vol. 12, no. 13, pp. 1609–1614, 2018.
- [27] A. Sarkar, P. P. Chakrabarti, and R. Kumar, "Frame-based proportional round-robin," *IEEE Transactions on Computers*, vol. 55, no. 9, pp. 1121–1129, 2006.
- [28] X. Shen, X. Cheng, L. Yang, M. Ma, and B. Jiao, "On the design of the scheduling algorithm for the full duplexing wireless cellular network," in *Proceedings of the IEEE Global Communications Conference (GLOBECOM '13)*, pp. 4970–4975, IEEE, Atlanta, Ga, USA, December 2013.
- [29] M. Jain, J. I. Choi, T. Kim et al., "Practical, real-time, full duplex wireless," in *Proceedings of the 17th Annual International Conference on Mobile Computing and Networking (MobiCom '11)*, pp. 301–312, ACM, Las Vegas, Nev, USA, September 2011.
- [30] I.-H. Lee, "Outage analysis and power allocation for distributed space-time coding-based cooperative systems over rayleigh fading channels," *Journal of Information and Communication Convergence Engineering*, vol. 15, no. 1, pp. 21–27, 2017.
- [31] H.-H. Choi and J.-R. Lee, "Distributed transmit power control for maximizing end-to-end throughput in wireless multi-hop networks," *Wireless Personal Communications*, vol. 74, no. 3, pp. 1033–1044, 2014.
- [32] J. G. Andrews, F. Baccelli, and R. K. Ganti, "A tractable approach to coverage and rate in cellular networks," *IEEE Transactions on Communications*, vol. 59, no. 11, pp. 3122–3134, 2011.
- [33] T. D. Novlan, H. S. Dhillon, and J. G. Andrews, "Analytical modeling of uplink cellular networks," *IEEE Transactions on Wireless Communications*, vol. 12, no. 6, pp. 2669–2679, 2013.
- [34] S. Goyal, P. Liu, S. Hua, and S. Panwar, "Analyzing a full-duplex cellular system," in *Proceedings of the 47th Annual Conference on Information Sciences and Systems (CISS '13)*, pp. 1–6, IEEE, Baltimore, Md, USA, March 2013.
- [35] H.-H. Choi, "Adaptive and prioritized random access and resource allocation schemes for dynamic TDMA/TDD protocols," *Journal of Information and Communication Convergence Engineering*, vol. 15, no. 1, pp. 28–36, 2017.



## Research Article

# Implementation and Field Trials of OFDM-Based Digital Video Broadcasting System in Commercial Broadcasting Network for Multichannel UHD Service

Sang-Jung Ra,<sup>1</sup> Myung-Sun Baek ,<sup>1</sup> Jin-Hyuk Song,<sup>1</sup> Dong-Joon Choi,<sup>1</sup> Joon-Young Jung,<sup>1</sup> and Cheol-Sung Kim<sup>2</sup>

<sup>1</sup>Media Transmission Research Group, Electronics and Telecommunication Research Institute (ETRI), Daejeon, Republic of Korea

<sup>2</sup>Electronics and Communication Engineering, Chonnam National University, Republic of Korea

Correspondence should be addressed to Myung-Sun Baek; [sabman@etri.re.kr](mailto:sabman@etri.re.kr)

Received 5 October 2018; Accepted 10 December 2018; Published 1 January 2019

Guest Editor: Seok-Chul Kwon

Copyright © 2019 Sang-Jung Ra et al. This is an open access article distributed under the Creative Commons Attribution License, which permits unrestricted use, distribution, and reproduction in any medium, provided the original work is properly cited.

This paper describes design and implementation of an OFDM-based digital video broadcasting system test platform for multichannel ultra-high definition (UHD) broadcasting services. The developed digital video broadcasting system test platform has been installed in commercial broadcasting station, and trial broadcasting service of the system has been performed through the commercial in-service network. For the performance measurement, field test is also executed. To evaluate the practical performance of the implemented system, a commercial broadcasting set-top box is used. Furthermore, by using measurement receiver, various system performances have been evaluated such as BER, PER, and CNR. Because high efficiency video coding (HEVC) can successfully transmit multimedia contents with a raw data rate of 51.6 Mbps, a multichannel UHD service can be serviced in a single physical 6MHz channel.

## 1. Introduction

Recently various advanced broadcasting technologies have been investigated and developed [1–4]. In the terrestrial broadcasting system, the transmission standards supporting 4K ultra-high definition (UHD) broadcasting service have been investigated and developed [5, 6]. Besides, for multichannel UHD broadcasting services, an orthogonal frequency division multiplexing- (OFDM-) based digital video broadcasting system was designed [7, 8].

In this paper, an OFDM-based digital broadcasting transmission system was designed and implemented to support multichannel UHD service. First, the threshold of visibility of the designed system is evaluated in both additive white Gaussian noise (AWGN) and fading channel. And the evaluated threshold of visibility (ToV) performance of the designed system is compared to that of the existing digital broadcasting systems [9, 10]. After the ToV performance evaluation, for the implementation, field programmable gate arrays (FPGAs) were used. Furthermore, to evaluate the

performance of the implemented transmission system, field trials were performed through the commercial in-service network [11] in Daejeon, Korea. In the field trials, the distance between the implemented transmitter and the measurement receiver was 27.1 km, and in the middle of the test route, an amplifier station was adopted. To check the smooth operation of the implemented system, a commercial set-top box (STB) was used.

In addition, to evaluate the performance, a spectrum analyzer and real-time transport stream analyzer were considered. The test results showed a smooth operation and superior performance of the implemented OFDM-based digital video broadcasting system transmitter.

The rest of this paper is organized as follows. Section 2 introduces the system model of the implemented system. Section 3 describes the hardware implementation and major system parameters. Section 4 describes the field test conditions. Test results are provided in Section 5. Finally, concluding remarks are given in Section 6.

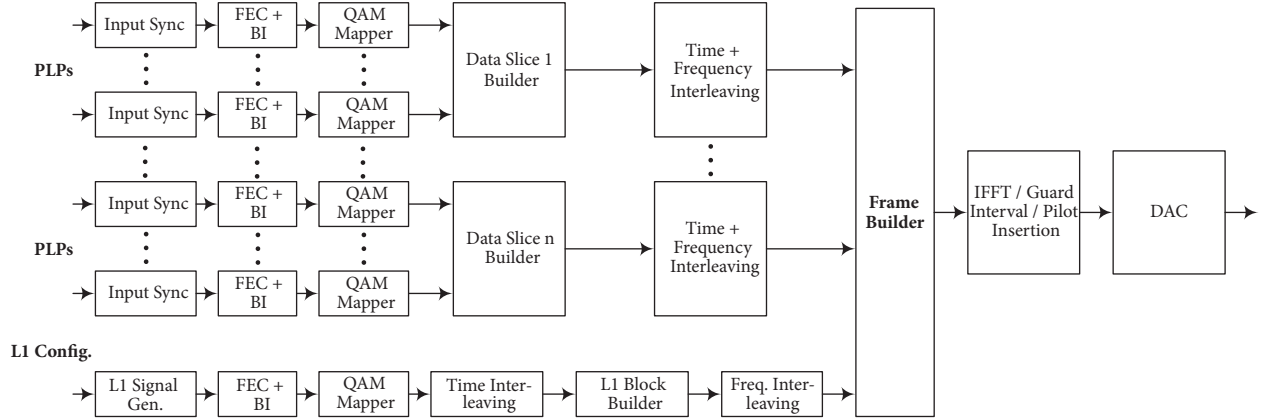


FIGURE 1: OFDM-based digital video broadcasting system transmitter structure.

## 2. Implemented OFDM-Based Digital Video Broadcasting System Model

The implemented OFDM-based digital video broadcasting structure is depicted in Figure 1. As shown in Figure 1, the transmitter is composed of physical layer pipe (PLP) processing, a frame builder, and an OFDM generation block. A PLP is used as an independent logical channel. Each PLP processing block consists of a data input processing block, forward error-correction code (FEC) and bit interleaving block, and QAM mapping block. The FEC is composed of the Bose–Chaudhuri–Hocquenghem (BCH) outer code and low density parity check (LDPC) inner code. Whereas LDPC is a very powerful technique for correcting transmission errors, it produces an error floor condition. BCH can remove the error floor caused by the LDPC decoder of the receiver. FEC encoded bits are then mapped to quadrature amplitude modulation (QAM) symbols and are finally assigned to each subchannel for the OFDM symbol [7, 12].

Next, a data slicer generates one or more slices of data PLP. One data slice or a combination of multiple data slices generates a transmission frame. The transmission frame is transmitted through the inverse fast Fourier transform (IFFT) and digital-analog conversion (DAC) in an OFDM block to produce a radio frequency (RF) signal.

Finally, an L1 signaling block is transmitted into the preamble part of the frames for transmission information. This is related to the position of the data slice, which can be tuned to a data slice to be received at the receiver [7, 12].

A receiver operating within a traditional 6 or 8 MHz TV tuner bandwidth can extract that part of the broad transmission signal that contains the desired service. This part consists of a data slice that never exceeds the traditional bandwidth of a receiver tuner [7, 12, 13].

## 3. Hardware Implementation and Major Parameters of OFDM-Based Digital Broadcasting System

Figure 2 depicts the implemented OFDM-based digital broadcasting system with FEC encoder, modulator, and DAC

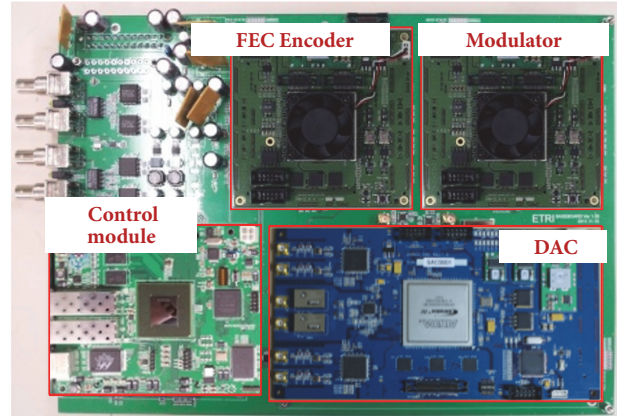


FIGURE 2: Implementation of the OFDM-based digital video broadcasting system transmitter.

TABLE 1: Hardware resources of FEC encoder.

Family		Stratix IV
Device		EP4SE530H40C4
Logic utilization	Combinational ALUTs	7,957 / 424,960 (2%)
	Memory ALUTs	0 / 212,480 (0%)
	Dedicated logic registers	8,061 / 424,960 (2%)
Total registers		8208
Total block memory bits		7,198,555 / 21,233,664 (34%)
DSP block 18-bit elements		0 / 1,024 (0%)
Total PLLs		1 / 12 (8%)

converter. For a convenient implementation, each implemented board uses the same FPGA. In implemented board, operation of the FEC encoder and the modulator is controlled by control PC. The DAC module converts complex digital signal to 44 MHz IF analog signal. RF upconverter is designed independently and converts 44MHz IF signal to wanted RF signal. The control module is designed for the implemented board control. Tables 1–3 show the use of the implemented

TABLE 2: Hardware resources of modulator.

Family		Stratix IV
Device		EP4SE530H40C4
Logic utilization	Combinational ALUTs	944 / 424,960 (< 1%)
	Memory ALUTs	0 / 212,480 (0%)
	Dedicated logic registers	1,049 / 424,960 (< 1%)
Total registers		1136
Total block memory bits		9,309,105 / 21,233,664 (44%)
DSP block 18-bit elements		0 / 1,024 (0%)
Total PLLs		1 / 12 (8%)

TABLE 3: Hardware resources of digital-to-analog converter.

Family		Stratix IV
Device		EP4SE530H40C4
Logic utilization	Combinational ALUTs	24,191 / 424,960 (6%)
	Memory ALUTs	1,748 / 212,480 (< 1%)
	Dedicated logic registers	29,311 / 424,960 (7%)
Total registers		29608
Total block memory bits		11,476,625 / 21,233,664 (54%)
DSP block 18-bit elements		840 / 1,024 (82%)
Total PLLs		1 / 12 (8%)

TABLE 4: Implemented OFDM-based digital broadcasting system parameters.

Parameters	Value
RF frequency	<b>225MHz</b>
(Start frequency)	<b>(132.696)</b>
FFT size	4096
Number of OFDM carriers	3408
Bandwidth	6 MHz
Guard interval (GI)	1/64, 1/128
Modulation order	16QAM - 4096 QAM
Code rate (LDPC)	2/3, 3/4, 4/5, 5/6, 9/10
LI time interleaver (TI) depth	8 OFDM symbols
Data slice TI depth	8 OFDM symbols
Video encoding	HEVC

transmitter. For a convenient implementation, we implement the board using the same FPGA. Table 4 shows the major system parameters of the implemented digital broadcasting system for 6MHz bandwidth [7, 14].

Among the parameters of Table 4, to achieve multichannel UHD broadcasting services with 51.6Mbps, 1/64 guard interval (GI), 4096 QAM, and 9/10 coderate are selected for our field trial.

The system configuration and equipment setup are shown in Figure 3. At the transmitting side, an MPEG-2 TS generator is used for generating the HEVC stream and is interfaced

through DVB-ASI. In the broadcasting network, both optical fiber and coaxial network are used. Optical fiber is used from transmission station to entrance of the reception building, and the coaxial network is used for the in-building broadcasting cable. The broadcasting network is utilized by a multisystem operator (MSO) in Korea.

At the receiving end, the STB receives the downstream signals and interfaces with an UHD display, a monitoring PC, and a stream analyzer. The STB consists of a tuner, demodulator, and HEVC decoder. The tuner can support digital reception for digital TV standards.

#### 4. Field Test Condition

To evaluate the performance of the implemented OFDM-based digital video broadcasting system transmitter, field trials are performed in a commercial in-service network environment. Figure 4 shows the field test bed for the implemented OFDM-based digital video broadcasting system. In the implemented system, a board-type FEC encoder and modulator are developed, which are controlled by a PC. The RF up-converter translates the IF frequency signal of 44 MHz into the desired RF channel. In this test, 225MHz is considered as RF center frequency.

The route used for the field trials is described in Figure 4. The head-end is located at Seonhwa-dong, Jung-Gu, Daejeon, Korea. From this head-end, the downstream signals were transmitted to a laboratory in ETRI through Yuseong station which acts as an amplifier for boosting the signals. Figure 5 shows the configuration of the broadcasting network. The broadcasting network is connected to a head-end through fiber optics and the laboratory is approximately 27.1 km away from Seonhwa station. An Optical Network Unit (ONU) converts the optical signals into RF signals for the final distribution through a coax network. The network configuration of the field trial is depicted in Figure 6.

#### 5. Performance Evaluation

*5.1. ToV Performance Evaluation and Comparison.* To check the ToV of the designed system, BER performance is evaluated in both AWGN and fading channel environments. Furthermore, the evaluated performance of the designed system is compared to that of the existing digital broadcasting system.

Table 5 shows the system parameter comparison between the existing transmission schemes [9, 10] and the implemented transmission scheme. The existing transmission method currently being used is based on a single carrier and can transmit a maximum of 38.8Mbps, while the implemented transmission method is based on a multicarrier and transmits a maximum above 51Mbps to provide a transmission rate that is improved by about 30%. In the case of [9], 1024-QAM-based system has been designed and implemented for UHD cable TV. Furthermore, the data rate of the system of [9] is similar to that of the implemented system with 1024QAM. Therefore, in this subsection, the ToV performance between the designed scheme of [9] and the implemented system of this paper is compared.

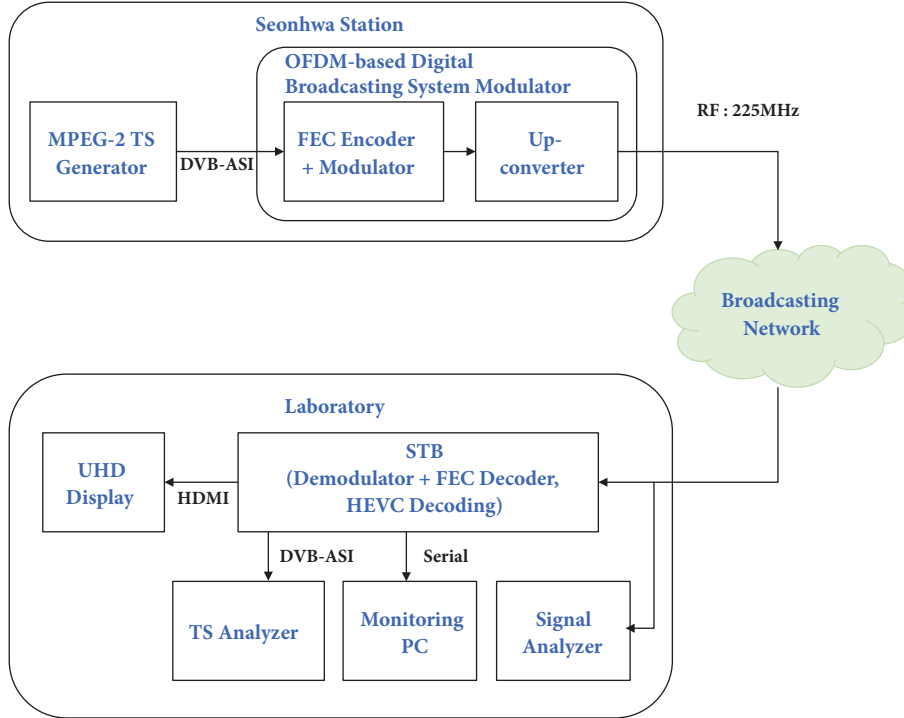


FIGURE 3: System configuration and equipment setup.

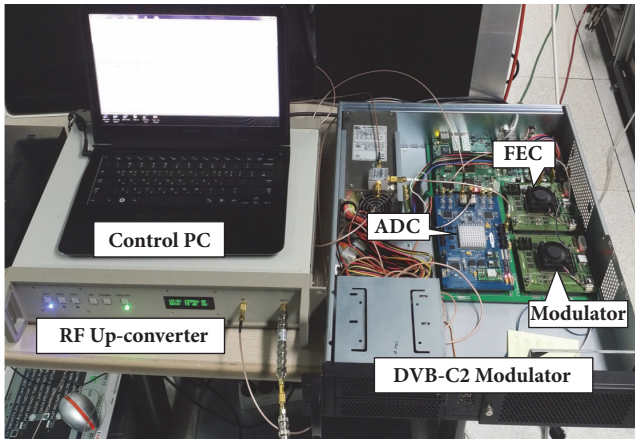


FIGURE 4: Implemented OFDM-based digital video broadcasting system modulator.

Figure 7 shows the BER performance of the designed digital video broadcasting system according to the modulation and coderate in AWGN channel. In the case of 1024QAM with 9/10 coderate, the transmission rate is 48.84Mbps and the ToV is about 29.35dB. Since the ToV of the system in [9] is 32.7dB, the performance of the designed system is about 3dB better than that of the system of [9] in the similar transmission condition. And the ToV of the 4096QAM with 9/10 coderate is about 35dB. Therefore, in the case of the designed system with 4096QAM and 9/10 coderate, if the

TABLE 5: Comparison between existing and implemented system.

	Existing	Designed [9]	Implemented
Standard	ITU-T J.83-B	ITU-T J.83-B	OFDM-based DVB
Transmission	Single Carrier	Single Carrier	Multi-Carrier
Bandwidth	6 MHz	6 MHz	6 MHz
Modulation	256QAM	1024QAM	1024QAM 4096QAM
Post-FEC Data Rate (Mbps)	38.80	48.54	48.84 51.82

SNR of the transmission channel is higher than that of 35dB, the multichannel UHD service can be successfully served.

Figure 8 describes the BER performance in echo channel 1 of Table 6 [15]. In this fading channel, the ToVs of 4096QAM with 9/10 coderate and 1024QAM with 9/10 coderate are about 36.3dB and 30.7dB, respectively. The ToV performance of fading channel is about 1.5dB worse than that of AWGN channel, and because this fading channel model properly reflects the practical broadcasting network environment, higher SNR should be guaranteed than 36.3dB to serve multichannel UHD contents with 4096QAM in in-service broadcasting network.

*5.2. Field Trial Results and Discussions.* As mentioned before, for accomplishment of a stream bitrate of 51.6 Mbps, the

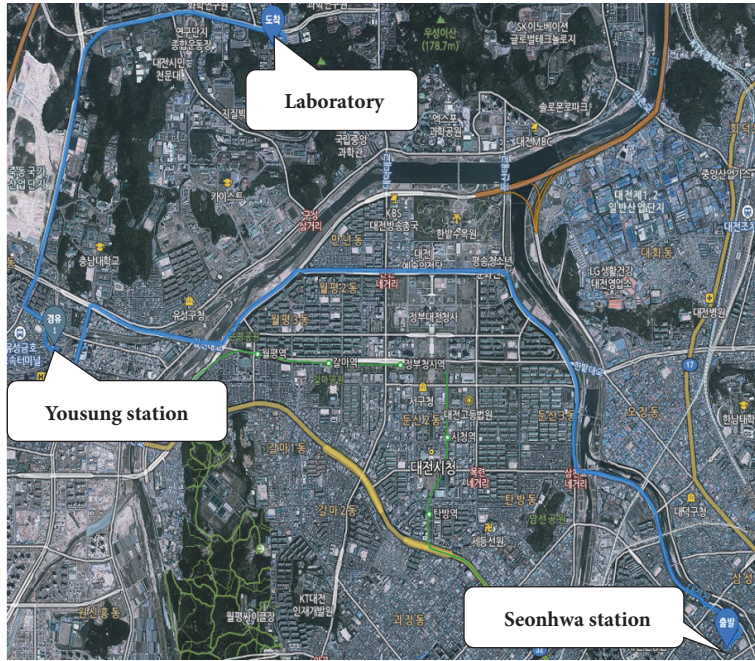


FIGURE 5: The route used for field trials (Seonhwa station: transmission station, Yousung station: amplification station).

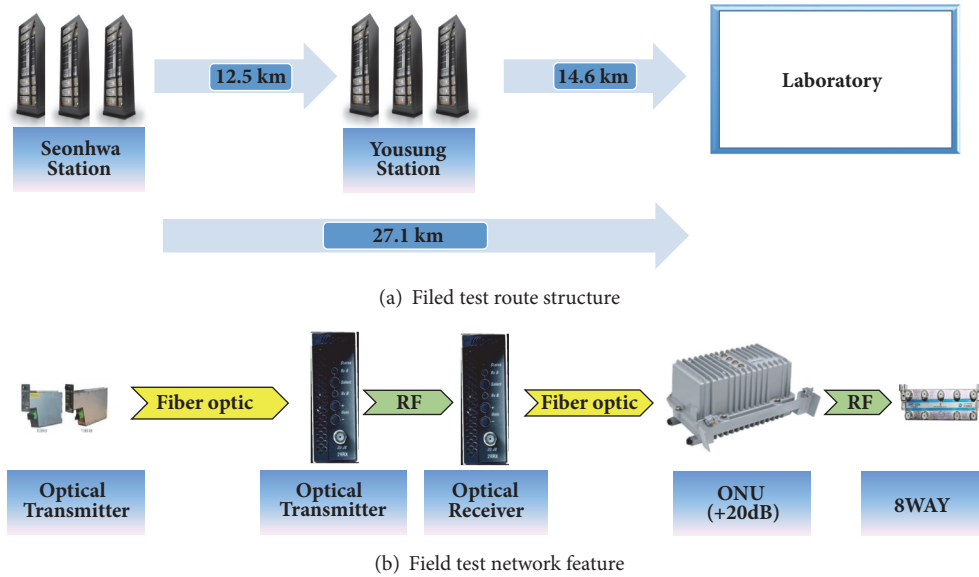


FIGURE 6: Broadcasting network configuration.

4096 QAM and 9/10 LDPC code rate are considered. In our paper, the achieved stream bitrate of 51.6Mbps means data transmission rate without header and pilot symbols. Figure 9 shows the frequency response of the received broadcasting signal. The spectrum result describes that the center frequency is 225 MHz, and the measured input power of the analog-to-digital converter (ADC) is -27.48 dBm within 6 MHz channel bandwidth. Figure 10 shows the constellation of the received signal after equalization process. The data for the

constellation was dumped and depicted in a monitoring PC connected to the receiver. As in the figure, the constellation of the equalized received signal shows clear QAM points.

The received signaling information is checked by commercial received signal analyzer in Figure 3. This commercial signal analyzer displays L1 signaling part 2 data and the FEC frame header as described in Figure 11. All parameters are the same as shown in Table 4. This means that the implemented FEC encoder and modulator work properly.

TABLE 6: Channel profile of echo channel 1.

Power [dB]	Delay [ns]	Phase [rad]
-11	38	0.95
-14	181	1.67
-17	427	0.26
-23	809	1.20
-32	1633	1.12
-40	3708	0.81

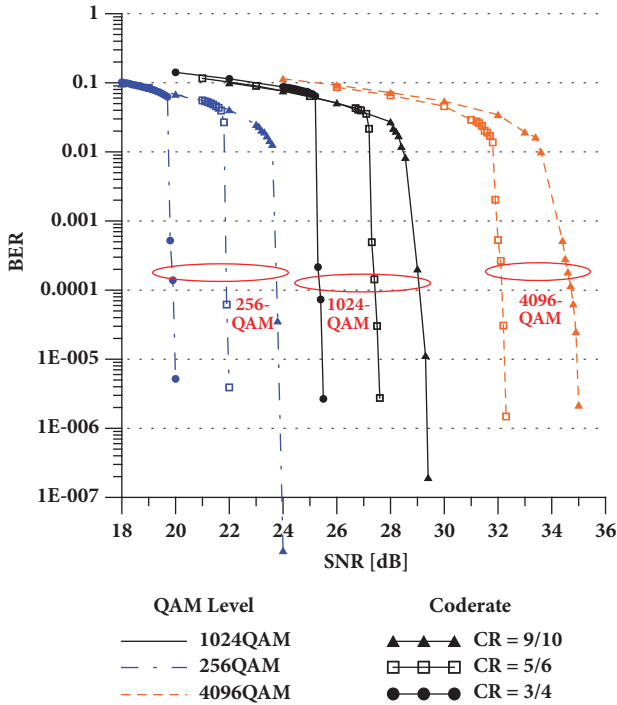


FIGURE 7: BER performance of designed digital video broadcasting system in AWGN channel.

The results of the field trials were used mainly to evaluate two aspects: the reception performance and the seamless stream reception status. To measure the reception performance, commercial STB is modified. From the modified STB, serial interface output data is gathered by monitoring PC. Figure 12 shows the measured carrier-to-noise ratio (C/N) and BER after the BCH decoder in a commercial STB. The value of the measured C/N is 40.25 dB. This value is superior to the required ToV (36.3 dB) as shown in Figure 8. That is, analog parts such as RF upconverter and a digital logic block were properly developed. In addition, the measured BER was zero because of the superior C/N at the receiver. The receiver system configuration is shown in Figure 13. As expected, the video stream is clearly played on UHDTV. Moreover, a seamless playback is achieved.

Furthermore to check the accomplishment of 51.6 Mbps stream bitrate, the bitrate of received signal is monitored by TS analyzer of Figure 3. Figure 14 describes the results of TS

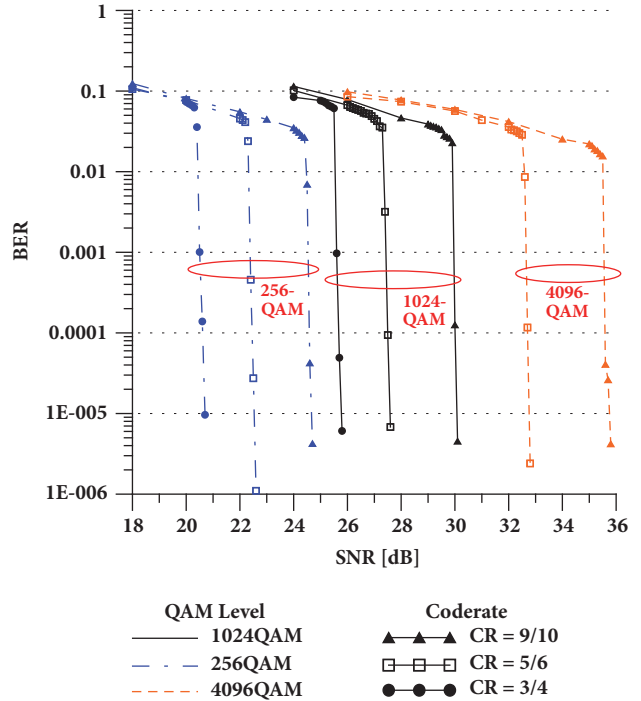


FIGURE 8: BER performance of designed digital video broadcasting system in fading channel (echo channel 1).

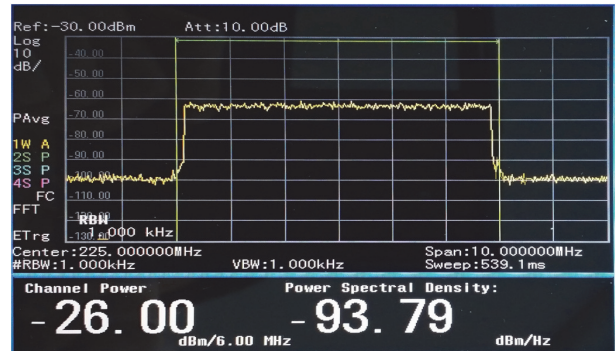


FIGURE 9: Received DVB-C2 signal in the frequency domain.

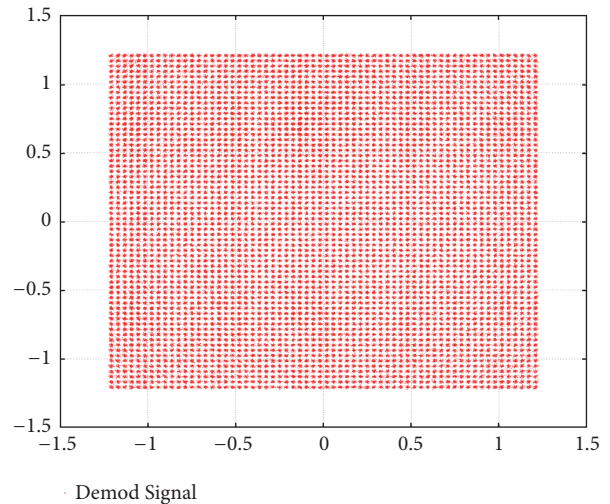


FIGURE 10: 4096-QAM Constellation for the Received DVB-C2 signal.



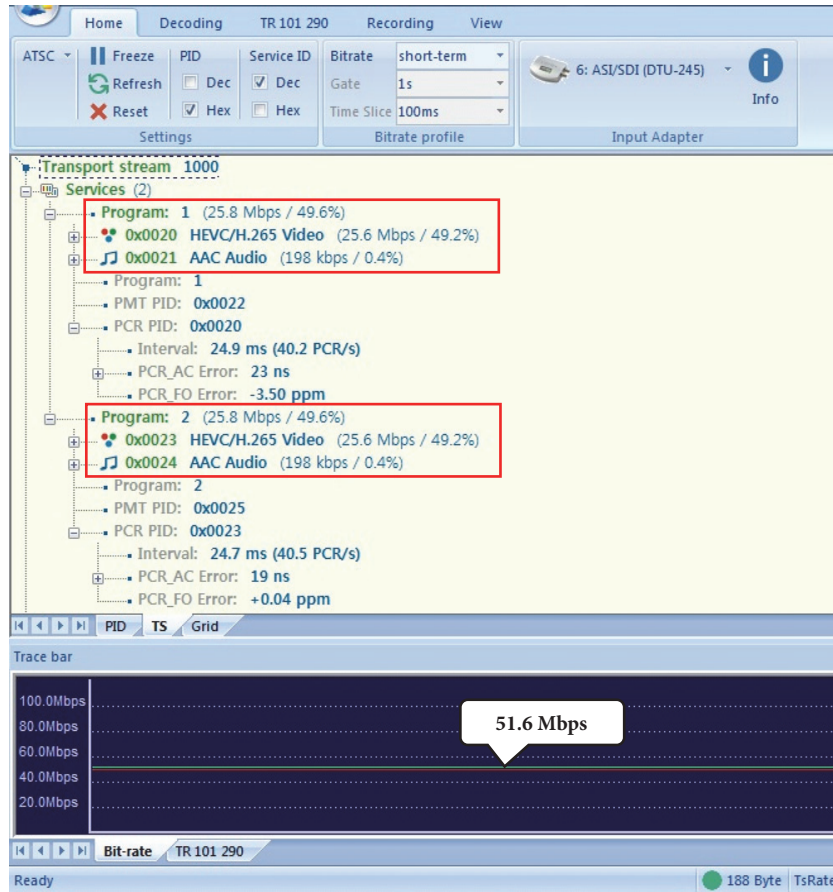


FIGURE 14: Received stream bitrate described in TS analyzer.

to the performance and physical network status. These test results can provide basic information for OFDM-based digital video broadcasting technology in many countries and may lead to the development of a next-generation digital broadcasting system.

### Data Availability

The data used to support the findings of this study are available from the corresponding author upon request.

### Conflicts of Interest

The authors declare that they have no conflicts of interest.

### Acknowledgments

This work was supported by the Institute for Information & communications Technology Promotion (IITP) grants funded by the Korean government (MSIP) No. 2016-0-00106, Development of the RF-Signal over IP Technology for the Smart Media Services Based on Optical IP Network.

### References

- [1] K. Park, N. Kim, and B.-D. Lee, "Performance evaluation of the media-transport technologies for the next-generation digital broadcasting systems," *IEEE ACCESS*, vol. 5, pp. 4125–4131, 2017.
- [2] T. T. Adeliyi and O. O. Olugbara, "Fast Channel Navigation of Internet Protocol Television Using Adaptive Hybrid Delivery Method," *Journal of Computer Networks and Communications*, vol. 2018, Article ID 2721950, 11 pages, 2018.
- [3] J. Seok, Y. Kim, M. Ki, H. Y. Kim, and J. S. Choi, "Fast prediction mode decision in HEVC Using a pseudo rate-distortion based on separated encoding structure," *ETRI Journal*, vol. 38, no. 5, pp. 807–817, 2016.
- [4] B. Kwon and S. Lee, "Effective Interference Nulling Virtual MIMO Broadcasting Transceiver for Multiple Relaying," *IEEE Access*, vol. 5, pp. 20695–20706, 2017.
- [5] Digital Video Broadcasting (DVB); frame structure channel coding and modulation for a second generation digital terrestrial television broadcasting system (DVB-T2), ETSI EN 302 755 V1.3.1, Apr. 2012.
- [6] ATSC: *ATSC Physical Layer Protocol Standard*, document A/322, Adv. Television Syst. Committee, Washington, DC, USA, Sep. 2016.
- [7] ETSI EN 302 769 v1.2.1, Digital Video Broadcasting(DVB) ; Frame structure channel coding and modulation for a second



- generation digital transmission system for cable systems (DVB-C2), Apr. 2011.
- [8] . Jae-Ho Lee, . Dong-Joon Choi, . Namho Hur, and . Whan-Woo Kim, "Performance Analysis of a Proposed Pre-FEC Structure for a DVB-C2 Receiver," *IEEE Transactions on Broadcasting*, vol. 59, no. 4, pp. 638–647, 2013.
  - [9] S.-H. Kim, J. Choi, J. Kim, M. S. Hossen, and K.-D. Kim, "Design and implementation of the 1024-QAM RF transmission system for UHD cable TV broadcasting," in *Proceedings of the 16th International Conference on Advanced Communication Technology: Content Centric Network Innovation!, ICACT 2014*, pp. 1317–1324, Republic of Korea, February 2014.
  - [10] P. K. Sinha, P. Biswas, and A. Sinha, "Design and implementation of high speed digital multi-programme system based on ITU-T J.83 annexures A and C," in *Proceedings of the 2015 IEEE International Conference on Signal Processing, Informatics, Communication and Energy Systems, SPICES 2015*, India, February 2015.
  - [11] W. Xiang, G. Wu, Q. Ling, and L. Wang, "Piecewise patching for time-shifted TV over HFC networks," *IEEE Transactions on Consumer Electronics*, vol. 53, no. 3, pp. 891–897, 2007.
  - [12] S. Ra, J. Song, J. Bae et al., "Performance measurement of high-efficient OFDM based transmission system in commercial HFC network," in *Proceedings of the 2016 IEEE International Symposium on Broadband Multimedia Systems and Broadcasting (BMSB)*, pp. 1-2, Nara, Japan, June 2016.
  - [13] T. Kamata, K. Okui, M. Fukasawa, T. Matsuoka, and K. Taniguchi, "Low-power zero-IF full-segment ISDB-T CMOS tuner with tenth-order baseband filters," *IEEE Transactions on Consumer Electronics*, vol. 57, no. 2, pp. 403–410, 2011.
  - [14] J. Lee, W. You, J. Oh, S. Ra, and J. Jung, "Performance analysis and implementation of a DVB-C2 transceiver," in *Proceedings of the 18th International Conference on Advanced Communications Technology, ICACT 2016*, pp. 612–616, Republic of Korea, February 2016.
  - [15] DVB Document A147, Digital Video Broadcasting (DVB), Implementation Guidelines for a second generation digital cable transmission system (DVB-C2), March 2013.

## Research Article

# Robust Shrinkage Range Estimation Algorithms Based on Hampel and Skipped Filters

Chee-Hyun Park <sup>1</sup> and Joon-Hyuk Chang <sup>2</sup>

<sup>1</sup>Department of Electronics and Computer Engineering, Hanyang University, Seoul 133-791, Republic of Korea

<sup>2</sup>Department of Electronic Engineering, Hanyang University, Seoul 133-791, Republic of Korea

Correspondence should be addressed to Joon-Hyuk Chang; [jchang@hanyang.ac.kr](mailto:jchang@hanyang.ac.kr)

Received 28 September 2018; Accepted 18 December 2018; Published 1 January 2019

Guest Editor: Seok-Chul Kwon

Copyright © 2019 Chee-Hyun Park and Joon-Hyuk Chang. This is an open access article distributed under the Creative Commons Attribution License, which permits unrestricted use, distribution, and reproduction in any medium, provided the original work is properly cited.

Herein, we present robust shrinkage range estimation algorithms for which received signal strength measurements are used to estimate the distance between emitter and sensor. The concepts of robustness for the Hampel filter and skipped filter are combined with shrinkage for the positive blind minimax and Bayes shrinkage estimation. It is demonstrated that the estimation accuracies of the proposed methods are higher than those of the existing median-based shrinkage methods through extensive simulations.

## 1. Introduction

Range estimation is a crucial technique in which the distance between the emitter and sensor is estimated utilizing time-of-arrival (TOA) or received signal strength (RSS) measurements. Distance information is important for range-based source localization utilizing TOA and RSS measurements because distance is used for source localization. Namely, the more accurate is the distance measurement; the better is the localization accuracy. Range estimation problems under line-of-sight (LOS) environments have been studied in previous works [1–5]. In [1], the ad hoc closed-form hybrid TOA/RSS range estimation algorithm is developed. The ad hoc closed-form range estimator is superior to the iterative maximum likelihood (ML) method in a certain parameter space. Also, a fusion algorithm is studied for range-based tracking using two independent processing chains for RSS and TOA [2]. In addition, the Cramér-Rao lower bound (CRLB) for the TOA/RSS-based range estimation is derived in [3]. The RSS-based ranging is famous for its low cost; thus it is more popular than the TOA-based ranging algorithm. In [4], the best unbiased and linear minimum mean square range estimates are studied in the context of RSS-based range estimation. Also, a range estimation method based on the multiplicative distance-correction factor (MDCF) is developed to attenuate

the inaccuracy for the estimated range, where grid based optimization and particle swarm optimization are employed [5].

The shrinkage estimation approach has received attention because it outperforms the ML and least squares (LS) in conditions of small samples or low signal-to-noise ratio (SNR). Although the shrinkage algorithms based on mathematical optimization methods are superior to the blind minimax estimation, we adopt the positive blind minimax (PBM) algorithm in this paper because its computational complexity is much simpler than that of the mathematical optimization-based methods [6, 7]. Also, the Bayes shrinkage (BS) estimation is utilized because PBM and BS estimators are known to outperform the conventional shrinkage estimator [7, 8].

However, some open problems exist and a crucial task among range estimation problems is to determine the distance between the emitter and sensor in LOS/non-line-of-sight (NLOS) mixed situations. For example, the LOS path between the source and sensors may be obstructed under indoor scenarios. Motivated by the above problems, we propose the algorithm combining the shrinkage and robustness. To make the shrinkage estimator robust to outliers, we adopt the Hampel [9–11] and skipped filters [9]. We summarize our main contributions as follows:

- (i) The variance of the range estimate based on the Hampel filter is found algebraically.
- (ii) The variance of the range estimate based on the skipped filter is calculated in the analytical form.
- (iii) We develop the closed-form robust shrinkage range estimation methods based on the Hampel filter/PBM and Hampel filter/BS estimator.
- (iv) We propose the closed-form robust shrinkage range estimation methods based on the skipped filter/PBM and skipped filter/BS method.

The algorithms that use the Tyler's estimator for the robust shrinkage estimation of the covariance matrix have been studied [12–15]. But, to the best of our knowledge, the robust shrinkage approaches combined with the Hampel and skipped filters have not been investigated in the existing literatures. Also, note that the proposed methods are the closed-form algorithms. Thus, the complexities of the proposed algorithms are lower than those of the mathematical optimization or iteration-based algorithms.

This paper is organized as follows. Section 2 deals with the LOS/NLOS mixed range estimation problem. Section 3 addresses the existing range estimation methods in detail. Section 4 describes the proposed robust shrinkage distance estimation algorithms based on the Hampel filter, skipped filter, PBM, and BS methods. Section 5 evaluates the mean square error (MSE) performances through simulation results. Section 6 presents the conclusion.

## 2. Problem Formulation

The aim of the range estimation method using RSS measurements is to accurately predict the distance between the emitter and sensor so that the error criterion, e.g., the MSE or squared error, is minimized. In the context of LOS/NLOS mixed range estimation, the RSS measurement equation is determined as [16]

$$P_i = P_o - 10\gamma \log_{10} \frac{d_o}{d} + n_i, \quad i = 1, 2, \dots, M \quad (1)$$

where  $P_i$  is the  $i$ th RSS for the sensor in decibel (dB),  $P_o$  is the signal strength at the reference distance ( $d_o$ ),  $d_o$  is set to 1m for convenience,  $d$  is the true range (distance) to be estimated,  $\gamma$  is the path loss exponent,  $n_i$  is distributed by  $(1 - \epsilon)N(0, \sigma_1^2) + \epsilon N(\mu_2, \sigma_2^2)$  with  $M$  denoting samples in the sensor, and  $N(\mu, \sigma^2)$  is the Gaussian probability density function (PDF) with mean  $\mu$  and variance  $\sigma^2$ , respectively [17]. It is assumed that  $\gamma$  and  $P_o$  are known *a priori* from the calibration campaign [18, 19]. The measurement error  $n_i$  is the random process that follows a Gaussian distribution with  $N(0, \sigma^2)$  in conventional LOS situations. However, the noise distribution rarely follows the conventional Gaussian distribution due to multipath effects in indoor and urban regions. Therefore, the noise distribution should be designed as a two-mode Gaussian mixture distribution in which the LOS noise component is distributed as  $N(0, \sigma_1^2)$  and the NLOS noise follows  $N(\mu_2, \sigma_2^2)$ . The LOS noise has a probability of  $1 - \epsilon$  and

the NLOS noise has a probability of  $\epsilon$ . Like previous research for the LOS/NLOS mixture localization, while the statistics of the inlier can be obtained, the mean and variance of the outlier distribution are unavailable. Here,  $\epsilon$  ( $0 \leq \epsilon \leq 1$ ) is a measure of contamination, which is usually lower than 0.1 [20–22].

## 3. Review of Conventional Robust Shrinkage Approaches

*3.1. ML-Based Shrinkage Range Estimation Algorithm.* In the LOS situations, the shrinkage estimator is obtained by multiplying the ML estimator ( $\hat{d}^{\text{ML}} = d_o 10^{(\bar{P}-P_o)/10\gamma} = d \cdot 10^{\bar{n}}$ ) and shrinkage factor ( $c$ ) [4, 23], where  $\bar{P} = (\sum_{i=1}^M P_i)/M$ ,  $\bar{n} = (\sum_{i=1}^M n_i)/M$ . The MSE for the shrinkage range estimation is represented as follows:

$$\begin{aligned} \text{MSE} &= E \left[ (c \cdot \hat{d}^{\text{ML}} - d)^T (c \cdot \hat{d}^{\text{ML}} - d) \right] \\ &= E \left[ (c(d + v) - d)^T (c(d + v) - d) \right] \\ &= (c - 1)^2 d^2 + c^2 E[v^2] + 2c(c - 1) d E[v] \quad (2) \\ &\approx (c - 1)^2 d^2 + c^2 E[v^2] \\ &\approx (c - 1)^2 d^2 + c^2 \text{var}(\hat{d}^{\text{ML}}) \end{aligned}$$

where  $v$  is the error of the ML estimate ( $\hat{d}^{\text{ML}}$ ) and  $E[v] \approx 0$  by means of the delta method [24]. Then, the shrinkage factor for distance estimation is derived by minimizing the MSE as follows:

$$c = \frac{d^2}{d^2 + \text{var}(\hat{d}^{\text{ML}})} \approx \frac{(\hat{d}^{\text{ML}})^2}{(\hat{d}^{\text{ML}})^2 + \text{var}(\hat{d}^{\text{ML}})}. \quad (3)$$

The shrinkage range estimator is obtained as follows:

$$b = \frac{(\hat{d}^{\text{ML}})^2}{(\hat{d}^{\text{ML}})^2 + \text{var}(\hat{d}^{\text{ML}})} \cdot \hat{d}^{\text{ML}}. \quad (4)$$

Although  $\text{var}(\hat{d}^{\text{ML}})$  can be calculated analytically,  $\hat{d}^{\text{ML}}$  is linearized to apply the shrinkage algorithm (see (2)). For this, the ML range estimator is linearized for  $E[\bar{n}]$  using the Taylor-series as follows:

$$\begin{aligned} \hat{d}^{\text{ML}} &\approx d \cdot \left\{ 10^{E[\bar{n}]/10\gamma} + 10^{E[\bar{n}]/10\gamma} \frac{\ln 10}{10\gamma} (\bar{n} - E[\bar{n}]) \right\} \\ &= d + \left( \frac{\ln 10}{10\gamma} \right) d \cdot \bar{n}. \end{aligned} \quad (5)$$

Then,  $\text{var}\{\hat{d}^{\text{ML}}\} \approx d^2 ((\ln 10)/10\gamma)^2 \text{var}\{\bar{P}\}$ . Because  $d$  is an unknown true value to be estimated, the variance of  $\hat{d}^{\text{ML}}$  can be approximated as  $\{\hat{d}^{\text{ML}}\}^2 ((\ln 10)/10\gamma)^2 (\sigma^2/M)$ , where  $\sigma^2$  is the variance per sample. It should be noticed that the approximated variance of  $\hat{d}^{\text{ML}}$  is different from the true

variance of  $\hat{d}^{\text{ML}}$  as can be seen from our simulation results. Furthermore, the conventional shrinkage estimator can be improved in two ways: the PBM algorithm and BS method. Finally, the PBM estimator is represented as follows [7]:

$$b_{\text{PBM}} = \alpha_{\text{PBM}} \cdot \hat{d}^{\text{ML}} + (1 - \alpha_{\text{PBM}}) d^* \quad (6)$$

where  $\alpha_{\text{PBM}} = [(\hat{d}^{\text{ML}})^2 - \text{var}(\hat{d}^{\text{ML}})]_+ / [(\hat{d}^{\text{ML}})^2 - \text{var}(\hat{d}^{\text{ML}})]_+ + \text{var}(\hat{d}^{\text{ML}})$ ,  $d^*$  is the prior point guess value to be determined empirically, and  $(\cdot)_+$  denotes the  $\max(0, \cdot)$ . Also, the BS estimator is obtained in the following [8]:

$$b_{\text{BS}} = \alpha_{\text{BS}} \cdot \hat{d}^{\text{ML}} + (1 - \alpha_{\text{BS}}) d^* \quad (7)$$

where  $\alpha_{\text{BS}} = (\hat{d}^{\text{ML}} - d^*)^2 / ((\hat{d}^{\text{ML}} - d^*)^2 + \text{var}(\hat{d}^{\text{ML}}))$ . When the prior value,  $d^*$ , is properly selected, the MSE performance of the BS method is superior to that of the existing shrinkage algorithm.

**3.2. Median- (Med-) Based Robust Shrinkage Range Estimation Algorithm.** The ML-based range estimator is an optimal estimator in LOS environments; however it becomes much inaccurate when there are outliers among samples. To circumvent this problem, the median-based range estimator can be utilized because it is insensitive to outliers when the contamination ratio is less than 50%. In this case, the median-based range estimator can be represented as  $\hat{d}^{\text{Med}} = d_o 10^{(\bar{P} - P_o)/10\gamma}$ , where  $\bar{P} = \text{median}\{P_1, \dots, P_M\}$ . Then, in the same manner as the ML-based range estimator, the variance of the median-based robust range algorithm ( $\text{var}[\hat{d}^{\text{Med}}]$ ) can be obtained as  $d^2 ((\ln 10)/10\gamma)^2 \text{var}\{\bar{P}\} \approx \{\hat{d}^{\text{Med}}\}^2 ((\ln 10)/10\gamma)^2 (\sigma^2/M)(\pi/2)$ . Note that, in the derivation of variance of the median-based robust range estimation method, the constant  $\pi/2$  is multiplied because the variance of the sample median is asymptotically  $\pi/2$  times larger than that of the sample mean in the LOS situation [25]. Also, the median-based shrinkage range estimator can be categorized into the median-based PBM (Med/PBM) and median-based Bayesian shrinkage (Med/BS) estimator. The Med/PBM and Med/BS estimators are represented as follows:

$$\begin{aligned} b_{\text{Med/PBM}} &= \alpha_{\text{Med/PBM}} \cdot \hat{d}^{\text{Med}} + (1 - \alpha_{\text{Med/PBM}}) d^* \\ b_{\text{Med/BS}} &= \alpha_{\text{Med/BS}} \cdot \hat{d}^{\text{Med}} + (1 - \alpha_{\text{Med/BS}}) d^* \end{aligned} \quad (8)$$

where  $\alpha_{\text{Med/PBM}} = [(\hat{d}^{\text{Med}})^2 - \text{var}(\hat{d}^{\text{Med}})]_+ / [(\hat{d}^{\text{Med}})^2 - \text{var}(\hat{d}^{\text{Med}})]_+ + \text{var}(\hat{d}^{\text{Med}})$  and  $\alpha_{\text{Med/BS}} = (\hat{d}^{\text{Med}} - d^*)^2 / ((\hat{d}^{\text{Med}} - d^*)^2 + \text{var}(\hat{d}^{\text{Med}}))$ .

**3.3. Hampel Filter.** The version considered, herein, represents a moving-window implementation of the Hampel filter as in [9–11], an outlier detection procedure based on the median and median absolute deviation (MAD) scale estimator. Specifically, this filter's response is given by

$$y_i = \begin{cases} P_i, & |P_i - m| < tD, \\ m, & |P_i - m| > tD \end{cases} \quad (9)$$

where  $m$  is the median value from the moving data window and  $D$  is the MAD scale estimate of the sensor, defined as  $D = 1.4826 \times \text{median}|P_{1:M} - m|$ . Namely, the sensors are categorized into the LOS sensor set and LOS/NLOS mixture sensor set with the use of (9). If the entire elements of the sensor meet the first condition of (9), it is predicted as an LOS sensor. If at least one sample satisfies the second condition of (9), the corresponding sensor is regarded as an LOS/NLOS mixture sensor. The factor 1.4826 allows the MAD scale to produce an unbiased estimate of the standard deviation for Gaussian data. Also,  $P_{1:M}$  is the RSS from the first to the  $M$ th in the sensor and the parameter  $t$  is selected empirically. When  $t = 0$ , the Hampel filter is reduced to the standard median filter. The Hampel filter suffers from implosion, which means more than 50% of data values are identical, i.e.,  $D = 0$ , implying that  $y_i = m$  irrespective of the constant  $t$ .

**3.4. Skipped Filter [9].** In the Hampel filter of the previous section, when the absolute value of the difference between the sample and median is larger than the threshold, the sample median is substituted for the corresponding sample. In contrast, in the skipped filter, when the sample is predicted as an outlier, the corresponding sample is removed from the sample set of the sensor. Because the contamination ratio (the percentage of outliers in the sample set) is usually smaller than 10% [20–22], the probability that the filtered samples are depleted is much small.

## 4. Proposed Robust Shrinkage Range Estimation Method

Below, we explain in detail the proposed Hampel filter-based, skipped filter-based shrinkage range estimation algorithms.

**4.1. Hampel Filter/PBM and Hampel Filter/BS-Based Range Estimation Algorithms.** In this subsection, the Hampel filter-based shrinkage range estimation algorithms are described in detail. The filtered data,  $y_{1:M}$ , are averaged using the sample mean, i.e.,  $P^{h,f} = (\sum_{i=1}^M y_i) / M$ . Then, the variance of the statistic  $P^{h,f}$  is found as follows:

$$\begin{aligned} &\text{var}[P^{h,f}] \\ &= \frac{(\text{var}[\text{one inlier}(y_q)] \times \text{number of inliers} + \text{var}[\text{median for } y_i (i = 1, \dots, M)] \times \text{number of outliers})}{M^2} \\ &= \frac{S/Q \times Q + \pi/2 \times S/Q^2 \times R}{M^2} = \frac{S + \pi/2 \times S/Q^2 \times R}{M^2} \end{aligned} \quad (10)$$

where  $S = \sum_q (y_q - m)^2$ ,  $q$ 's are the sample indices determined as inliers in the LOS/NLOS mixture state, and  $Q$  is the number of samples predicted as inliers with the use of (9). Also,  $R$  is the number of samples determined as outliers and  $M = (Q + R)$  is the total number of samples in the sensor. In the numerator of the second equation of (10), the constant  $\pi/2$  is multiplied by the variance of the sample mean [25] since the variance of the sample median is asymptotically  $\pi/2$  times larger than that of the sample mean in the LOS situation. Furthermore, we do not consider the implosion because it rarely occurs. Then, the variance of the Hampel filter-based range estimator is obtained as  $\text{var}\{\hat{d}^{\text{Ham}}\} \simeq \{\hat{d}^{\text{Ham}}\}^2 ((\ln 10)/10\gamma)^2 \cdot \text{var}[P^{h,f}]$ , where  $\hat{d}^{\text{Ham}} = d_o 10^{(P^{h,f} - P_o)/10\gamma}$ . Additionally, the robust shrinkage range estimator based on the Hampel filter and PBM estimator is obtained as follows:

$$b_{\text{Ham/PBM}} = \alpha_{\text{Ham/PBM}} \cdot \hat{d}^{\text{Ham}} + (1 - \alpha_{\text{Ham/PBM}}) d^* \quad (11)$$

where  $\alpha_{\text{Ham/PBM}} = ((\hat{d}^{\text{Ham}})^2 - \text{var}(\hat{d}^{\text{Ham}}))_+ / (((\hat{d}^{\text{Ham}})^2 - \text{var}(\hat{d}^{\text{Ham}}))_+ + \text{var}(\hat{d}^{\text{Ham}}))$ . Furthermore, the robust shrinkage range estimator based on the Hampel filter and BS method is found as

$$b_{\text{Ham/BS}} = \alpha_{\text{Ham/BS}} \cdot \hat{d}^{\text{Ham}} + (1 - \alpha_{\text{Ham/BS}}) d^* \quad (12)$$

where  $\alpha_{\text{Ham/BS}} = (\hat{d}^{\text{Ham}} - d^*)^2 / ((\hat{d}^{\text{Ham}} - d^*)^2 + \text{var}(\hat{d}^{\text{Ham}}))$ .

**4.2. Skipped Filter/PBM and Skipped Filter/BS-Based Range Estimation Methods.** In the same manner as the Hampel filter-based shrinkage range estimation method, the filtered data,  $y_q$ , are averaged using the sample mean, i.e.,  $P^{s,f} = \sum_q (y_q/Q)$ . The variance of the statistic  $P^{s,f}$  is calculated in the following:

$$\begin{aligned} \text{var}[P^{s,f}] &= \frac{\text{var}[\text{one inlier}(y_q)] \times \text{number of inliers}}{Q^2} \quad (13) \\ &= \frac{S/Q \times Q}{Q^2} = \frac{S}{Q^2}. \end{aligned}$$

Then, the variance of the skipped filter-based range estimator is obtained as  $\text{var}\{\hat{d}^{\text{Sk}}\} \simeq \{\hat{d}^{\text{Sk}}\}^2 ((\ln 10)/10\gamma)^2 \cdot \text{var}[P^{s,f}]$ , where  $\hat{d}^{\text{Sk}} = d_o 10^{(P^{s,f} - P_o)/10\gamma}$ . Additionally, the robust shrinkage range estimator based on the skipped filter and PBM method is obtained as follows:

$$b_{\text{Sk/PBM}} = \alpha_{\text{Sk/PBM}} \cdot \hat{d}^{\text{Sk}} + (1 - \alpha_{\text{Sk/PBM}}) d^* \quad (14)$$

where  $\alpha_{\text{Sk/PBM}} = ((\hat{d}^{\text{Sk}})^2 - \text{var}(\hat{d}^{\text{Sk}}))_+ / (((\hat{d}^{\text{Sk}})^2 - \text{var}(\hat{d}^{\text{Sk}}))_+ + \text{var}(\hat{d}^{\text{Sk}}))$ . Indeed, the robust shrinkage range estimator based on the skipped filter and BS method is obtained as follows:

$$b_{\text{Sk/BS}} = \alpha_{\text{Sk/BS}} \cdot \hat{d}^{\text{Sk}} + (1 - \alpha_{\text{Sk/BS}}) d^* \quad (15)$$

where  $\alpha_{\text{Sk/BS}} = (\hat{d}^{\text{Sk}} - d^*)^2 / ((\hat{d}^{\text{Sk}} - d^*)^2 + \text{var}(\hat{d}^{\text{Sk}}))$ .

TABLE 1: Simulation settings.

Distance (d)	5 m
Parameter ( $d^*$ )	10
Parameter (t)	1.5
Number of Monte-Carlo simulation	1000
Number of sensors	1
Path loss exponent ( $\gamma$ )	3
$P_o$	5 dB
$d_o$	1 m
Directivity of source	omnidirection

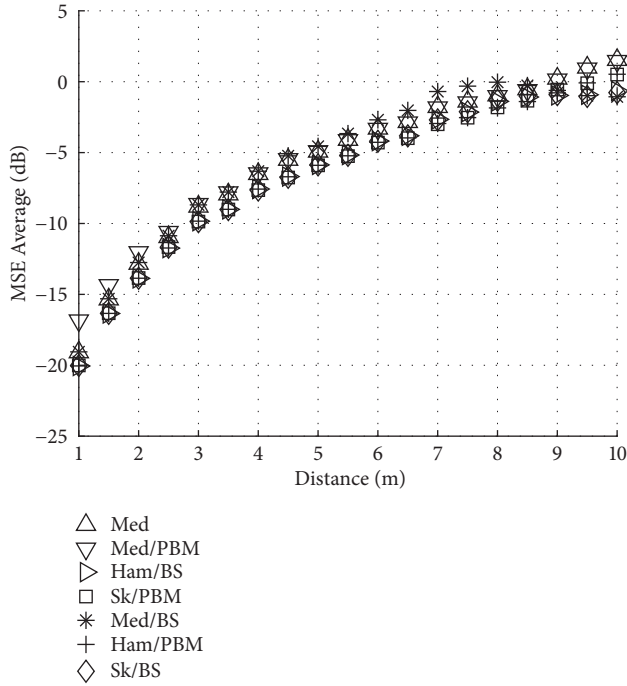
TABLE 2: List of abbreviations.

TOA	Time of Arrival
RSS	Received Signal Strength
LOS	Line of sight
ML	Maximum Likelihood
CRLB	Cramér-Rao lower bound
MDCF	multiplicative distance-correction factor
LS	Least Squares
SNR	Signal-to-noise ratio
PBM	positive blind minimax
BS	Bayes shrinkage
NLOS	Non-line-of-sight
dB	decibel
PDF	Probability density function
MSE	Mean square error
Med/PBM	Median/Positive blind minimax
Ham/BS	Hampel filter/Bayes shrinkage
SK/PBM	Skipped filter/Positive blind minimax

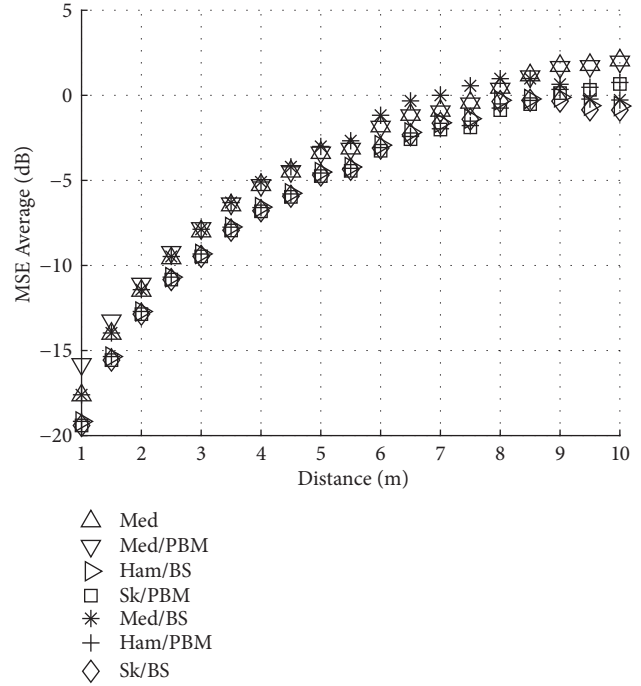
Furthermore, the distance can be also estimated in the energy-based acoustic ranging problem [26, 27]. Unlike the RSS-based ranging algorithm, the reference signal power is not known in the energy-based ranging method. Therefore, the distance cannot be estimated directly from the measurement equation. In this case, the range can be estimated sequentially, i.e., the source location is firstly estimated using the energy minimization-based localization algorithm [27] (the robust version of the measurement is used in the localization algorithm), then the distance is obtained from the estimated position. The shrinkage factor can be found using the estimated source coordinates and delta method. The difference between the shrinkage factor in the LOS situation and that of LOS/NLOS mixture environment lies in that the position estimate using the robust algorithm is utilized under the LOS/NLOS mixed situation. The details for the algorithm and performance evaluation remain as future works.

## 5. Simulation Results

We compare the performance of the proposed LOS/NLOS mixed range estimation methods with that of the median-based shrinkage range estimator in this section. The simulation setting is provided in Table 1. Table 2 explains the



(a) Contamination ratio ( $\epsilon$ ): 20%, the bias of NLOS noise ( $\mu_2$ ): 4 m, standard deviation of LOS noise ( $\sigma_1$ ):  $\sqrt{10}$  m, and standard deviation of NLOS noise ( $\sigma_2$ ): 100 m



(b)  $\epsilon$ : 30%,  $\sigma_1$ :  $\sqrt{10}$  m,  $\mu_2$ : 4 m, and  $\sigma_2$ : 100 m

FIGURE 1: MSE averages of the range estimation algorithms as a function of the distance.

abbreviations used in this paper. The MSE average is defined as follows:

$$\text{MSE average} = \frac{\sum_{k=1}^{1000} (\hat{d}(k) - d)^2}{1000} \quad (16)$$

where  $\hat{d}(k)$  is the estimated range from the point target to the sensor in the  $k$ th range set and  $d$  denotes the true range to be estimated.

Figure 1 is the distance versus MSE averages. As the distance increased, the MSE average increased and the MSE averages of the proposed methods were lower than those of the other methods.

Figure 2 is the MSE averages versus the standard deviation of inliers. The MSE averages of the proposed methods were lower than those of the other existing methods based on the median in Figure 2. The performances of all robust methods deteriorated as the standard deviation of LOS error was increased.

Figure 3 shows the MSE averages as a function of standard deviation of NLOS noise. The MSE averages for the proposed robust shrinkage range estimation methods were lower than those of the other methods. The localization performances of the proposed and median-based existing algorithms were not affected by the NLOS noise because the Hampel and skipped filters are insensitive to the adverse effects of outliers.

Figure 4 shows the MSE averages versus the bias. The MSE averages of all methods were nearly constant as the bias

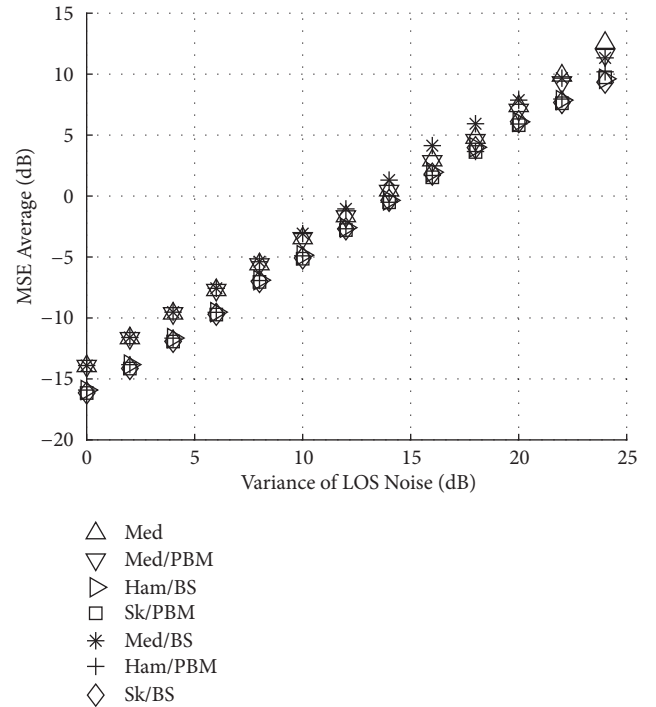


FIGURE 2: MSE averages of the range estimation algorithms as a function of variance of LOS noise (bias of NLOS noise ( $\mu_2$ ): 4 m, contamination ratio: 30%, and standard deviation of NLOS noise ( $\sigma_2$ ): 100 m).

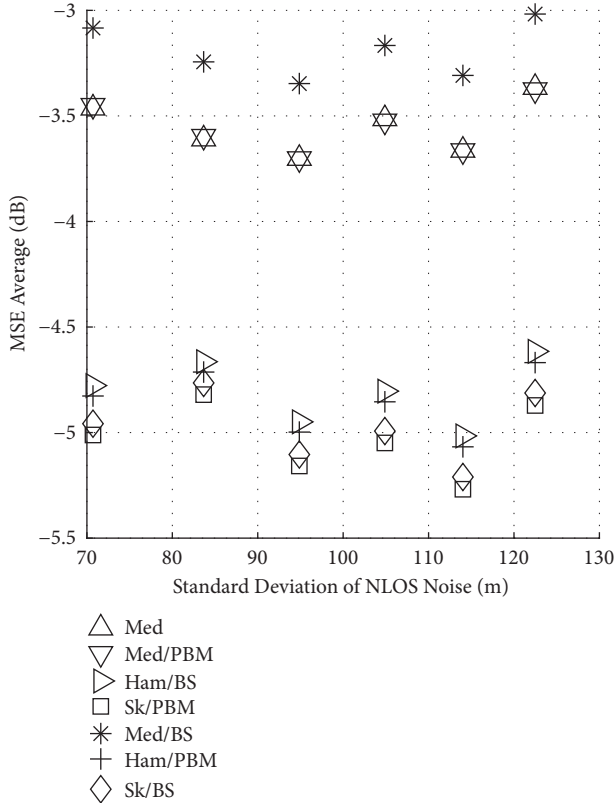


FIGURE 3: Comparison of MSE averages of the proposed estimators with that of the existing methods (contamination ratio ( $\epsilon$ ): 30%, the bias of NLOS noise ( $\mu_2$ ): 4 m, and standard deviation of LOS noise ( $\sigma_1$ ):  $\sqrt{10}$  m).

varied and the proposed methods outperformed the other existing algorithms. Namely, the estimation performances of the proposed range estimation algorithms are not affected by the bias because the Hampel and skipped filters are robust to the outliers.

Figure 5 shows the variation of the MSE averages with respect to the parameter  $t$  in (9). The MSE averages of the proposed algorithms, i.e., the Hampel and skipped filter-based methods, were much affected by the selection of parameter  $t$ , but those of the median-based methods were nearly constant and the MSE average of the proposed algorithms was minimal at  $t = 1.5$ . The MSE averages of the proposed methods are sensitive to the parameter  $t$  because  $P^{h,f}$  and  $P^{s,f}$  are dependent on the value of  $t$ .

Figure 6 is the sample size versus the MSE averages. Again, the proposed range estimation methods outperformed the other methods, as shown in Figure 6 and the MSE averages decreased as the sample size increased. Figure 7 shows the variation of the MSE averages with respect to the contamination ratio ( $\epsilon$ ). When the contamination ratio was lower than 50%, the MSE averages of all algorithms increased slightly as the contamination ratio increased. However, when the contamination ratio became larger than 50%, the MSE averages of the existing range estimation methods were significantly increased. Meanwhile, those of the proposed

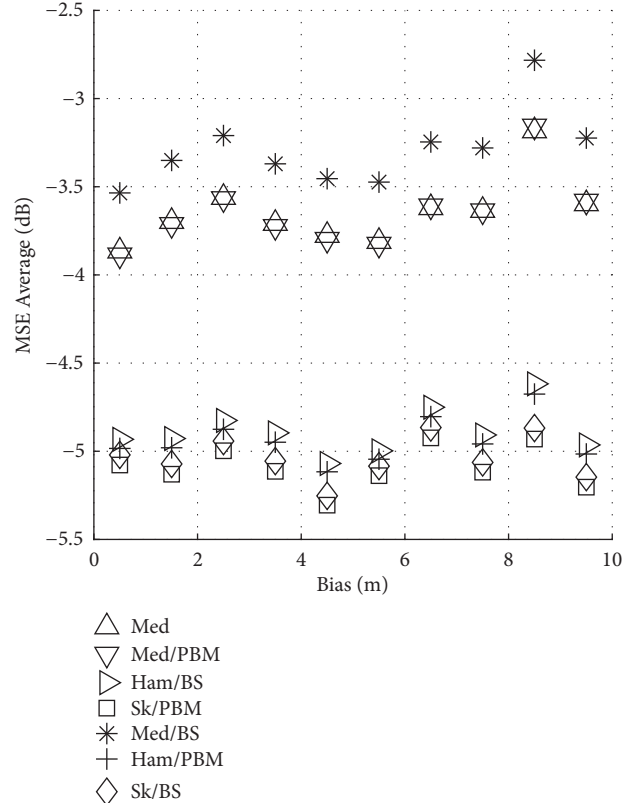


FIGURE 4: MSE averages of the range estimation algorithms as a function of bias (contamination ratio: 30%, standard deviation of LOS noise ( $\sigma_1$ ):  $\sqrt{10}$  m, and standard deviation of NLOS noise ( $\sigma_2$ ): 100 m).

methods were slightly incremented. Figure 8 shows the true and approximated variances of the ML range estimator. The true variance and approximated variance using the Taylor-series were nearly the same when the standard deviation of LOS noise was  $\sqrt{10}$  m. However, the approximated variance diverged from the true variance when the standard deviation of LOS noise increased to 17 m because the Taylor-series was adopted. Thus, the approximated variance should be utilized to apply the shrinkage estimator effectively.

## 6. Conclusions

The robust shrinkage range estimation methods were developed utilizing the Hampel filter, skipped filter, PBM, and BS estimators. Namely, the concepts of robustness for the Hampel and skipped filters and shrinkage for the PBM and BS estimators were mixed. The MSE performances of the proposed robust shrinkage methods were superior to those of the existing median-based shrinkage algorithms in the various simulation environments. Note that the MSE performances of the proposed methods were more robust, even in the regimes where  $\epsilon \geq 0.5$ , than those of the median-based shrinkage algorithms. Also, the proposed algorithms were developed in closed-form; thus, the computational complexities would be lower than those of the iteration methods.

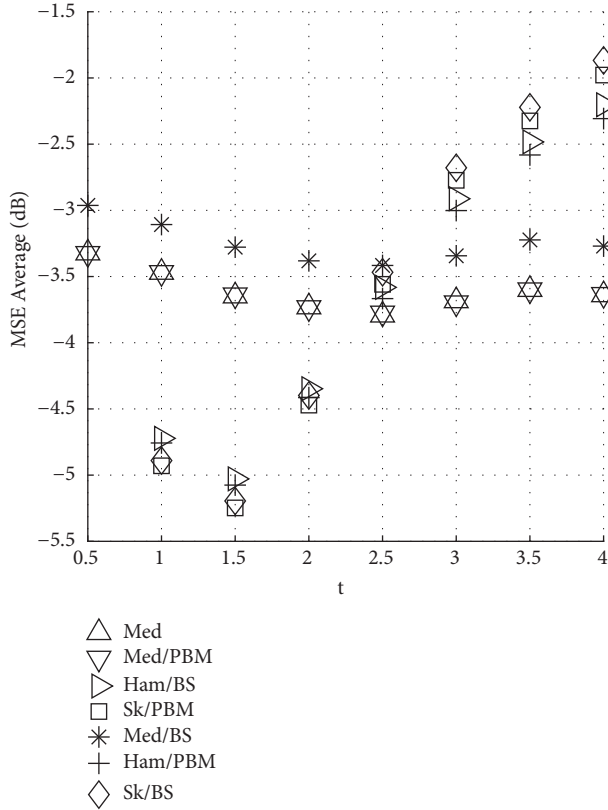


FIGURE 5: MSE averages of the range estimation algorithms as a function of parameter (t) (bias of NLOS noise ( $\mu_2$ ): 4 m, contamination ratio: 30%, standard deviation of LOS noise ( $\sigma_1$ ):  $\sqrt{10}$  m, and standard deviation of NLOS noise ( $\sigma_2$ ): 100 m).

**Data Availability**

The datasets generated during and/or analysed during the current study are not publicly available due to the fact that ftp is not available but are available from the corresponding author upon reasonable request.

**Conflicts of Interest**

The authors declare that they have no conflicts of interest.

**Authors' Contributions**

In this research paper, Chee-Hyun Park proposed a robust shrinkage distance estimation algorithm. Joon-Hyuk Chang carried out the correspondence of the paper.

**Acknowledgments**

This work was supported by Projects for Research and Development of Police Science and Technology under Center for Research and Development of Police Science and Technology and Korean National Police Agency funded by the Ministry of Science and ICT (PA-J000001-2017-101) and was supported by the National Research Foundation of Korea

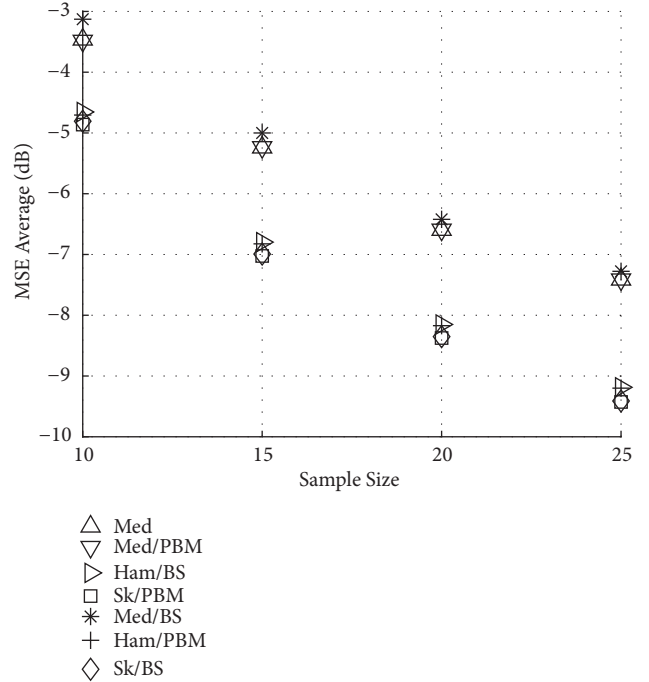


FIGURE 6: MSE averages of the range estimation algorithms as a function of sample size (contamination ratio: 30%, standard deviation of LOS noise ( $\sigma_1$ ):  $\sqrt{10}$  m, and standard deviation of NLOS noise ( $\sigma_2$ ): 100 m).

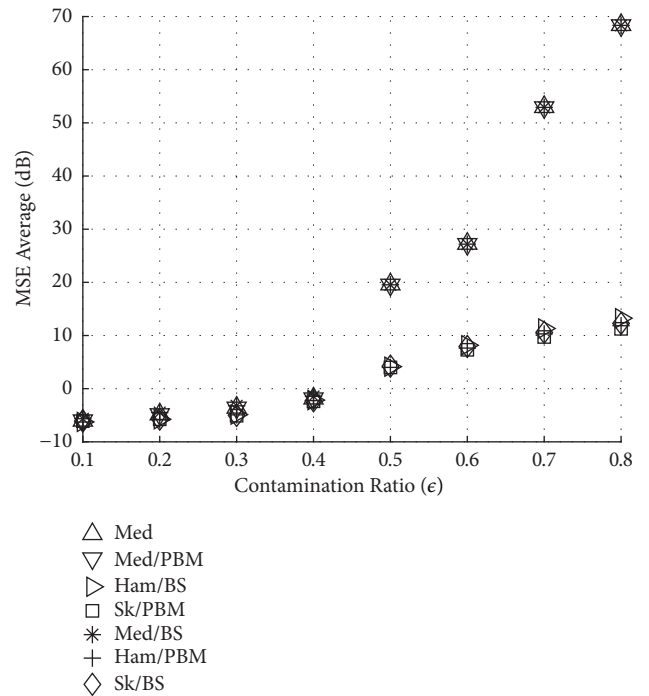


FIGURE 7: Comparison of MSE averages of the proposed estimators as a contamination ratio.

(NRF) grant funded by the Korea Government (MOE) (no. 201800000000513).



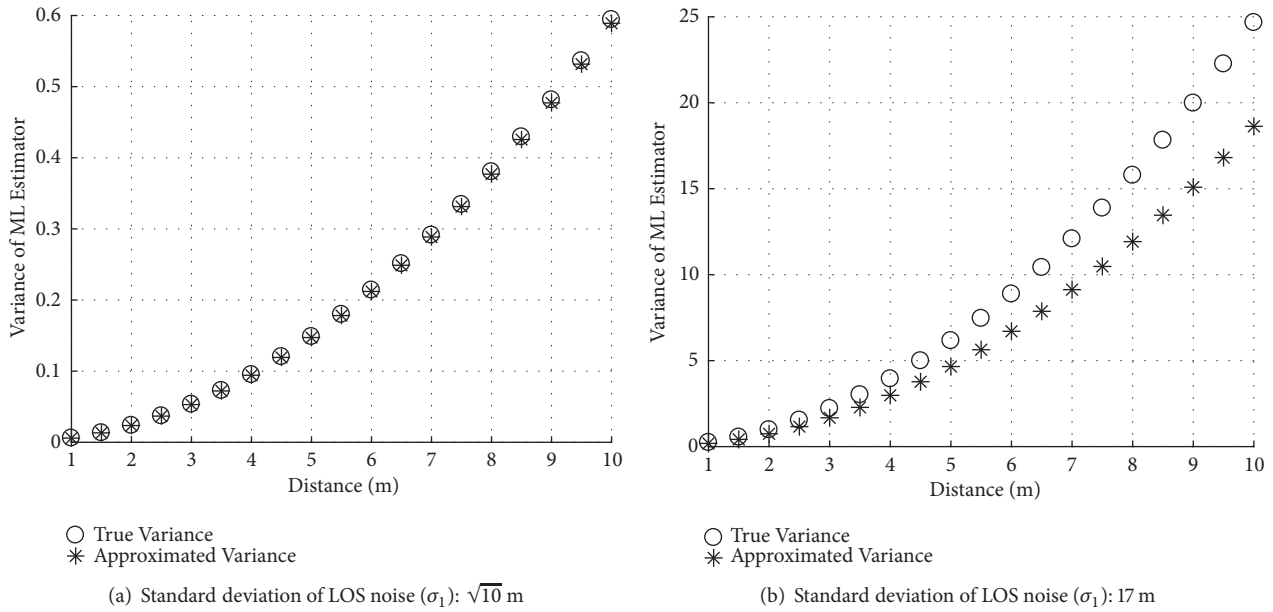


FIGURE 8: Comparison of true and approximated variances of the ML estimator as a function of distance.

## References

- [1] A. Coluccia and A. Fascista, "On the Hybrid TOA/RSS Range Estimation in Wireless Sensor Networks," *IEEE Transactions on Wireless Communications*, vol. 17, no. 1, pp. 216–218, 2018.
- [2] D. Macii, A. Colombo, P. Pivato, and D. Fontanelli, "A data fusion technique for wireless ranging performance improvement," *IEEE Transactions on Instrumentation and Measurement*, vol. 42, no. 8, pp. 1905–1915, 1994.
- [3] A. Catovic and Z. Sahinoglu, "The Cramer-Rao bounds of hybrid TOA/RSS and TDOA/RSS location estimation schemes," *IEEE Communications Letters*, vol. 8, no. 10, pp. 626–628, 2004.
- [4] S. D. Chitte, S. Dasgupta, and Z. Ding, "Distance estimation from received signal strength under log-normal shadowing: Bias and variance," *IEEE Signal Processing Letters*, vol. 16, no. 3, pp. 216–218, 2009.
- [5] L. Gui, M. Yang, P. Fang, and S. Yang, "RSS-based indoor localisation using MDCE," *IET Wireless Sensor Systems*, vol. 7, no. 4, pp. 98–104, 2017.
- [6] Y. Eldar, "Uniformly Improving the Cramér-Rao Bound and Maximum-Likelihood Estimation," *IEEE Transactions on Signal Processing*, vol. 54, no. 8, pp. 2943–2956, 2006.
- [7] Z. Ben-Haim and Y. C. Eldar, "Blind minimax estimation," *Institute of Electrical and Electronics Engineers Transactions on Information Theory*, vol. 53, no. 9, pp. 3145–3157, 2007.
- [8] L. Li, "Bayesian Shrinkage Estimation in Exponential Distribution Based on Record Values," in *Proceedings of the 2011 International Conference on Computational and Information Sciences (ICCIS)*, pp. 1159–1162, Chengdu, China, October 2011.
- [9] R. R. Wilcox, *Introduction to robust estimation and hypothesis testing*, Academic Press, 3rd edition, 2012.
- [10] R. K. Pearson, Y. Neuvo, J. Astola, and M. Gabbouj, "Generalized Hampel Filters," *EURASIP Journal on Advances in Signal Processing*, pp. 1–18, 2016.
- [11] F. R. Hampel, "The breakdown points of the mean combined with some rejection rules," *Technometrics*, vol. 27, no. 2, pp. 95–107, 1985.
- [12] D. E. Tyler, "A distribution-free  $M$ -estimator of multivariate scatter," *The Annals of Statistics*, vol. 15, no. 1, pp. 234–251, 1987.
- [13] F. Pascal, Y. Chitour, J.-P. Ovarlez, P. Forster, and P. Larzabal, "Covariance structure maximum-likelihood estimates in compound Gaussian noise: existence and algorithm analysis," *IEEE Transactions on Signal Processing*, vol. 56, no. 1, pp. 34–48, 2008.
- [14] Y. I. Abramovich and N. K. Spencer, "Diagonally loaded normalised sample matrix inversion (LNSMI) for outlier-resistant adaptive filtering," in *Proceedings of the 2007 IEEE International Conference on Acoustics, Speech and Signal Processing, ICASSP '07*, pp. III1105–III1108, USA, April 2007.
- [15] Y. Chen, A. Wiesel, and I. Hero, "Robust shrinkage estimation of high-dimensional covariance matrices," *IEEE Transactions on Signal Processing*, vol. 59, no. 9, pp. 4097–4107, 2011.
- [16] T. S. Rappaport, *Wireless Communications: Principles and Practice*, Prentice Hall, 2nd edition, 2002.
- [17] F. Yin, C. Fritsche, F. Gustafsson, and A. M. Zoubir, "EM- and JMAP-ML based joint estimation algorithms for robust wireless geolocation in mixed LOS/NLOS environments," *IEEE Transactions on Signal Processing*, vol. 62, no. 1, pp. 168–182, 2014.
- [18] N. Patwari, J. N. Ash, S. Kyperountas, A. O. Hero III, R. L. Moses, and N. S. Correal, "Locating the nodes: cooperative localization in wireless sensor networks," *IEEE Signal Processing Magazine*, vol. 22, no. 4, pp. 54–69, 2005.
- [19] P. Tarrío, A. M. Bernardos, J. A. Besada, and J. R. Casar, "A new positioning technique for RSS-Based localization based on a weighted least squares estimator," in *Proceedings of the 2008 IEEE International Symposium on Wireless Communication Systems*, pp. 633–637, Reykjavik, Iceland, October 2008.
- [20] F. Yin, C. Fritsche, F. Gustafsson, and A. M. Zoubir, "TOA-based robust wireless geolocation and cramer-rao lower bound analysis in harsh LOS/NLOS environments," *IEEE Transactions on Signal Processing*, vol. 61, no. 9, pp. 2243–2255, 2013.
- [21] F. Gustafsson and F. Gunnarsson, "Mobile positioning using wireless networks: possibilities and fundamental limitations

- based on available wireless network measurements,” *IEEE Signal Processing Magazine*, vol. 22, no. 4, pp. 41–53, 2005.
- [22] U. Hammes, E. Wolsztynski, and A. M. Zoubir, “Robust tracking and geolocation for wireless networks in NLOS environments,” *IEEE Journal of Selected Topics in Signal Processing*, vol. 3, no. 5, pp. 889–901, 2009.
- [23] C.-H. Park and J.-H. Chang, “Shrinkage estimation-based source localization with minimum mean squared error criterion and minimum bias criterion,” *Digital Signal Processing*, vol. 29, pp. 100–106, 2014.
- [24] G. Casella and R. L. Berger, *Statistical Inference*, Cengage Learning, 2nd edition, 2001.
- [25] P. J. Rousseeuw and A. M. Leroy, *Robust Regression and Outlier Detection*, John Wiley & Sons, 1987.
- [26] Li and Y. H. Hu, “Energy-based collaborative source localization using acoustic microsensor array,” *EURASIP Journal on Advances in Signal Processing*, vol. 89, pp. 1–11, 2016.
- [27] K. C. Ho and M. Sun, “An accurate algebraic closed-form solution for energy-based source localization,” *IEEE Transactions on Audio, Speech and Language Processing*, vol. 15, no. 8, pp. 2542–2550, 2007.

## Research Article

# Spatiotemporal Statistical Channel Model for Indoor Corridor at 14 GHz, 18 GHz, and 22 GHz Bands

Nicholas O. Oye  and Thomas J. O. Afullo

*Discipline of Electrical, Electronic and Computer Engineering, Howard College Campus, University of KwaZulu-Natal, Durban 4041, South Africa*

Correspondence should be addressed to Nicholas O. Oye; 217063428@stu.ukzn.ac.za

Received 9 August 2018; Revised 26 October 2018; Accepted 21 November 2018; Published 9 December 2018

Guest Editor: Ernest Kurniawan

Copyright © 2018 Nicholas O. Oye and Thomas J. O. Afullo. This is an open access article distributed under the Creative Commons Attribution License, which permits unrestricted use, distribution, and reproduction in any medium, provided the original work is properly cited.

Several techniques have been proposed to overcome challenges of meeting demands for higher data rates in wireless communication. Space-time diversity method is proposed to exploit spatiotemporal nature of the channel; hence, a comprehensive knowledge of the spatiotemporal properties of a channel is required. In this paper, a measurement-based channel model that considers both delay and angular domains of an indoor corridor channel for 14 GHz, 18 GHz, and 22 GHz is proposed. A nonparametric Gaussian kernel density estimation method is applied for cluster identification for the three frequency bands. This work proposes a spatiotemporal model that conditions the model parameters on the azimuthal spatial domain. The clusters are modeled on the complete azimuth plane and a Gaussian estimation distribution is fitted onto the empirical data plot. Both clusters and multipath components are modeled and results are compared with Saleh-Valenzuela model parameter values. The results show that both clusters and multipath components can be estimated by probability density functions that follow Gaussian and Laplacian fits on the spatial domain for indoor corridor environment, respectively.

## 1. Introduction

The challenges of spectrum shortage can be overcome by putting in place efficient and reliable wireless communication channel models. The frequency bands above 6 GHz promise large bandwidths and are thus desirable for application in fifth generation (5G) networks and beyond [1]. For optimum wireless communication systems' operation, massive multiple-input-multiple-output (MIMO) techniques have been introduced with capabilities to exploit both delay and angular domains to maximize capacity [2]. A successful design and deployment of indoor environment systems such as Femto Access Points, relies on an in-depth knowledge of radio channel propagation in terms of spatiotemporal channel fading [3].

Many studies have considered both spatial and temporal correlation properties of a propagation channel [3–5]. The space-time processing techniques' performance is dependent on efficient modeling of the correlation between spatial and temporal domains of propagation at a particular frequency

band. Based on channel measurements, the Saleh-Valenzuela (S-V) model is one of the popular and widely used models that describe the stochastic properties of path time of arrival (ToA) and amplitudes of the resolvable multipath components (MPCs) in a wireless communication system. It assumes the Poisson process in modeling both MPCs' and clusters' ToA [6]. This model was used as the basis for the IEEE 802.15.3a model and is also used to compare standardization proposals for wireless personal area networks (PANs) [7].

An extension of S-V model (ES-V) was introduced which captured both temporal and angular information [8–10] for low-data speed wireless PANs. It assumes independence of spatial and temporal domains of each other. In addition, stochastic radio channel model (SRCM) based on measurement data [11] was conducted at 24 GHz frequency band in an office environment under line-of-sight (LOS) and non-line-of-sight (NLOS) scenarios. However, these models did not address the correlation of spatial and temporal properties of the channel, which are necessary for exploitation

of space-time techniques in signal processing. In [12], a measurement-based double-directional model for 60 GHz MIMO channel in a conference room was presented. The authors proposed a spatiotemporal channel model. Two approaches were provided for modeling spatiotemporal properties at 60 GHz band, namely, stochastic and ray-tracing (semideterministic approach).

More recently, the rotated directional antenna (RDA) and the uniform virtual array (UVA) approaches were adopted in investigation of a 60 GHz indoor office wireless channel in three dimensional (3-D) space [13]. The study considered the azimuth and the corresponding elevation domains simultaneously. Generally, the modeling was based on the ES-V model with specific emphasis on angular domain. However, these approaches did not incorporate the spatiotemporal correlation with parameters conditioned on the spatial domain in indoor corridor environments. Other studies on millimeter wave channel characterization can be found in [14–19].

The contribution of this paper is threefold: first, to have an in-depth study of statistical propagation channel characterization of the 14 GHz, 18 GHz, and 22 GHz bands in an indoor environment. In particular, it seeks to study the clustering of MPCs and spatial and temporal correlation characteristics of an indoor corridor channel. Second, to propose a spatiotemporal model that incorporates correlation properties and clustering with parameter conditioning on the spatial domain. Finally, this paper describes the impact of structural design, construction materials, and general geometry of radio wave propagation channel in the indoor environment on the propagation characteristics at 14 GHz, 18 GHz, and 22 GHz. The intercluster (cluster distribution) and intracluster (MPC distribution) channel parameters and correlation properties are analyzed using two joint probability functions (pdfs).

The rest of this paper is organized as follows: Section 2 presents the channel measurement set up, environment, and cluster identification. A kernel density estimate (KDE) approach is described in this section. In Section 3, spatiotemporal model that assumes dependence in delay and spatial domains is described. The proposed model is presented under characterization of channel parameters in Section 4. Validation of the proposed channel model and conclusion are given in Sections 5 and 6, respectively.

## 2. Channel Measurements and Data Processing

*2.1. Measurement Environment.* The measurement campaign was performed in an indoor corridor environment of the 5<sup>th</sup> floor of the Discipline of Electrical, Electronic and Computer Engineering building, University of Kwa-Zulu Natal, South Africa. The structural and construction materials of the corridor are made up of concrete and brick walls, tiled floor, plasterboard ceiling, and wooden doors to offices as depicted in Figure 1. The corridor is terminated by wooden doors on both ends and has a volume of  $30 \times 1.4 \times 2.7 \text{ m}^3$ . Measurements were conducted with no movements of people in the corridor and doors remained closed. The corridor acted as a waveguide through which the waves were propagated from the Tx to

the Rx via the direct path and the reflected or guided paths. Several scatterers (i.e., walls, floor, ceiling, lumps, doors, etc.) were in the vicinity of the Tx and the Rx that generated MPCs. The spatiotemporal correlation was analyzed in terms of the intercluster and intracluster parameters. The correlation between the spatial and temporal aspects of the propagation indoor corridor channel was modeled with the parameter values conditioned on the spatial domain for all the studied frequency bands.

*2.2. Measurement Set Up.* Channel measurements were done using a radio frequency signal generator (Rohde and Schwarz SMF 100A) and signal analyzer with a frequency range from 20 Hz to 40 GHz and maximum analysis bandwidth of 120 MHz (Rohde and Schwarz FSIQ 40) at the Tx and the Rx sides, respectively. A trigger signal was used to synchronize the Tx and the Rx systems during measurements. A pair of wideband vertically polarized (V-V) directional horn antennas with dBi gain of 19.5, half power beamwidth of  $19.2^\circ$  in elevation, and  $18.4^\circ$  in azimuth for 14 GHz were used as illustrated in Figure 2. At the frequency band of 18 GHz, the antenna gain, half power beamwidth elevation, and azimuth were 20.95 dBi,  $15.6^\circ$ , and  $15.4^\circ$ , respectively; while at 22 GHz, the antenna gain was 22.1 dBi and half power beamwidth was  $13^\circ$  in elevation and  $15^\circ$  in azimuth [20].

The Tx was fixed at one end of the corridor while the Rx was placed at 1 m, 4 m, 8 m, and 12 m separations from the Tx for all the measurements at each frequency band on a LOS scenario as illustrated in Figure 1. Both the Tx and the Rx antennas were fixed at 1.6 m above the floor for measurements in all the frequency bands. The receiving horn antenna was rotated on the azimuth plane in steps of  $30^\circ$  from  $0^\circ$  (boresight angle). Consequently, the direct and the reflected rays were captured both on spatial and temporal domains to describe the characteristics of the propagation channel. The elevation angle of both the Tx and the Rx horn antennas was kept at  $0^\circ$  for all the measurement points. The highly directional Tx and Rx antennas and geometry of the measurement environment realized very low signal levels reflected from the ceiling and floor in this research. The ceiling and floor distances were further from transmitting and receiving antennas as compared to side walls.

*2.3. Cluster Identification.* Measurements were performed in the time domain with the Rx antenna rotated on the azimuthal plane to capture the properties of the spatial domain of the channel. A cluster is defined in this paper as MPCs with similar characteristics on the spatial and temporal domains. Several researchers have reported diverse definitions of a cluster [21–23]. The MPCs resulted from reflections from scatterers along the propagation channel, a phenomenon previously reported in [6]. A number of parametric clustering techniques have been proposed such as K-means and Fuzzy C-means clustering methods [13, 24, 25]. However, we used the KDE technique which is a nonparametric density estimation procedure [26]. This technique was used in the identification of clusters from the measurements data. The KDE technique is appealing as it is

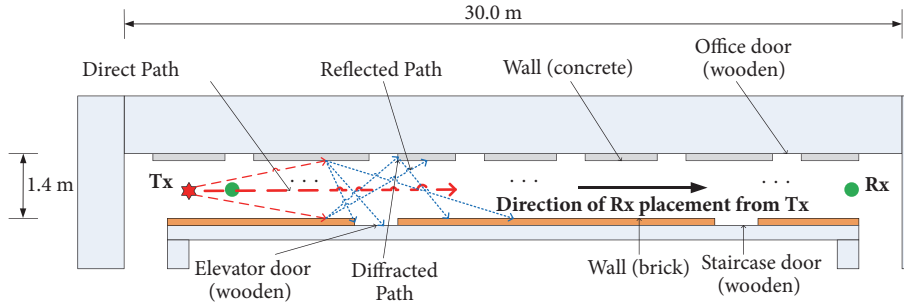


FIGURE 1: Indoor corridor floor layout.

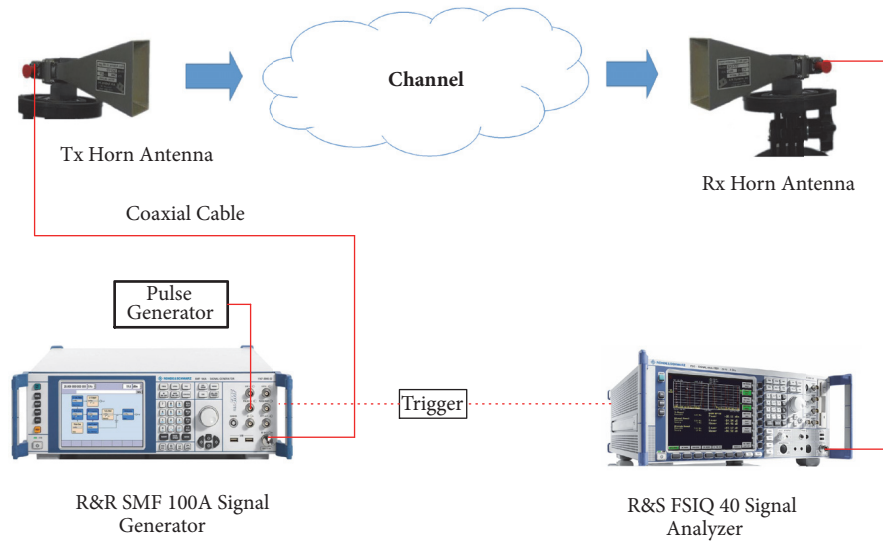


FIGURE 2: Measurement equipment.

solely based on the sample and hence avoids specification of the wrong parametric family as much as possible with the parametric approaches [27].

A joint delay and angular clustering method such as KDE has been used in [3] to make identification of multipath clusters more realistic and practical. Recently, authors in [28] proposed a new algorithm for clustering measurement data based on KDE. In this paper, a Gaussian KDE is proposed to estimate the MPCs clusters in an indoor environment. We conducted measurements using a custom-made channel sounder and the applied estimation method fairly clustered the MPCs in both time and angular domains. The data set of our measurements has two components: spatial and temporal domains. We applied a two-dimensional (2-D) kernel analysis directly as it is often easier to visualize densities in 2-D [26]. The KDE for a 2-D data set can be expressed as in (1):

$$\hat{f}(t, \Theta) = \frac{1}{nh_t h_\Theta} \sum_{i=1}^n K_t \left( \frac{t - t_i}{h_t} \right) \cdot K_\Theta \left( \frac{\Theta - \Theta_i}{h_\Theta} \right) \quad (1)$$

where  $h_\Theta$  and  $K_\Theta(\cdot)$ , and  $h_t$  and  $K_t(\cdot)$  are bandwidths and kernel functions of spatial and temporal domains, respectively, and  $n$  is the number of observations of measurement data for  $t, \Theta \in \mathfrak{R}$ . We applied a Gaussian KDE technique on the 2-D data set because of its robustness, simplicity, and convenience [3, 29] as expressed in (2) and (3) for time and angular domains, respectively:

$$K_t \left( \frac{t - t_i}{h_t} \right) = \frac{1}{\sqrt{2\pi}} \exp \left( -\frac{(t - t_i)^2}{2h_t^2} \right) \quad (2)$$

$$K_\Theta \left( \frac{\Theta - \Theta_i}{h_\Theta} \right) = \frac{1}{\sqrt{2\pi}} \exp \left( -\frac{(\Theta - \Theta_i)^2}{2h_\Theta^2} \right) \quad (3)$$

Optimal bandwidth was automatically chosen without a compromise between under- or oversmoothing [26]. Figures 3, 4, and 5 show the spatiotemporal MPCs contour plots of the measurement data for the three frequency bands. From the plots, it is clearly observable that MPC clusters exist in both space and time domains. For instance, a scatter plot is shown in Figure 6 for 22 GHz MPCs received in the

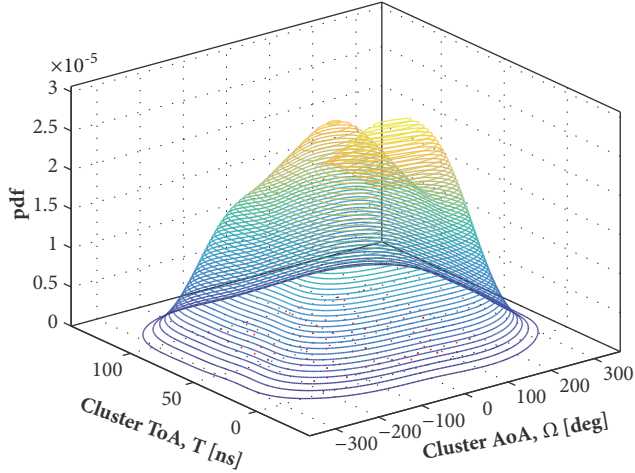


FIGURE 3: MPCs AoA-ToA contour plot for 14 GHz.

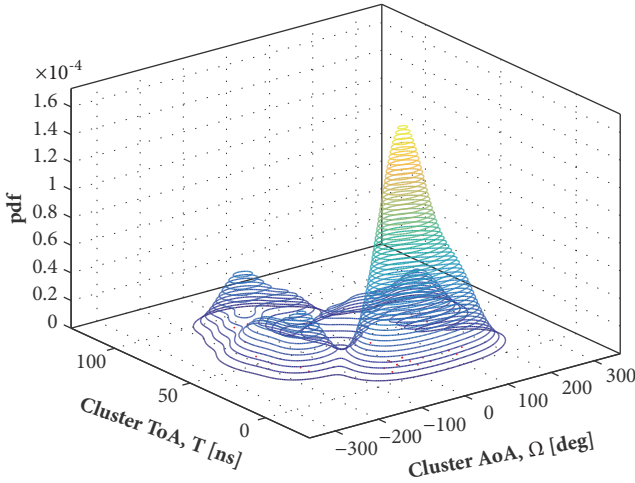


FIGURE 4: MPCs AoA-ToA contour plot for 18 GHz.

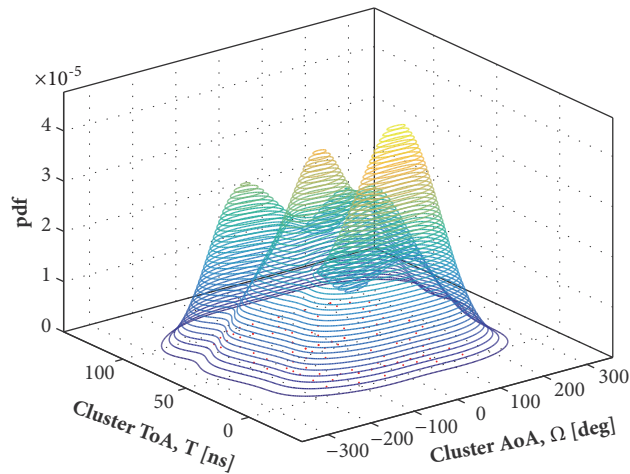


FIGURE 5: MPCs AoA-ToA contour plot for 22 GHz.

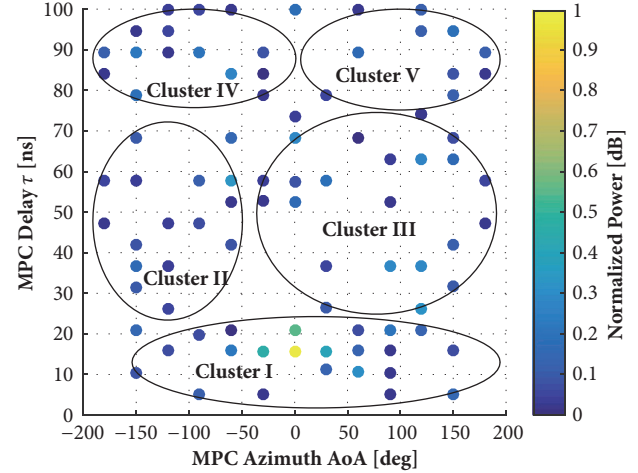


FIGURE 6: Scatter plot of MPCs for 22 GHz.

corridor indicating the location in space and time where the estimated clusters were positioned. After the 2-D Gaussian KDE processing, the clusters were singled out by visual inspection. Other works that employed visual inspection to identify clusters are [3, 6, 10].

### 3. Spatiotemporal Statistical Model

As reported in the S-V model, multipath components arrive at the receiver in clusters with delayed time of arrival and attenuated amplitudes [6]. The MPCs are reflected rays from scatterers that act as image sources along the propagation path. In an indoor corridor environment, these scatterers are generally the internal side walls, floor, ceiling, staircase, lamps, doors, and windows. Measurement data has thus been used to statistically characterize and model the indoor propagation channel such as S-V model.

The model presents parameters that can be used in simulation of the channel for in-depth understanding of the propagation phenomenon of the indoor corridor environment. The ES-V model is widely used and is based on clusters to derive channel parameters with the impulse response given by (4) [12]:

$$h(t, \Theta) = \sum_{m=0}^M \sum_{n=0}^{N_m} \beta_{n,m} e^{j\chi_{n,m}} \delta(t - T_m - \tau_{n,m}) \dots \delta(\Theta - \Omega_m - \omega_{n,m}) \quad (4)$$

where  $h$  is the channel response and  $\beta_{n,m}$  is the complex amplitude of the  $n$ th MPC in the  $m$ th cluster.  $T_m$  and  $\Omega_m$  are the ToA and angle of arrival (AoA) of the  $m$ th cluster, respectively;  $\tau_{n,m}$  and  $\omega_{n,m}$  are the ToA and AoA of the  $n$ th ray (i.e., MPC) in the  $m$ th cluster, respectively;  $\chi_{n,m}$  is the phase of each MPC; and  $\delta(\cdot)$  is the Dirac delta function.  $\chi_{n,m}$  is assumed to randomly and uniformly vary over  $[0, 2\pi)$ . The

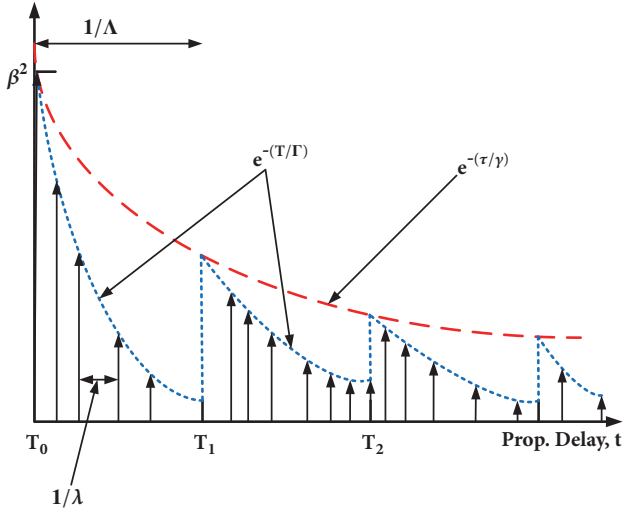


FIGURE 7: S-V mode for indoor multipath propagation.

mean-squared power of the  $n$ th ray in the  $m$ th cluster is given by (5) and (6) [12] and depicted in Figure 7:

$$\overline{\beta_{n,m}^2} = \beta^2(T_m, \tau_{n,m}) \quad (5)$$

$$= \beta^2(0,0)e^{-T_m/\Gamma}e^{-\tau_{n,m}/\gamma} \quad (6)$$

where the cluster and ray ToA decay constants are represented by  $\Gamma$  and  $\gamma$ , respectively.  $\beta^2(0,0)$  is the average power of the first ray of the first cluster [10]. The cluster and ray arrival times can be described by two Poisson processes if delay and angular properties are modeled independently. The interarrival time of clusters can be characterized by an exponential probability density function as presented in Figure 8 for the 18 GHz band. In addition, ray interarrival times within each cluster can be independently described in the same manner as shown by histogram plot in Figure 9. Consequently, each cluster's arrival time is estimated by a distributed random variable that decays exponentially and is conditioned on the arrival of the previous cluster. The distributions of cluster and ray arrival rates, assumed independence, can be expressed as in (7) and (8), respectively [12]:

$$p(T_m | T_{m-1}) = \Lambda e^{-\Lambda(T_m - T_{m-1})}, \quad m > 0 \quad (7)$$

$$p(\tau_{n,m} | \tau_{n-1,m}) = \lambda e^{-\lambda(\tau_{n,m} - \tau_{n-1,m})}, \quad m > 0 \quad (8)$$

where  $\Lambda$  is the cluster interarrival rate and  $\lambda$  is the ray arrival rate (see Figure 7).

It is worth noting that the ES-V model assumes that time and angular parameters can be modeled independently. However this work jointly model the delay and spatial domain characteristics using a conditional angular-delay distribution function [3, 12].

#### 4. Characterization of the Channel Parameters

In this section, we characterize the propagation channel in terms of intercluster and intracluster parameters. A statistical

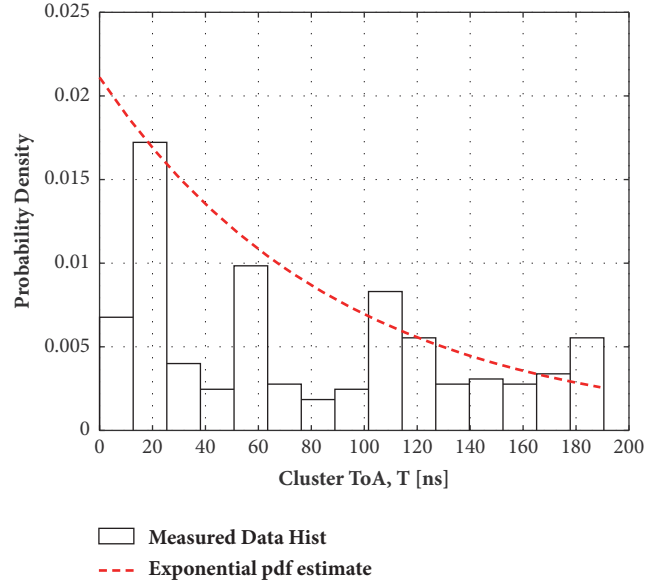


FIGURE 8: Marginal ToA pdf for clusters at 18 GHz.

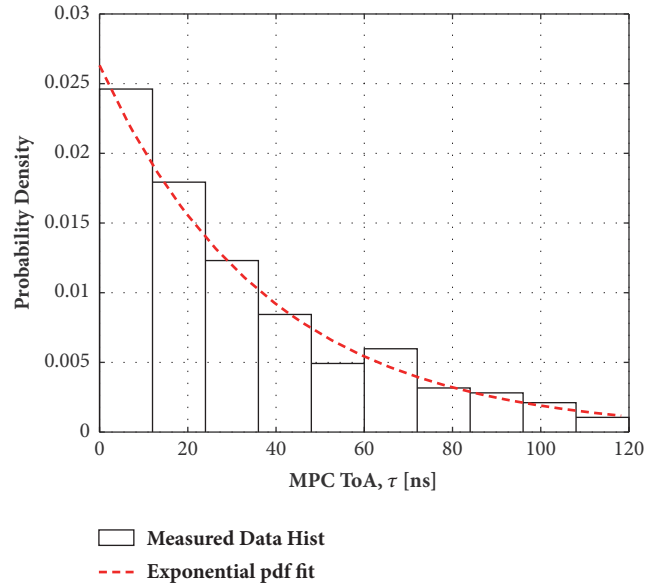


FIGURE 9: Intercluster marginal ToA pdf for MPCs at 22 GHz.

characterization of the behavior of these parameters may be carried out by fitting the measurement data against the proposed theoretical distributions. The estimated intercluster and intracluster parameters results are presented and compared with S-V model values discussed in Section 3. As stated earlier, three frequency bands are considered in an indoor corridor environment (i.e., 14 GHz, 18 GHz, and 22 GHz) in LOS scenario and the average number of clusters for the 14 GHz band on the angular domain is represented by the histogram plot of Figure 10.

**4.1. Intercluster Parameters.** The correlation between temporal and angular domains is noted to generate a joint

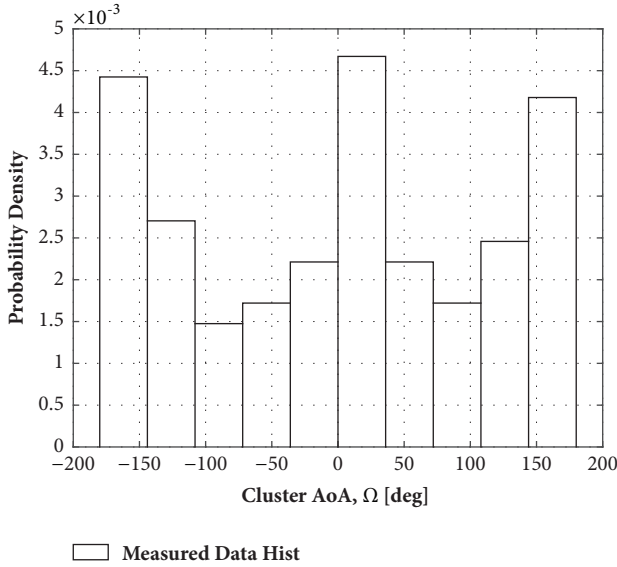


FIGURE 10: Average number of clusters at 14 GHz.

distribution of cluster-based model. The joint probability distribution function (pdf) of clustering  $f(T_m, \Omega_m)$  is given by (9):

$$f(T_m, \Omega_m) = f(\Omega_m | T_m) \cdot f(T_m) \quad (9)$$

where  $f(\Omega_m | T_m)$  is conditional AoA pdf for the cluster and  $f(T_m)$  is the marginal ToA pdf for the cluster. We considered all possible AoAs for the received reflections in the indoor corridor to empirically determine the joint pdf. Different frequency bands were considered with Tx system placed at one end of the corridor while the Rx was successively placed at four different locations from the Tx and all possible AoAs captured. The received MPCs are modeled by the joint AoA pdfs for each of the frequency bands. Figures 3, 4, and 5 show the joint pdf,  $f(T_m, \Omega_m)$  for the 14 GHz, 18 GHz, and 22 GHz cases, respectively. Figure 6 shows the scatter plot of the estimated clustered MPCs for 22 GHz. The clustering technique shows that there are five clusters of MPCs in the indoor corridor arriving at the Rx.

The angular axes for all the bands span the range  $-180^\circ$  and  $+180^\circ$  to form the  $360^\circ$  full spatial azimuth span. We noted significant differences in the statistical analysis of the spatiotemporal domains of the channel at varying frequencies. MPCs that arrive at the Rx with both short and long delays at 14 GHz (Figure 3) have a wider angular range and uniform amplitude with three distinct clusters. The three clusters are due to the direct path and the reflected MPCs from both side walls. The 18 GHz band has paths with restricted angular range for short delays while having highly attenuated longer delay paths that have relatively wide angular range. Four clusters are observed as shown in Figure 4. This could be attributed to the effects of the corridor geometry and structural design, resulting in destructive interference. In addition, surface roughness could have resulted in higher distortion and attenuation at this particular frequency band. This phenomenon needs further investigation by considering

varying measurement environments. At 22 GHz band, five clusters were observed. The cluster with short delay paths has wider angular range than those with longer delays as seen in Figure 5. It is also notable that the signals are less attenuated as compared to 18 GHz although number of clusters increased. Received MPCs at the Rx over short delays are composed of the direct LOS path and/or reflections from structures in the vicinity of the Rx. The Rx placed in the corridor is surrounded by walls, doors, floor, and ceiling, thus the reflections come from a large angular range.

In Figure 4, for example, arrival paths with relatively short delay range have larger angular ranges and are observed to be reflected from both walls of the corridor. Arrival paths with larger delays are largely due to reflections from corridor end wall or multiple reflections within the corridor as radio waves are guided by the waveguide-like corridor. These paths of course suffer higher attenuation than early arrival ones because of longer paths traveled and multiple reflections. This characteristic of radio propagation in the channel is attributed to the general structure of the measurement environment (Figure 1). As expected, one observes that different frequency bands have different propagation characteristics in the same environment. The probability of path arrivals is highest at  $0^\circ$  and for the shorter delay ranges in all the frequency bands. In addition, larger delay paths have high probability at  $180^\circ$  due to corridor end wall reflections as shown in Figures 3, 4, and 5. Paths arriving from side walls incur least probabilities and are most attenuated. This is partly due to the geometry, structural design, and construction materials of the corridor. The cluster ToA has been modeled by the Poisson process that assumes independence of arrivals [6, 10]. However, in a regular structural design, such as indoor corridors, this independence does not hold [3]. In this paper, a nonparametric estimation of the pdf is used to model the arrivals based on measurement data. This is a more general approach with no *a priori* assumption of Poisson process satisfied by the cluster arrival times.

The empirical cluster AoA histogram density for 14 GHz is shown in Figure 10. The 14 GHz and 22 GHz frequency bands have a similar channel clusters behavior. Estimation of a cluster's marginal ToA pdf  $f(T_m)$  was done by accumulation of all the AoAs,  $\{\Omega_m\}_m \in M$  for 18 GHz as presented in Figure 8. The estimated pdf is plotted as the dotted curve and the  $f(T_m)$  is modeled by an exponential pdf expressed as in (10):

$$f(T_m) = \begin{cases} \frac{1}{\mu_T} \exp\left(-\frac{T_m}{\mu_T}\right), & T_m > 0 \\ 0, & \text{otherwise} \end{cases} \quad (10)$$

where  $\mu_T$  is the mean ToA.

The cluster joint AoA pdfs for 14 GHz, 18 GHz, and 22 GHz are estimated using this new technique.  $f(\Omega_m | T_m)$  is characterized by an empirical distribution that fits the data. We considered the azimuthal spatial range from  $-180^\circ$  to  $180^\circ$ . The cluster joint AoA pdf is further estimated using a Gaussian pdf as the mean and standard deviation values are determined. We observed low probability density values for clusters with arrival paths with longer delays. Figures



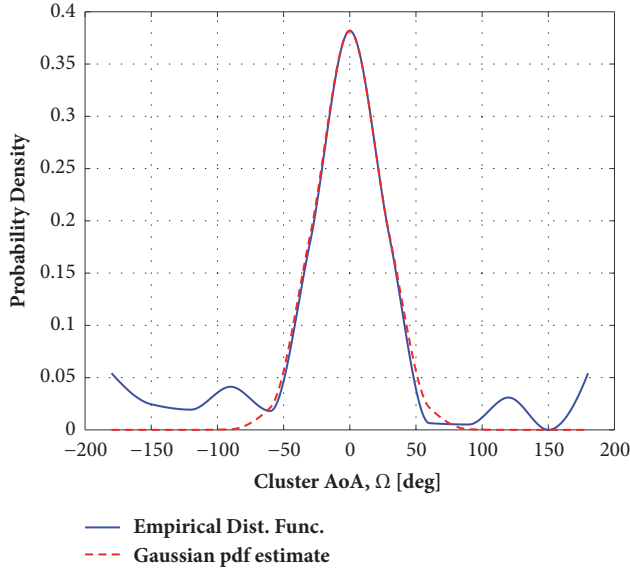


FIGURE 11: Cluster azimuth AoA pdf for 14 GHz.

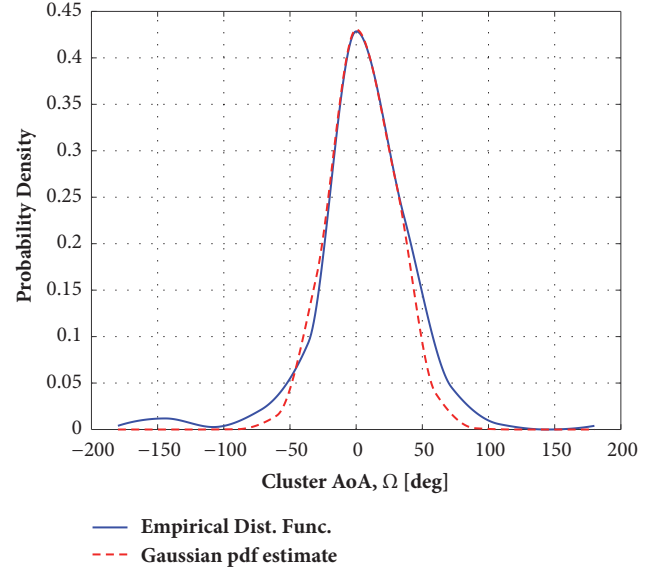


FIGURE 12: Cluster azimuth AoA pdf for 18 GHz.

11, 12, and 13 show the plots of the empirical distribution function and the estimated Gaussian pdfs. From the graphs, it is observed that a Gaussian pdf can closely estimate the cluster AoA in an indoor corridor at 14 GHz, 18 GHz, and 22 GHz frequency bands. The proposed Gaussian pdf to model the channel is given by (11):

$$f(\Omega_m, T_m) = \frac{1}{\sqrt{2\pi} \cdot \sigma_{\Omega_m}} \exp\left\{-\frac{\Omega_m^2}{2\sigma_{\Omega_m}^2}\right\} \quad (11)$$

where  $\sigma_{\Omega_m}$  is the standard deviation conditioned upon  $\Omega_m$ . However, the tails of the empirical distributions for 14 GHz and 22 GHz have pronounced clusters appearing between  $90^\circ$  and  $180^\circ$  and  $-90^\circ$  and  $-180^\circ$ . This may be due to the presence of strong MPCs received as reflected, scattered, and diffracted from back and side walls. The approximation errors at these spatial ranges are within the acceptable margin as the probability of occurrence in most cases is less than 0.08. For 18 GHz, the empirical values are approximated better as weaker and fewer MPCs were received from the back and side walls. This may be due to the impact of structural design and construction materials of the corridor at this propagation wavelength.

**4.2. Intracluster Parameters.** The ToA of the MPCs have been modeled by the Poisson process. In this approach, each cluster consists of a number of MPCs. To identify an individual ray composing a cluster, experimental measurements should be done in both spatial and temporal domains [30]. An extension of the proposed nonparametric projection of the pdf of the arrival time of clusters based on the measured data is adopted. The MPC marginal ToA pdf  $f(\tau_{n,m})$ , is estimated using the accumulated MPCs' AoAs,  $\{\omega_n\}_{n \in N}$ . Figure 9 shows the MPC marginal ToA histogram probability density for 22 GHz, with the number of MPCs estimated by an exponential pdf plotted in dotted curve. The observed results are in

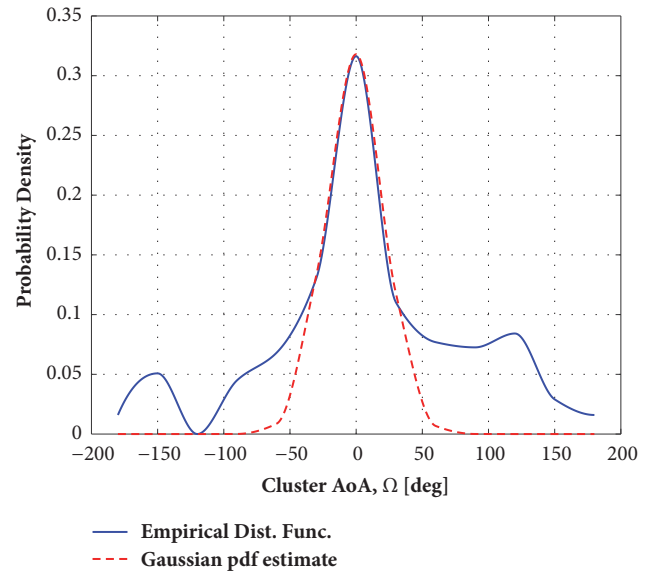


FIGURE 13: Cluster azimuth AoA pdf for 22 GHz.

agreement with [3, 31]. The joint MPCs position per cluster  $f(\tau_{n,m}, \omega_{n,m})$  can be expressed as (12):

$$f(\tau_{n,m}, \omega_{n,m}) = f(\omega_{n,m} | \tau_{n,m}) \cdot f(\tau_{n,m}) \quad (12)$$

where  $f(\omega_{n,m})$  is the MPC azimuth AoA pdf, expressed as a zero-mean Laplacian pdf in (13)

$$f(\omega_{n,m}, \tau_{n,m}) = \frac{1}{\sqrt{2}\sigma_\omega} \exp\left(-\sqrt{2}\frac{|\omega_{n,m}|}{\sigma_\omega}\right) \quad (13)$$

where  $\sigma_\omega$  is the standard deviation conditioned on the spatial domain for  $\tau_{n,m}$ . Figure 14 shows a scatter plot of the MPCs' AoA with respect to ToA while considering the MPCs' normalized power. The result shows that there is a correlation

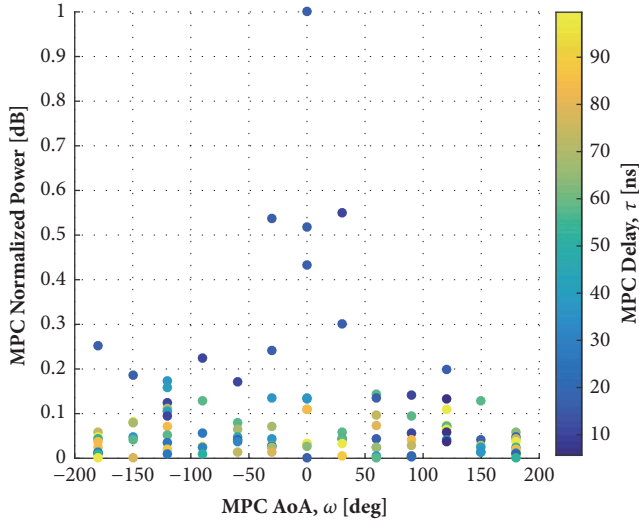


FIGURE 14: MPCs scatter plot of marginal AoA for 14 GHz.

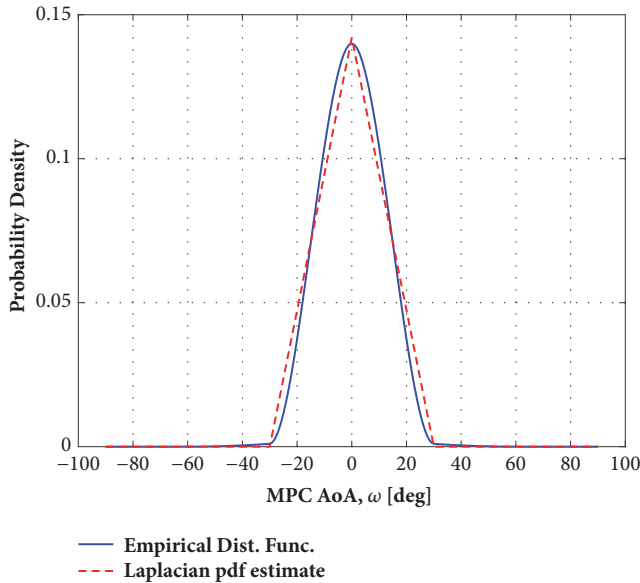


FIGURE 15: Intracluster azimuth AoA pdf for MPCs for 14 GHz.

between AoA and ToA with respect to power. The paths with shortest delays arrive at  $0^\circ$  with highest power. Paths with larger delays have much wider spatial range and lower power at the Rx. The delayed MPCs are attenuated on the side walls of the corridor as they travel along the corridor. This implies that the probability density of MPC's AoA is a joint distribution of time and angle of arrival, as indicated in (12).

Previous research has reported that the Laplacian distribution can be adopted to estimate the MPC's AoA pdf [3, 10, 11]. However, no justifiable reason is given over this choice except for it is fitting well against measured data. In [3], the effects of local and distant scatterers on the distribution of MPC's AoA at the Rx are illustrated. As can be seen in Figure 15, the scatters at the vicinity of the Rx can cause a large spatial range, and the Laplacian pdf neatly estimates the

empirical distribution. The corridor, side walls, doors, ceiling, and floor can generate a lot of reflections in a wide spatial range. These paths are delayed and weak. However, distant scatterers tend to generate reflections within a narrow spatial range. The effect of distant scatterers was established to be at the spatial range of  $-30^\circ$  to  $30^\circ$ . On assumption of same number of local and distant scatterers and each generating same number of MPCs, there would be a higher density on one direction and lower on the other. This gives a distribution similar to the Laplacian distribution with high density at the center and lower density on the side spatial areas.

## 5. Validation of the Proposed Channel Model

To validate the proposed pdf estimation of the indoor corridor channel at 14 GHz, 18 GHz, and 22 GHz frequency bands, the channel parameters are compared with S-V model. The estimated model and the S-V model channel parameters are listed in Table 1. The building used in [6] to conduct measurements is almost similar to our measurement environment. We extracted the model parameters based on LOS scenarios for all the frequency bands. The temporal parameters are estimated using the methods in [6] and are generally larger than the S-V model parameters. The greatest discrepancy is in the estimates for the value of  $\Lambda$  because more clusters were observed (3-5 clusters) in the indoor corridor as compared to 1-2 in [6]. This was due to the structural design, construction materials, and general geometry of the corridor. In addition, the frequency bands considered were much higher than that in S-V model. We were able to identify the clusters that overlap in time but separate in spatial domain. This clearly separated clusters that would have been identified as a single group in time domain only. The S-V model has no spatial parameters values. Both  $\Gamma$  and  $\gamma$  were observed to be fairly similar to S-V model for 18 GHz and slightly higher for other frequency bands.

## 6. Conclusion

The spatiotemporal characteristics of the channel were captured and this information was used for MPCs clustering using a 2-D Gaussian KDE technique. In addition, the inter-cluster and intracluster parameters were extracted and the correlation between time and angular domains in clustering was determined using the proposed channel model. For 14 GHz, three clusters were observed, with the main cluster being between  $-30^\circ$  and  $30^\circ$ . The clusters emerging at the tails of the distributions were as a result of the corridor end wall reflections especially for 14 GHz and 22 GHz bands. The 18 GHz band has a smoother tail because of weak MPCs received from the end and side walls. The clusters' distributions were modeled based on the spatial domain irrespective of time of arrival with variation in mean angle for all the measurements. Rays with short delays made up the clusters between  $-90^\circ$  and  $90^\circ$  for all the frequency bands. The MPCs' distribution within a cluster was approximated with a Laplacian pdf, with standard deviation from  $3.0^\circ$  to  $3.3^\circ$  for the three studied frequency bands.

TABLE 1: Intercluster and intracluster channel parameters for LOS 14 GHz, 18 GHz, and 22 GHz frequency bands.

Parameter	Notation	Units	14 GHz	18 GHz	22 GHz	S-V Model
Cluster rate of arrival	$\Lambda$	[1/ns]	0.05	0.04	0.05	0.003
Ray rate of arrival	$\lambda$	[1/ns]	0.2	0.5	0.2	0.2
Cluster rate of decay	$\Gamma$	[ns]	90	60	90	60
Ray rate of decay	$\gamma$	[ns]	38	25	35	20
Cluster AoA mean	$\Omega_m$	[deg]	0	5	0	-
Cluster st. dev.	$\sigma_{\Omega_m}$	[deg]	25	25	22	-
Ray AoA mean	$\phi$	[deg]	1.0	1.0	1.0	-
Ray st. dev.	$\sigma_\phi$	[deg]	3.2	3.3	3.0	-

The application of the presented model in indoor corridor and enclosed environments with Tx antenna fixed at height  $h_t$  and typical Rx antenna at height  $h_r$  is described. For any arbitrary distance between the Tx and the Rx antennas, the channel can be easily simulated based on the parameters given in Table 1. The channel can be realized by simulating the MPCs as a Laplacian distribution, then the clusters of the MPCs can be determined as a Gaussian distribution. The simulated channel can be effectively applied in design and deployment of signal processing techniques, network protocols, and massive MIMO for indoor and enclosed environments.

The novelty of this work is the introduction of joint pdf estimates that describe the stochastic properties of the channel with channel parameters conditioned on the spatial domain. Furthermore, it describes the correlation of the intercluster and intracluster spatiotemporal characteristics of the channel. The extracted channel parameters enable reproduction of the channel by computer simulation. The result of this work is applicable in any indoor corridor or enclosed environments with a waveguide-like structural design and concrete and wooden (doors) materials on walls, e.g., pedestrian underpass, tunnels connecting buildings, underground passageways, and through-pass corridors in malls. The corridor can have any cross sectional dimension and length.

## Data Availability

The data used to support the findings of this study are available from the corresponding author upon request.

## Conflicts of Interest

The authors declare that they have no conflicts of interest.

## References

- [1] M. Nasr-Esfahani and B. S. Ghahfarokhi, "Improving spectrum efficiency in self-organized femtocells using learning automata and fractional frequency reuse," *Annals of Telecommunications-Annales des Télécommunications*, vol. 72, no. 11-12, pp. 639–651, 2017.
- [2] S. Sivakrishna and R. S. Yarrabothu, "Design and simulation of 5G massive MIMO kernel algorithm on SIMD vector processor," in *Proceedings of the Conference on Signal Processing and Communication Engineering Systems (SPACES '18)*, pp. 53–57, Vijayawada, India, January 2018.
- [3] C.-C. Chong, C.-M. Tan, D. I. Laurenson, S. McLaughlin, M. A. Beach, and A. R. Nix, "A new statistical wideband spatio-temporal channel model for 5-GHz band WLAN systems," *IEEE Journal on Selected Areas in Communications*, vol. 21, no. 2, pp. 139–150, 2003.
- [4] R. B. Ertel, P. Cardieri, K. W. Sowerby, T. S. Rappaport, and J. H. Reed, "Overview of spatial channel models for antenna array communication systems," *IEEE Personal Communications*, vol. 5, no. 1, pp. 10–22, 1998.
- [5] U. Martin et al., "Model scenarios for direction-selective adaptive antennas in cellular mobile communication systems – scanning the literature," *Wireless Personal Communications*, vol. 11, no. 1, pp. 109–129, 1999.
- [6] A. A. Saleh and R. A. Valenzuela, "A statistical model for indoor multipath propagation," *IEEE Journal on Selected Areas in Communications*, vol. 5, no. 2, pp. 128–137, 1987.
- [7] A. Meijerink and A. F. Molisch, "On the physical interpretation of the Saleh-Valenzuela model and the definition of its power delay profiles," *IEEE Transactions on Antennas and Propagation*, vol. 62, no. 9, pp. 4780–4793, 2014.
- [8] A. F. Molisch, D. Cassioli, and C.-C. Chong, "A comprehensive standardized model for ultrawideband propagation channels," *IEEE Transactions on Antennas and Propagation*, vol. 54, no. 11, pp. 3151–3166, 2006.
- [9] A. F. Molisch et al., "IEEE 802.15.4a channel model," *Final Report*, 2004.
- [10] Q. H. Spencer, B. D. Jeffs, M. A. Jensen, and A. L. Swindlehurst, "Modeling the statistical time and angle of arrival characteristics of an indoor multipath channel," *IEEE Journal on Selected Areas in Communications*, vol. 18, no. 3, pp. 347–360, 2000.
- [11] R. Heddergott, U. Bernhard, and B. Fleury, "Stochastic radio channel model for advanced indoor mobile communication systems," in *Proceedings of the 8th International Symposium on Personal, Indoor and Mobile Radio Communications (PIMRC '97)*, vol. 1, pp. 140–144, Helsinki, Finland, 1997.
- [12] C. Gustafson, K. Haneda, S. Wyne, and F. Tufvesson, "On mm-wave multipath clustering and channel modeling," *IEEE Transactions on Antennas and Propagation*, vol. 62, no. 3, pp. 1445–1455, 2014.

- [13] X. Wu, C.-X. Wang, J. Sun et al., "60-GHz millimeter-wave channel measurements and modeling for indoor office environments," *IEEE Transactions on Antennas and Propagation*, vol. 65, no. 4, pp. 1912–1924, 2017.
- [14] B. Ai et al., "On indoor millimeter wave massive MIMO channels: measurement and simulation," *IEEE Journal on Selected Areas in Communications*, vol. 35, no. 7, pp. 1678–1690, 2017.
- [15] J. Huang, C.-X. Wang, R. Feng, J. Sun, W. Zhang, and Y. Yang, "Multi-Frequency mmWave Massive MIMO Channel Measurements and Characterization for 5G Wireless Communication Systems," *IEEE Journal on Selected Areas in Communications*, vol. 35, no. 7, pp. 1591–1605, 2017.
- [16] Q. Wang, B. Ai, D. W. Matolak et al., "Spatial variation analysis for measured indoor massive MIMO channels," *IEEE Access*, vol. 5, pp. 20828–20840, 2017.
- [17] C. Xu, J. Zhang, Q. Zheng, H. Yu, and L. Tian, "Measurement-based delay spread analysis of wideband massive MIMO system at 3.5 GHz," in *Proceedings of the IEEE International Conference on Computational Electromagnetics (ICCEM '17)*, pp. 246–248, Kumamoto, Japan, March 2017.
- [18] J. Li, B. Ai, R. He et al., "Measurement-based characterizations of indoor massive MIMO channels at 2 GHz, 4 GHz, and 6 GHz frequency bands," in *Proceedings of the IEEE 83rd Vehicular Technology Conference (VTC Spring '16)*, pp. 1–5, Nanjing, China, May 2016.
- [19] N. Czink, M. Herdin, H. Özcelik, and E. Bonek, "Number of multipath clusters in indoor MIMO propagation environments," *IEEE Electronics Letters*, vol. 40, no. 23, pp. 1498–1499, 2004.
- [20] N. O. Oyie and T. J. O. Afullo, "Measurements and analysis of large-scale path loss model at 14 and 22 GHz in indoor corridor," *IEEE Access*, vol. 6, pp. 17205–17214, 2018.
- [21] M. Toeltsch, J. Laurila, K. Kalliola, A. F. Molisch, P. Vainikainen, and E. Bonek Sr., "Statistical characterization of urban spatial radio channels," *IEEE Journal on Selected Areas in Communications*, vol. 20, no. 3, pp. 539–549, 2002.
- [22] J. E. Dietert and B. Rembold, "Stochastic channel model for outdoor applications based on raytrace simulations," in *Proceedings of the Millennium Conference on Antennas and Propagation (AP '20)*, Davos, Switzerland, April 2000.
- [23] M. Steinbauer, A. F. Molisch, and E. Bonek, "The double-directional radio channel," *IEEE Antennas and Propagation Magazine*, vol. 43, no. 4, pp. 51–63, 2001.
- [24] K. J. Kim, J. Yue, R. A. Iltis, and J. D. Gibson, "A QRD-M/Kalman filter-based detection and channel estimation algorithm for MIMO-OFDM systems," *IEEE Transactions on Wireless Communications*, vol. 4, no. 2, pp. 710–721, 2005.
- [25] K. Dasani and A. Shrotriya, "Channel estimation and data detection with fuzzy C-means based em approach in MIMO system," in *Proceedings of the 2nd International Conference on Computational Intelligence and Communication Technology (CICT '16)*, pp. 559–563, February 2016.
- [26] W. N. Venables and B. D. Ripley, *Modern Applied Statistics with S-PLUS*, Springer Science & Business Media, New York, NY, USA, 4th edition, 2013.
- [27] C. Heinz and B. Seeger, "Cluster kernels: Resource-aware kernel density estimators over streaming data," *IEEE Transactions on Knowledge and Data Engineering*, vol. 20, no. 7, pp. 880–893, 2008.
- [28] L. C. Matioli, S. R. Santos, M. Kleina, and E. A. Leite, "A new algorithm for clustering based on kernel density estimation," *Journal of Applied Statistics*, vol. 45, no. 2, pp. 347–366, 2018.
- [29] D. W. Scott, *Multivariate Density Estimation: Theory, Practice and Visualization*, John Wiley & Sons, New York, NY, USA, 1992.
- [30] A. Maltsev, R. Maslennikov, A. Lomayev, A. Sevastyanov, and A. Khoryaev, "Statistical channel model for 60 GHz WLAN systems in conference room environment," *Radioengineering*, vol. 20, no. 2, pp. 409–422, 2011.
- [31] P. F. M. Smulders and A. G. Wagemans, "A statistical model for the MM-wave indoor radio channel," in *Proceedings of the 3rd IEEE International Symposium on Personal, Indoor and Mobile Radio Communications*, pp. 303–307, Boston, MA, USA, 1992.

## Research Article

# Development and Validation of New Reverberation Chamber for Wireless Devices

Dong-Uk Sim <sup>1</sup>, Sang Il Kwak,<sup>1</sup> Jong Hwa Kwon,<sup>1</sup> and Seong-Ook Park<sup>2</sup>

<sup>1</sup>Radio Environment and Monitoring Research Group, Electronics and Telecommunications Research Institute (ETRI), Daejeon 34129, Republic of Korea

<sup>2</sup>School of Electrical Engineering, Korea Advanced Institute of Science and Technology (KAIST), Daejeon 34141, Republic of Korea

Correspondence should be addressed to Dong-Uk Sim; [simdonguk@etri.re.kr](mailto:simdonguk@etri.re.kr)

Received 19 April 2018; Accepted 23 May 2018; Published 26 June 2018

Academic Editor: Haejoon Jung

Copyright © 2018 Dong-Uk Sim et al. This is an open access article distributed under the Creative Commons Attribution License, which permits unrestricted use, distribution, and reproduction in any medium, provided the original work is properly cited.

This paper proposes a reverberation chamber structure consisting of new reflectors and mode stirrers for electromagnetic compatibility and wireless terminal measurements. The key design considerations for them are determined through a reasonable approach to analyze the eigenmode for a reverberation chamber and the standard deviation of its working volume based on 3D simulation. The final designs are expected to improve the standard deviation performance of the initial structure of the reverberation chamber and provide a better mode stirring environment. The results measured in the fabricated chamber demonstrate that these predictions are clearly realized. The results satisfy the main requirements of this paper, which are defined in consideration of the specifications of commercial reverberation chamber products. Therefore, the reverberation chamber of this paper is expected to be useful for performance measurement and evaluation of commercial wireless terminals. To verify this logical approach to obtain a good design and its results, the results measured in the actual fabricated reverberation chamber are described along with analytical and computational results.

## 1. Introduction

Unlike previous generations, 5G network is characterized by the provision of innovative services rather than technological advances [1]. ITU-R proposed the service scenarios for 5G such as augmented reality (AR), self-driving car, and smart city cameras, which are defined as a combination of the following three core scenarios: enhanced mobile broadband (eMBB), ultra-high reliable and low latency communications (URLLC), and massive machine type communication (mMTC) [2]. The innovative services impose very challenging requirements on 5G network, such as the 1000 times higher data rate and 100 times reduced latency, which are impossible to meet with a single technology. Therefore, a wide variety of devices equipped with suitable technologies for each service will comprise the 5G network. For the wide variety of devices, providing a single measurement instrument such as an anechoic chamber (AC) or a reverberation chamber (RC) is one of the important issues to reduce capital and operational expenses (CAPEX/OPEX).

The AC has been considered the only way to measure the 5G devices. However, to overcome drawbacks of AC as well as considering the real communication environment, recently the RC attracts a huge attention. The RC is an important alternative measurement instrument for the measurement and application of small antennas for wireless and mobile terminals and for realistic evaluation of SISO to MIMO devices below the current 4G standard, as is well known through the IEC 61000-4-21 standard [3–5]. It can be used for obtaining various metrics between traditional antennas and devices such as efficiency, correlation, total radiated power (TRP), and total isotropic sensitivity (TIS) with high accuracy and short measurement times. Currently, the widespread use of this RC technology provides a variety of methodologies to support testing of the key performance indicators for 5G devices. However, achieving this requires the design of RC that has a more stringent field uniformity performance than the standard, which is for electromagnetic compatibility (EMC), not for 5G services. This is because, at higher frequencies in the millimeter wave band that will be a key component

for enabling a massive increase of the available bandwidth and high data rates, the measurement uncertainty may have a profound effect on the actual performance evaluation of 5G devices. Thus, more stringent user requirements for an RC must be defined, and a reasonable design approach is required to achieve them.

The most important consideration for the intended measurement tasks and applications in these fields is to design an RC appropriately so that it satisfies the user's requirements. The standard provides requirements of acceptable RC performance and basic guidelines for RC design to meet these requirements. Indeed, there are no indicators to objectively evaluate RC performance beyond the requirements of the standard in modeling for RC construction. Also, even if an RC is designed much more stringently than the requirements proposed in the standard, this does not prove that it can achieve superior performance in comparison to other RCs. In other words, comparing the performance of different RCs, including their physical parameters, can be quite difficult, and there are no theoretically standardized formats or guidelines on how to carry out RC modeling to achieve better performance.

In this respect, it can be said that the design of an RC with excellent performance is virtually impossible without an initial reference structure. Based on an initial structure that satisfies the basic standard guidelines, the specific design of an RC should follow a reasonable structure design process to modify it until the user's own requirements are satisfied. The derivation of this initial structure and the logical process for its improvement are dependent on known rules of thumb or unknown rules of thumb [6, 7]. It is well known that a deterministic approach based on the numerical method is accurate in modeling an RC including mode stirrers for desired RC performance [8]. Based on this approach and the rules of thumb, the RC design method based on 3D electromagnetic wave (EM) simulations provides valuable insight into the physical working principles of an RC; allows the design behaviours for the geometrical parameters, such as mode stirrer size, shape, and position to be determined; and finally shortens the development time until the RC meets all the requirements of the user [9]. We can refer to other RC structures introduced in other papers for purposes different from this study, which include several types of mode stirrers [10–12].

This paper proposes a new RC structure for EMC and wireless device measurements. As mentioned above, the requirements for an RC have been established and its initial structure has been determined through the references and the rules of thumb. Based on the initial structure, a reasonable approach using field uniformity and eigenmode analysis in the RC has resulted in the final structure that satisfies the requirements and shows improved performance compared to the initial one. Another objective of this paper is to show that this approach for superior design will improve the previous results in a way that compares relatively well with the current theoretical results. To verify the performance of the final structure, experimental results of the constructed prototype are presented along with simulation results.

TABLE 1: Requirements of reverberation chamber to develop.

Items	Requirements
Start operating frequency	650 MHz
Overall volume	5.05 m <sup>3</sup>
(Internal dimensions)	(1.4 m × 1.95 m × 1.85 m)
Working volume	0.76 m <sup>3</sup>
(Rectangular dimensions)	(0.835 m × 0.951 m × 0.954 m)
Standard deviation	Less than 2.5 dB

## 2. Reverberation Chamber Requirements

Considering the requirements of the IEC 61000-4-21 standard, the requirements of RC to be developed in this work are shown in Table 1. For measurements at mobile communication frequencies and for EMC measurements above 1 GHz, the start operating frequency of the RC was set to 650 MHz [13, 14]. The RC has inner dimensions of 1.4 m × 1.95 m × 1.85 m (length  $L$  × width  $W$  × height  $H$ ) based on the size of the Bluetest RTS60 model, having outside dimensions of 1.4 m × 1.94 m × 2 m [15].

The working volume of the RC can be located at a distance greater than  $\lambda/4$  from the wall, mode stirrers, and reflectors within the RC [3], where  $\lambda$  is the wavelength for the start operating frequency of the RC. If the distance from them is selected as  $\lambda/4$ , the working volume will be the maximum size. If the requirement for field uniformity is met, the larger the working volume, the better the usability. However, in the process of designing an RC to meet the user's requirements after they are defined by the procedure introduced in this paper, there can be a risk that the mode stirrer or reflector structures satisfying the field uniformity condition may not be derived when the maximum working volume is defined. Moreover, there is also the drawback that it can take a long time to find the structures. Therefore, the working volume should be set appropriately considering the size of the device under test (DUT) as well as the position and distance from the mode stirrers and reflectors.

To do this, commercial RCs (whose overall size and the working volume dimensions are published) were investigated, and the ratio between them was analyzed. This is not based on theoretical grounds, but only to figure out the average level of the ratio from those designed cases. In the case of Siepel models, EOLE80, EOLE200, EOLE400, and EOLE1000 models, the ratios were approximately 10%, 17%, 19%, and 16%, respectively [16]. In this case, the field uniformity specification applied is 3 dB. Considering these data and the standard deviation requirement of this study, the ratio was set to approximately 15%, and the corresponding working volume dimensions were determined as 0.835 m × 0.951 m × 0.954 m (length  $W_L$  × width  $W_W$  × height  $W_H$ ), as shown in Table 1. The general standard deviation, a field uniformity requirement of the IEC 61000-4-21 standard, is 3 dB, but in this study it was set to a more stringent value of 2.5 dB.

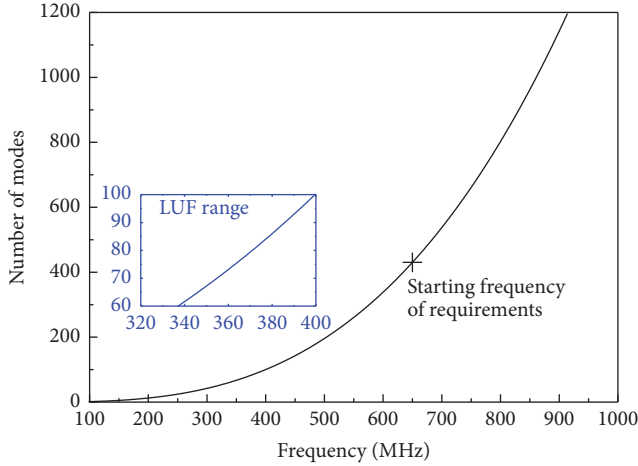


FIGURE 1: Theoretical number of modes for a reverberation chamber of the size considered in this paper.

The number of modes  $N$  computed approximately above cutoff in an ideal empty cavity is given by

$$N = \frac{8\pi}{3} (L \times W \times H) \frac{f^3}{c_0^3}, \quad (1)$$

where  $f$  is the frequency in hertz and  $c_0$  is the vacuum speed of light in meters per second [17]. For the overall size of the RC in Table 1, the modal numbers present in the cavity with respect to the frequency are shown in Figure 1. The “60 to 100 modes” rule suggests that the lowest useable frequency (LUF) exists in the range of approximately 338 MHz to 400 MHz [3, 18]. For the purpose of this work, 650 MHz, at which many more modes are generated than at the theoretical LUF, is considered as the start operating frequency of RC, that is, the actual LUF. Therefore, the RC performance was considered starting from 650 MHz during the development process and verification.

### 3. Reverberation Chamber Design and Simulation

**3.1. The Basic Prototype of Reverberation Chamber.** The basic prototype of the RC that reflects the dimension requirements in Table 1 is shown in Figure 2. It is a rectangular chamber consisting of two mode stirrers, herein referred to as stirrer 1 and stirrer 2. Stirrer 1 is perpendicular to the bottom of the chamber and consists of four rectangular planes with a width ( $a$ ) of 0.46 m and a height ( $b$ ) of 0.46 m, which correspond to the size of one wavelength for an operating frequency of 650 MHz. For asymmetric placement between all planes, these planes have been rotated  $45^\circ$  around rotation axes with the directions of  $(\vec{x} + \vec{y} + \vec{z})$ ,  $(\vec{x} - \vec{y} + \vec{z})$ ,  $(-\vec{x} - \vec{y} - \vec{z})$ , and  $(-\vec{x} + \vec{y} + \vec{z})$  at each of their centers in order from the plane nearest to the bottom.

Stirrer 2 is horizontal to the bottom of the chamber and consists of four rectangular planes. Taking into account operation at the higher frequency and the asymmetry of stirrer 1, each plane has a width ( $c$ ) of 0.4 m and a height ( $d$ ) of

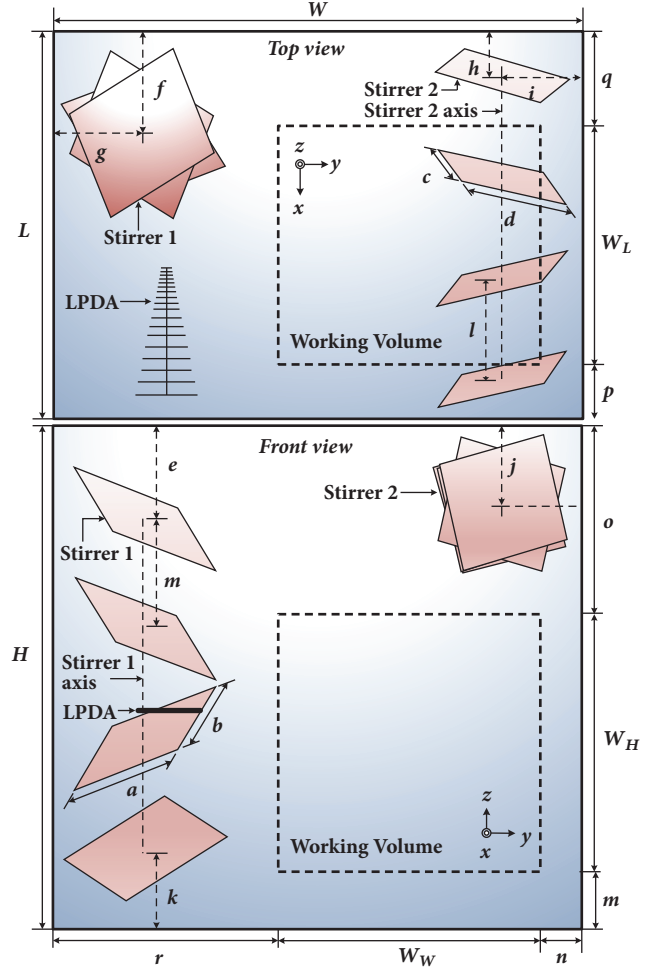


FIGURE 2: Basic prototype of a reverberation chamber proposed in this paper.

0.4 m, which are slightly less than one wavelength. Similarly, these planes have also been rotated  $25^\circ$  around rotation axes with the same vector directions as in the case of stirrer 1 at each of their centers in order from the bottom plane in the top view of Figure 2. The working volume defined in Table 1 is located 0.157 m from stirrer 1 and 0.12 m from stirrer 2. These are spaced distances greater than 0.115 m, which is a quarter wavelength for an operating frequency of 650 MHz [3]. Likewise, the separation distances from the RC walls, denoted by  $m$ ,  $n$ ,  $p$ , and  $q$ , were determined to be more than a quarter wavelength and satisfy the working volume requirement of Table 1. The values of all parameters depicted in Figure 2 are shown in Table 2.

To investigate the level of field uniformity of the basic prototype as described in Introduction, a commercial software package FEKO as the simulation kernel, which is based on a frequency domain method of moment (MOM), is used [19]. Because it provides ease of modeling large 3D structures, such as an RC, as well as its numerical accuracy, it was chosen for this study. The algorithms and the usability of the software can be confirmed through several published studies that have used them in analyzing RCs [8–10], although those studies

TABLE 2: Design parameters for the basic prototype of the reverberation chamber.

Parameter	Length, m	Parameter	Length, m
$H$	1.85	$g$	0.34
$L$	1.4	$h$	0.16
$W$	1.95	$i$	0.31
$W_H$	0.954	$j$	0.3
$W_L$	0.835	$k$	0.3
$W_W$	0.951	$l$	0.36
$a$	0.46	$m$	0.2
$b$	0.46	$n$	0.2
$c$	0.4	$o$	0.7
$d$	0.4	$p$	0.2
$e$	0.35	$q$	0.364
$f$	0.36	$r$	0.8

may have had purposes different from that of the present study.

For the simulation of the materials in the closed structure, a free space condition with a relative permittivity of  $\epsilon_r = 1$  and a relative magnetic permeability of  $\mu_r = 1$ , which were assumed to be frequency independent, was used. For the zinc plates of the RC walls and the aluminum plates of mode stirrers with a thickness of 0.002 m, the values of  $\sigma = 1.67 \times 10^7$  S/m and  $\sigma = 3.816 \times 10^7$  S/m, respectively, were used. These values were also assumed to be frequency independent. The processor and memory used for the simulations were an Intel(R) Xeon(R) CPU E5-2699 v4 and a memory (RAM) of 256 GB, respectively.

The simulations were performed at a total of nine frequencies at 25 MHz intervals from 650 MHz to 850 MHz. The reason is that for 850 MHz and above, the mesh size generated in the RC requires much more resources to compute. A log-periodic dipole array (LPDA) antenna was used as a transmitting antenna for the simulations. It consisted of 18 dipole elements, and it was realized by impedance matching through the transmission line network. At each calculation frequency, a total of twenty simulations were performed as the stirrers rotated at  $18^\circ$  intervals. Then, the standard deviation representing the field uniformity of the RC was computed according to the IEC 61000-4-21 standard after postprocessing collecting the electric field data from twenty simulations.

The results are shown in Figure 3. These results show that the basic prototype of the RC, which reflects the physical requirements in Table 1, exhibits a standard deviation characteristic of less than 3 dB at most frequencies. These simulations were not intended to calculate accurate standard deviation values, but rather to investigate the tendency of their change and their approximate level in the frequency band of interest. In actual measurements, it was expected that a lower standard deviation could be obtained because the reverberation effect occurs constantly, while the stirrers rotate at regular intervals. Based on the basic structure, the following subsections describe its performance improvement process and the corresponding results to meet the performance requirements of Table 1.

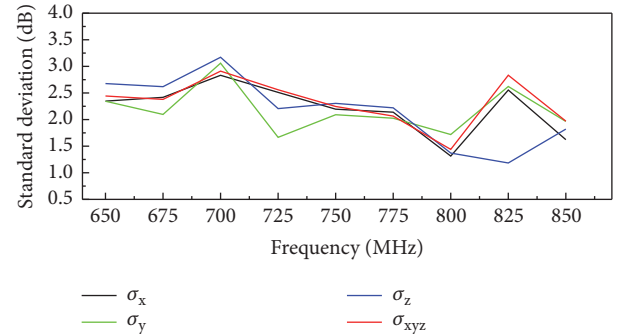


FIGURE 3: The simulated E-field standard deviation for working volume of the basic RC structure.

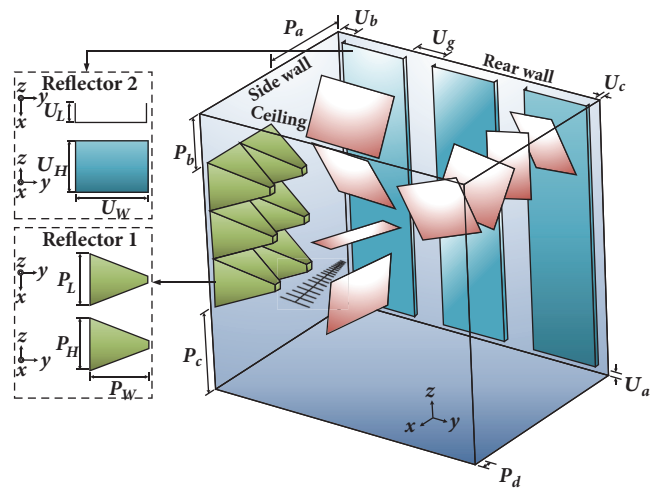


FIGURE 4: RC structure with reflector 1 and 2.

**3.2. The Effect of Reflectors in a Reverberation Chamber.** The approach to improve the field uniformity of an RC can be roughly divided into two main aspects. One of them is to implement the appropriate reflectors by effectively utilizing the empty spaces on the RC walls. The other is to design efficient mode stirrers. This part describes the results for the former. As shown in Figure 2, due to the mode stirrers and the working volume, the available wall space is limited to the space on the walls forming the edges under stirrer 1 in the top view and the ceiling space between stirrer 1 and stirrer 2 in the front view.

The reflector structures and their positions applied to these spaces are shown in Figure 4. The structure of reflector type 1 is derived from the shape of a pyramidal absorber in a typical anechoic chamber. Taking into account the space required to place multiple reflectors and space to place the transmitting antenna, reflector type 1 has dimensions of  $0.324 \text{ m} \times 0.36 \text{ m} \times 0.324 \text{ m}$ . In addition, their final positions were determined through a parametric study analyzing the field uniformity according to those numbers.

Figure 5 shows the variation of standard deviation according to the number of type 1 reflectors. These results were calculated by placing them in order from the bottom of the left sidewall to the top, in the top of the middle of the



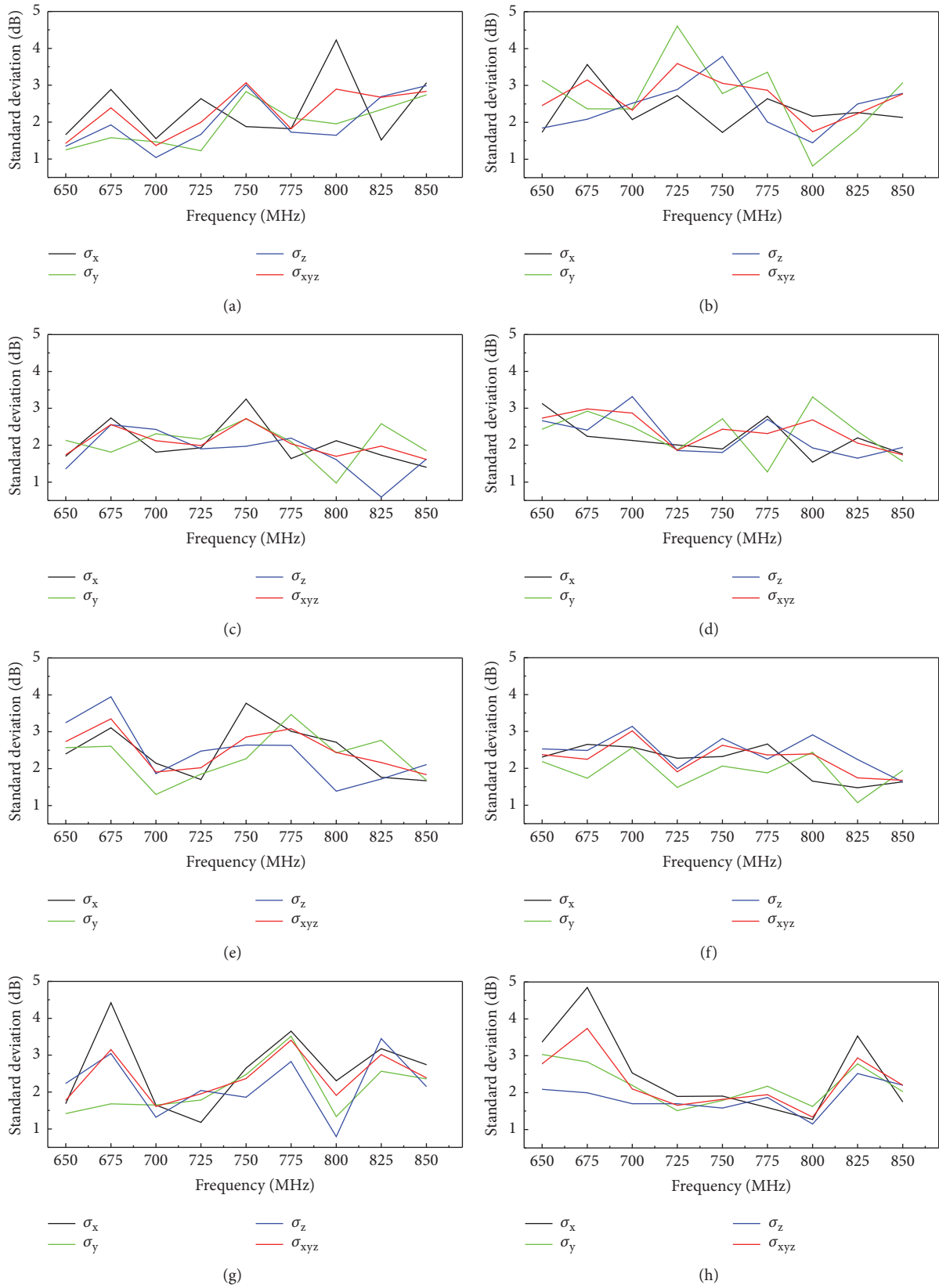


FIGURE 5: Standard deviation calculated according to the number of reflector 1 when there is no reflector 2. (a) 2. (b) 4. (c) 6. (d) 8. (e) 10. (f) 11. (g) 13. and(h) 16.

TABLE 3: Design parameters related to the reflectors within the reverberation chamber.

Parameter	Length, m	Parameter	Length, m
$P_H$	0.324	$U_H$	1.75
$P_L$	0.324	$U_L$	0.03
$P_W$	0.36	$U_W$	0.461
$P_a$	0.71	$U_a$	0.05
$P_b$	0.34	$U_b$	0.05
$P_c$	0.538	$U_c$	0.05
$P_d$	0.042	$U_g$	0.22

rear wall, and in the space between stirrers 1 and 2 on the ceiling in the absence of type 2 reflectors in Figure 4. For the simulations, various numbers of type 1 reflectors were located in the RC that is eight, two, and six, respectively, and a total of sixteen simulation results were obtained. The numbers in the upper right corner of the graphs in Figure 5 indicate the number of type 1 reflectors applied.

The results indicates that when six type 1 reflectors are located on the left wall as shown in Figure 5(c), an acceptable standard deviation is obtained in the frequency band of interest. Here, when the number of type 1 reflectors is fixed to six, the standard deviation is recalculated according to the numbers of reflectors placed on the rear wall and the ceiling. The results were found to be similar or worse than that obtained with six type 1 reflectors. Therefore, it can be said that the number of type 1 reflectors should be six in consideration of convenience and cost in the fabrication of an RC. The final design parameter values for reflector 1 are shown in Table 3.

Placing reflector 2 shown in Figure 4 on the rear wall of the RC makes part of the wall uneven; thus, we can expect the generation of hybrid modes that can contribute to making the field evenly distributed in the RC. This expectation is based on the acoustical theory that the acoustical quality of a room can be improved by using scattering elements [20]. However, the structure of reflector 2 proposed in this paper, which are different from the scattering elements, was chosen as a thin plate attached to the chamber wall with a thin air gap ( $U_L$ ) between the plate and the wall.

As described above, the standard deviation analysis method of the working volume for evaluating field uniformity is very intuitive, but it does not provide a valuable insight into the physical principles caused by changes in structures, including mode stirrers inside an RC. In addition, the method requires extensive computation time, computational resources, and complex postprocessing. From this point of view, eigenmode analysis is very effective for the design of mode stirrers or reflectors in an RC. According to this technique, the design with the maximum amount of eigenfrequency shifts is the optimal choice, which allows designers to quickly and easily evaluate designs. This was confirmed in [21], which stated that the effectiveness of a mode stirrer lies in its ability to shift eigenfrequencies.

It should be noted that it is very difficult to quantitatively define the correlation between the eigenfrequency shift and

TABLE 4: Dimensions for width and gap of type 2 reflectors for the eigenfrequency shifts analysis according to their number.

Number of Reflector 2	$U_W$ , m	$U_g$ , m	Other Parameters
4	0.24	0.24	Same as Table 3
5	0.24	0.12	
8	0.12	0.12	
9	0.12	0.06	
11	0.06	0.12	
12	0.12	0.03	
21	0.06	0.03	

the standard deviation of the field uniformity. Therefore, the eigenfrequency and standard deviation should be analyzed together based on the reference structure, for example, as shown in Figure 2, to obtain the field uniformity satisfying the user's requirements. The eigenfrequency shifts ( $\Delta f_{\text{eigen}}$ ) are given by

$$\Delta f_{\text{eigen}} = |f_{\text{eigen.empty}} - f_{\text{eigen.loaded}}|, \quad (2)$$

where  $f_{\text{eigen.empty}}$  and  $f_{\text{eigen.loaded}}$  are the eigenfrequencies in an empty cavity and in an RC including each subsequent design in the cavity, respectively. According to (2), all designs presented in this section are evaluated under the same conditions, and the relative performance is compared. The eigenfrequencies are calculated for the actual total volume and internal structures of the RC shown in Figures 2 and 4 by using CST MICROWAVE STUDIO [22]. The material filling the RC is air (free space), and for a numerical analysis the boundary conditions selected on all its walls are  $E = 0$ .

For the calculation of eigenfrequencies according to the number of type 2 reflectors, their width ( $U_W$ ) and spacing ( $U_g$ ) were selected as shown in Table 4. Other parameters were the same as those shown in Tables 2 and 3. This is to investigate the changes in eigenfrequencies within an RC depending on the degree of roughness. The calculated results are shown in Figure 6. No consistent relevance for the changes in  $U_g$  can be found in three pairs of results obtained when the number of type 2 reflectors is 4 and 5, 8 and 9, and 11 and 21. Likewise, the three pairs of results when the number of type 2 reflectors are 5 and 8, 8 and 11, and 12 and 21 do not show any linear relationship for the variation of  $U_W$ . However, it can be seen that the amount of eigenfrequency shifts is larger under conditions where the number of type 2 reflectors is small and their width is large. In particular, it should be noted that the width corresponds to approximately  $\lambda/4$  of the starting operating frequency. From these results, the eigenfrequencies were investigated for several dimensions of  $U_W$  and  $U_g$  when a smaller number of type 2 reflectors were applied, that is, when 2 or 3 reflectors were applied. Those conditions are shown in Table 5.

The numerical results shown in Figures 6(b) and 6(c) show that the conditions of  $U_W = 0.461$  m and  $U_g = 0.22$  m can provide a better environment than other conditions in terms of the mode stirring performance of the RC. In particular, this condition in which the width corresponds to approximately

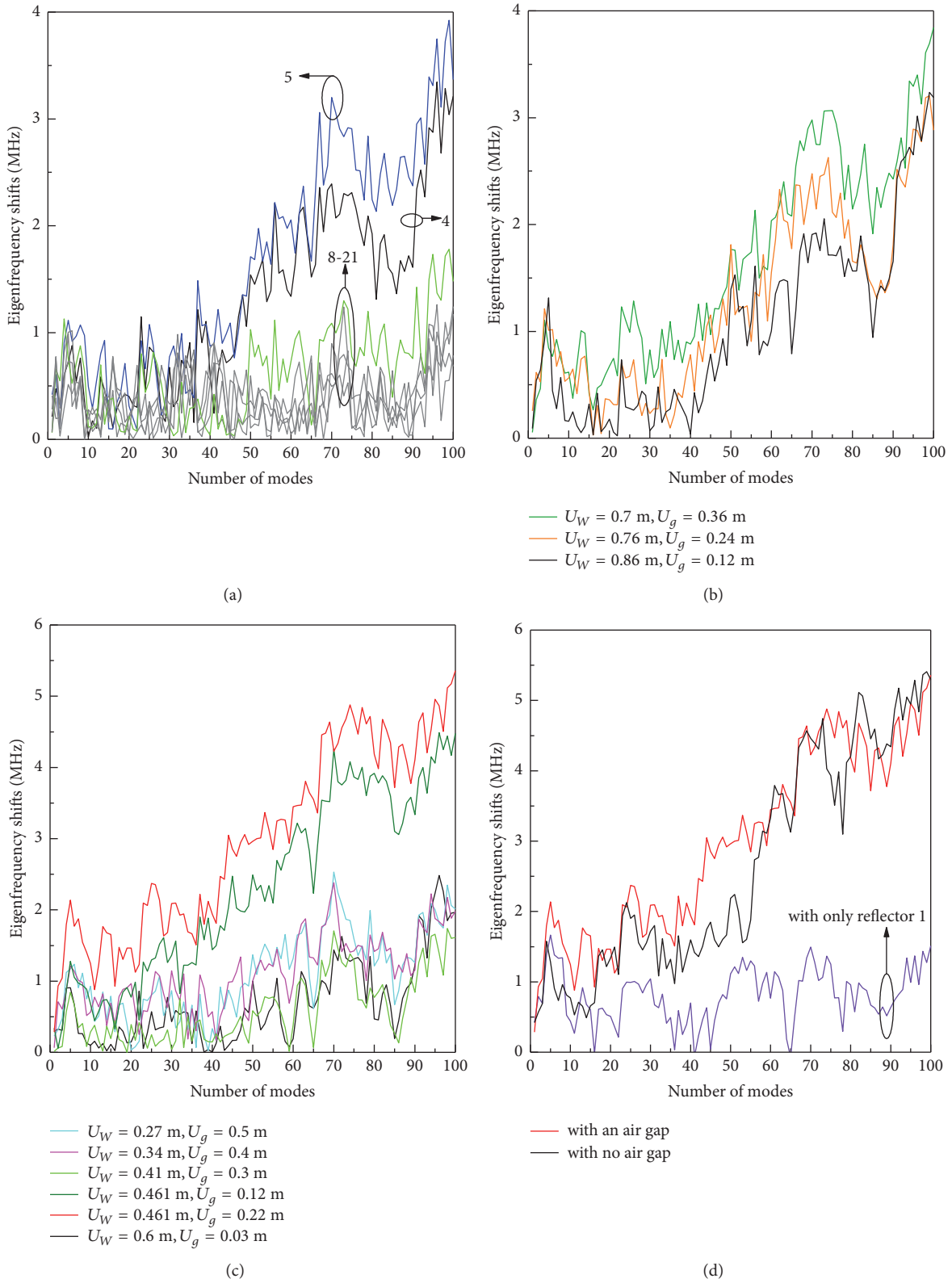


FIGURE 6: Eigenfrequency shifts calculated to determine the dimensions of reflector 2. (a) Results for the conditions in Table 4. (b) Results for two reflectors of the conditions in Table 5. (c) Results for three reflectors in Table 5. (d) Comparison of results for type 2 reflectors with an air gap and with no air gap when  $U_W = 0.461 \text{ m}$  and  $U_g = 0.22 \text{ m}$ .

TABLE 5: Dimensions for width and gap of type 2 reflectors for the eigenfrequency shifts calculations.

Number of Reflector 2	$U_W$ , m	$U_g$ , m	Other Parameters
2	0.7	0.36	Same as Table 3
	0.76	0.24	
	0.86	0.12	
3	0.27	0.5	Same as Table 3
	0.34	0.4	
	0.41	0.3	
	0.461	0.12	
	0.461	0.22	

one wavelength ( $\lambda$ ) shows an improved performance over  $\lambda/2$  and  $3\lambda/2$  conditions of  $U_W = 0.24$  m and  $U_W = 0.7$  m in Figure 6(a), respectively. Figure 6(d) shows that type 2 reflectors with an air gap shown in Figure 4 are superior to type 2 reflectors with no air gap in most modal numbers as well as lower ones and provides evidence that the shape of reflector 2 with the dimensions described above can create a better mode stirring environment than when there is only reflector 1.

**3.3. Mode Stirrer Design and the Final Design Results of RC.** In the RC shown in Figures 2 and 4, it can be inferred that there is a limit to the mode stirrer design to improve the mode stirring performance. First, the method of constructing the additional mode stirrer is difficult to realize spatially because of the working volume already defined and the transmitting antenna. Moreover, it is not efficient in terms of production cost because a separate motor for rotating the mode stirrer must be introduced. An alternative is to directly modify the structures of stirrers 1 and 2. This may have the effect of increasing the electrical length of the stirrer plates by making each square plate of the stirrers asymmetrically irregular. However, the start operating frequency of the RC defined in this paper is 650 MHz, which is much larger than the theoretical LUF, as described in Section 2, and performance improvements at frequencies lower than that are beyond the scope of interest. Even if there is room for improvement beyond the start operating frequency, the ease and cost of fabrication should be considered in reality for more complex structures. It should also be noted that the field uniformity performance at around 650 MHz in the results of number 6 of Figure 5 shows a level that almost satisfies the requirements. Therefore, a relatively simple approach has been adopted in this paper.

Figure 7 shows the final RC structure with the new stirrers 1 and 2 consisting of dual plates. In the case of stirrer 1, the newly added plates are located at the top of each pair. Also, in the case of stirrer 2, the new plates are located closer to the front, including the door, in each pair. The added plates have the same size as the original plates, and they are located at regular intervals denoted by  $g_{s1}$  and  $g_{s2}$  in the direction perpendicular to the plane from the center of the original ones. The performance of eigenfrequency shifts according

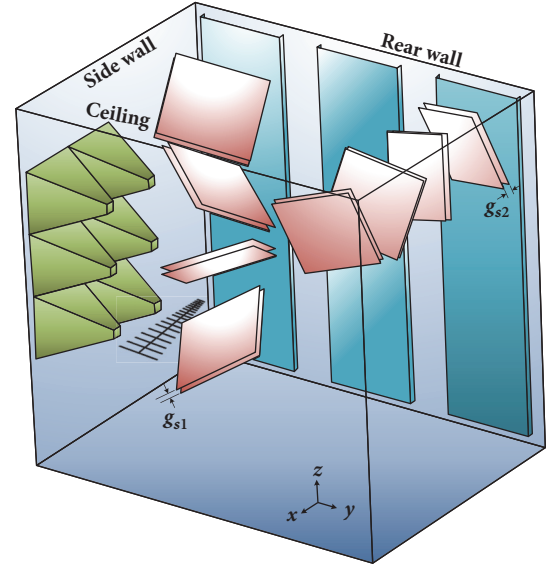


FIGURE 7: Final reverberation chamber structure with dual-plate type mode stirrers for fabrication.

to the intervals,  $g_{s1}$  and  $g_{s2}$ , is investigated as shown in Figure 8. Both graphs consistently show that the smaller the spacing of the plates that make up each stirrer,  $g_{s1}$  and  $g_{s2}$ , the better the eigenfrequency shifts occur. In addition, it has been confirmed again that the condition of  $g_{s1} = g_{s2} = 0.03$  m, which is the minimum dimension for easy fabrication, must be chosen through calculation of the total 16 conditions for the dimensions of the parameters shown in the legend of both graphs.

The eigenfrequency shifts for the final design shown in Figure 7 are shown in Figure 9, along with the results from the previous step. The clear effect of the new stirrers can be seen after the tenth mode number. Also, it can be confirmed that the RC consisting of reflectors and new stirrers can provide a better environment in terms of mode stirring performance. In the proposed RC design, many parameters have not been analyzed. It is almost impossible to find the optimal condition by analyzing the correlations between all these variables, and doing so would have little advantage from the engineering viewpoint. Therefore, in this paper, a basic prototype RC has been derived based on rules of thumb, and methods for improving its performance have been proposed. In addition, by analyzing the key parameters corresponding to the methods through a reasonable approach, the final design that allows the performance of the manufactured RC to meet the requirements has been proposed.

The standard deviations calculated through 3D simulations and postprocessing to confirm the field uniformity performance of the final design are shown in Figure 10 along with the results for the other two conditions shown in Figure 9. The standard deviation results ultimately demonstrate the possibility of improving the mode stirring environment implied by the eigenfrequency shifts shown in Figure 9. In Figure 10(b), the results obtained with the addition of reflector 2 show a standard deviation of less than 3 dB at all analysis

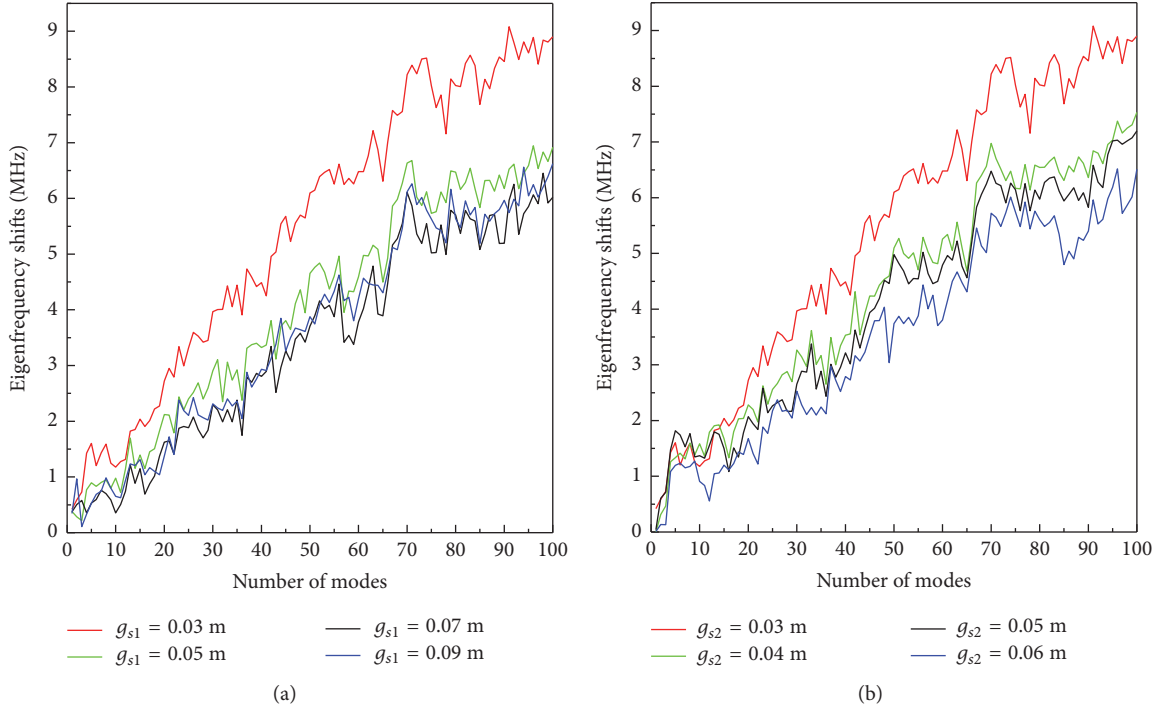


FIGURE 8: Calculated eigenfrequency shifts for RC with stirrers 1 and 2 in dual-plate form (a) when  $g_{s2} = 0.03$  m and (b) when  $g_{s1} = 0.03$  m.

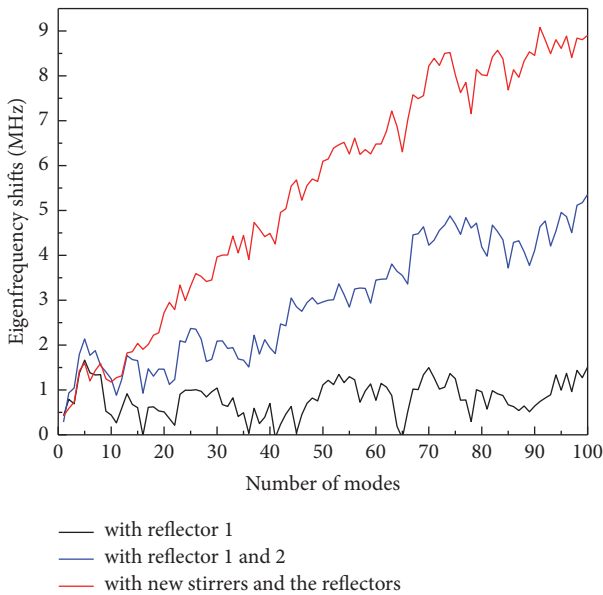


FIGURE 9: Eigenfrequency shifts for the final design compared to those of two other conditions shown in Figure 6(d).

frequencies compared to those in Figure 10(a). The results shown in Figure 10(c), which were obtained from the final design, show that the level of the overall standard deviation is lower in the band above 725 MHz compared to results shown in (c), and the difference between the components at each frequency is reduced. They also show slightly larger standard deviations than 2.5 dB at some frequencies and a maximum

standard deviation of about 2.72 at 725 MHz. However, actual measurements in reverberating environments in which mode stirrers rotate at regular intervals are expected to produce values lower than standard deviations calculated through simulations in which each rotational step is ideally uncorrelated and show a standard deviation of less than 2.5 dB which meets the requirements of this paper.

#### 4. Reverberation Chamber Measurements and Practical Verification

The final design shown in Figure 7 was made according to the dimensions of Tables 2 and 3 and the new stirrers. Figure 11 shows photographs of the fabricated RC, depicting reflector 1, reflector 2, the new stirrers, and the source antenna orientated in the  $x$  direction. Each mode stirrer is rotated by stepper motors controlled by computer software. The LPDA antenna for use as a transmitting antenna is located by a support in the position shown in Figures 2 and 11. The LPDA antenna must operate at 650 MHz or higher and be compact because the space in which it is placed is narrow. However, since the LPDA antenna satisfying these characteristics was not commercially available, one was developed independently. Figure 12 shows a photograph of the developed LPDA antenna. Detailed results for this LPDA antenna are described in [23]. A Rogers RO4003 substrate was used to fabricate the LPDA antenna, and its overall size was  $282 \text{ mm} \times 194 \text{ mm} \times 0.508 \text{ mm}$  ( $L \times W \times H$ ). The fabricated LPDA antenna was measured with a radome as shown in Figure 11. Thus, a compact LPDA antenna has been demonstrated to operate from 0.55 to 9 GHz and to

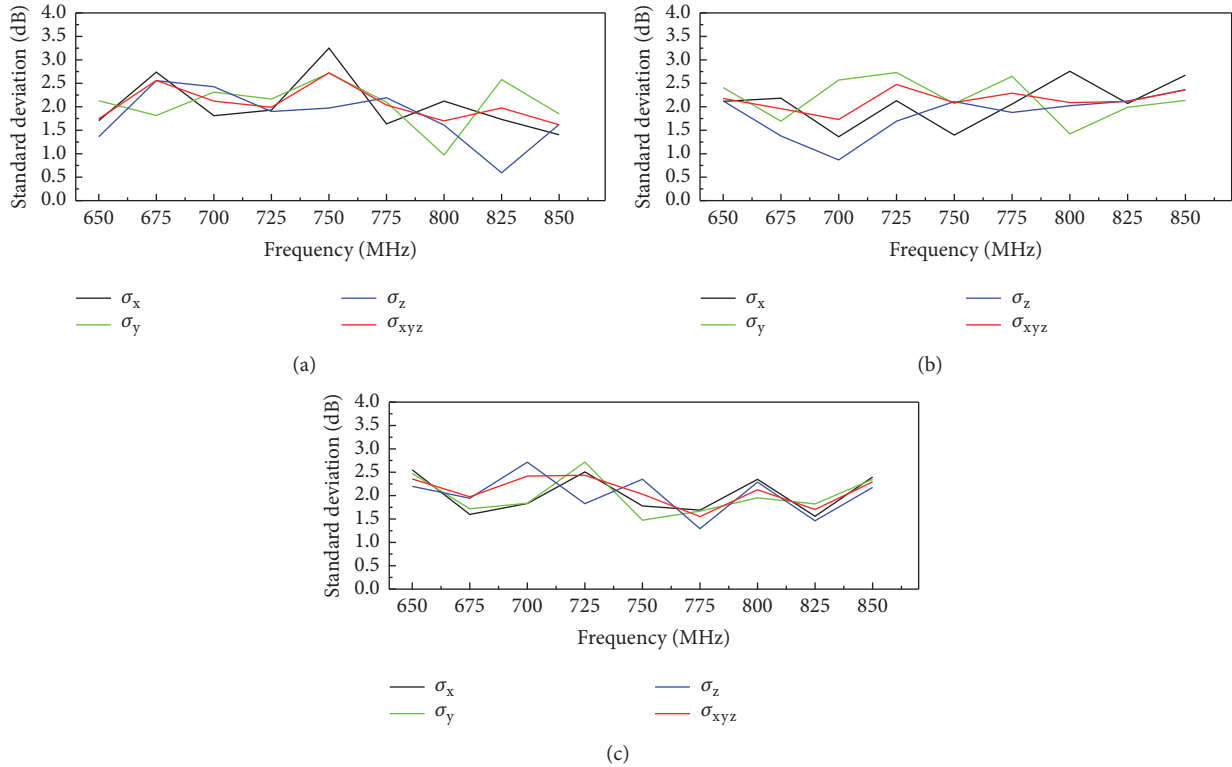


FIGURE 10: Calculated standard deviations for the RC (a) with reflector 1, (b) with reflectors 1 and 2, and (c) with the new stirrers and the reflectors, the final design.



FIGURE 11: Photographs of the fabricated reverberation chamber.

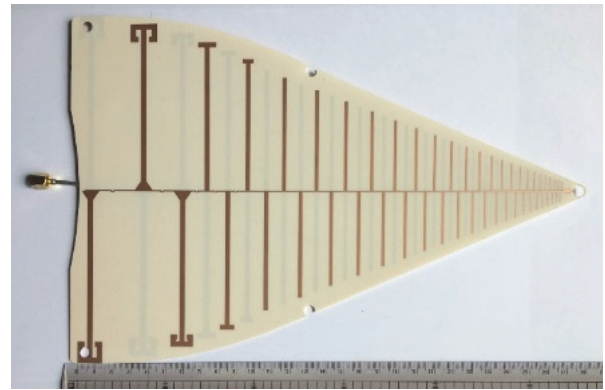


FIGURE 12: Photograph of the LPDA antenna developed to evaluate the performance of the proposed RC.

have a high gain ranging from 2.48 to 7.89 dBi. Compared to the standard LPDA antenna, the size of the proposed antenna has decreased by approximately 27% and 20% in length and width, respectively. Nevertheless, the miniaturized LPDA antenna exhibited broadband characteristics due to top loading techniques.

To evaluate the field uniformity performance of the proposed RC, the maximum electric field values were measured at eight corners of the working volume shown in Figure 2 based on the standard. An electric probe was used to record the field strengths, while the stirrer rotated through 18° angle

steps (i.e., 20 positions for one turn of the stirrer). The standard deviation at each sample frequency was calculated from the raw data of the measured electric field. All measurements and calculations were in accordance with the guidelines proposed in [3].

Figure 13 details the standard deviations measured at the sampling frequencies specified by [3] for the proposed RC and shows its simulated standard deviations according to the design described in Section 3. The tolerance level of field uniformity defined in this paper, which is 2.5 dB, is also shown in the figure. The standard deviations in Figure 13(b)

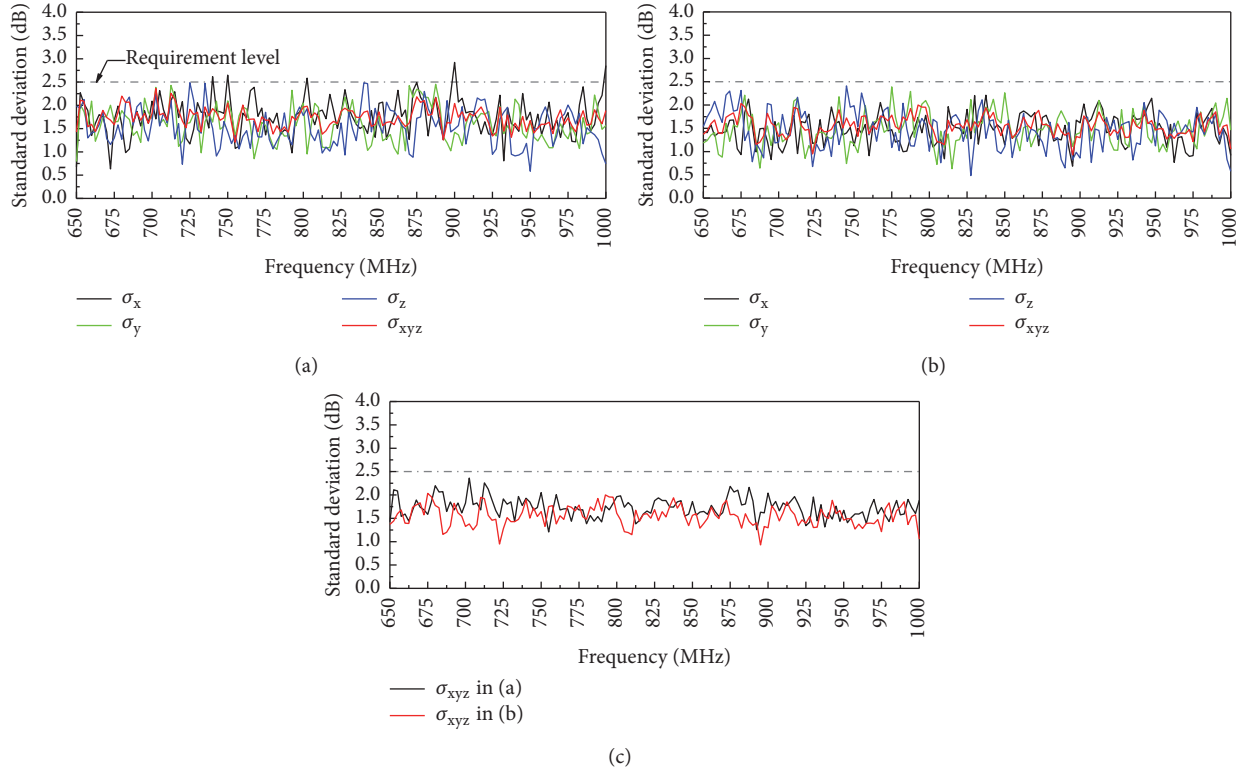


FIGURE 13: Measured standard deviations for the RC (a) with the reflectors and the original stirrers and (b) with the reflectors and the new stirrers, the final design. (c) Comparison between  $\sigma_{xyz}$  components of (a) and (b).

show that the final design consisting of the reflectors and the new dual-plate type stirrers meets the requirements for the field uniformity defined in this paper. It can also be seen that they are lowered at most frequencies compared to the results in Figure 13(a) obtained from a design composed of the reflectors and the original stirrers. This demonstrates that the new stirrer design outperforms the original design. In particular, remarkable frequency bands range from 680 MHz to 752.5 MHz and from 800 MHz to 935 MHz. The standard deviations are reduced by around 0.34 dB and 0.22 dB on average, respectively, and they are improved by up to 1 dB and 0.74 dB, respectively. In addition, the performance of the two stirrers is comparable at some frequencies. Based on these results, it can be concluded that the effective approach of this paper and the proposed final RC design shown in Figure 7 show a standard deviation below 2.5 dB by improving the performance of the basic prototype structure and satisfying all the defined requirements.

## 5. Conclusions

An RC consisting of new reflectors and mode stirrers has been proposed. It has an inner size that is approximately the same as or smaller than that of a commercial product. The main parameters for the reflectors and mode stirrers were determined through a logical approach based on standard deviation and eigenfrequency shift analysis by 3D simulations. The calculated and measured standard deviations for field

uniformity evaluation of the proposed RC have demonstrated that they clearly improve the standard deviation performance of its initial structure. In addition, the reasonable approach proposed in this paper for the RC design is very effective, and it has been verified that the design results accurately predict the main results obtained from the actual measurements. The measured results for the standard deviation of the proposed RC were found to satisfy all of the requirements defined in this paper. Therefore, it is expected that the performance of the proposed RC could be a very attractive facility for users who want to measure and evaluate the performance of commercial wireless terminals.

## Data Availability

The data used to support the findings of this study are available from the corresponding author upon request.

## Conflicts of Interest

The authors declare that they have no conflicts of interest.

## Acknowledgments

This work was supported by Institute for Information & Communications Technology Promotion grant funded by the Korea government (no. 2015-0-00855, Study on Measurement and Evaluation Technology based on Reverberation

Chamber, and no. 2017-0-00982, Development of System-Level Technology for Protection Design and Performance Evaluation against EMP). The authors are grateful to the staff of Korea Shield System Co., Ltd., the homepage of which is [www.kshieldsysltd.com](http://www.kshieldsysltd.com), for their help concerning the measurements in the reverberation chamber in this study.

## References

- [1] RWS-150029, “5G Vision and Enabling Technologies: ETRI Perspective,” ETRI, 3GPP RAN workshop on 5G, Phoenix, AZ, USA, 17<sup>th</sup>-18<sup>th</sup>, Sep. 2015.
- [2] ITU-R WP5D, “Technical Performance Requirements (New Recommendation ITU-R Key Performance Indicator),” June 2017.
- [3] “Reverberation Chamber Test Methods,” International Electrotechnical Commission Standard IEC 61000-4-21: 2011, Jan. 2011.
- [4] P.-S. Kildal, C. Carlsson, and J. Yang, “Measurement of free-space impedances of small antennas in reverberation chambers,” *Microwave and Optical Technology Letters*, vol. 32, no. 2, pp. 112–115, 2002.
- [5] P.-S. Kildal and K. Rosengren, “Correlation and capacity of MIMO systems and mutual coupling, radiation efficiency, and diversity gain of their antennas: simulations and measurements in a reverberation chamber,” *IEEE Communications Magazine*, vol. 42, no. 12, pp. 104–112, 2004.
- [6] A. Coates and A. P. Duffy, “Maximum working volume and minimum working frequency tradeoff in a reverberation chamber,” *IEEE Transactions on Electromagnetic Compatibility*, vol. 49, no. 3, pp. 719–722, 2007.
- [7] C. L. Zekios, P. C. Allilomes, M. T. Chryssomallis, and G. A. Kyriacou, “Finite element based eigenanalysis for the study of electrically large lossy cavities and reverberation chambers,” *Progress in Electromagnetics Research B*, vol. 61, no. 1, pp. 269–296, 2015.
- [8] H. Zhao and Z. Shen, “Memory-efficient modeling of reverberation chambers using hybrid recursive update discrete singular convolution-method of moments,” *IEEE Transactions on Antennas and Propagation*, vol. 60, no. 6, pp. 2781–2789, 2012.
- [9] C. Bruns and R. Vahldieck, “A closer look at reverberation chambers—3-D simulation and experimental verification,” *IEEE Transactions on Electromagnetic Compatibility*, vol. 47, no. 3, pp. 612–626, 2005.
- [10] G. Andrieu, F. Tristant, and A. Reineix, “Investigations about the use of aeronautical metallic halls containing apertures as mode-stirred reverberation chambers,” *IEEE Transactions on Electromagnetic Compatibility*, vol. 55, no. 1, pp. 13–20, 2013.
- [11] J. Clegg, A. C. Marvin, J. F. Dawson, and S. J. Porter, “Optimization of stirrer designs in a reverberation chamber,” *IEEE Transactions on Electromagnetic Compatibility*, vol. 47, no. 4, pp. 824–832, 2005.
- [12] A. Sorrentino, A. Gifuni, G. Ferrara, and M. Migliaccio, “Mode-stirred reverberating chamber autocorrelation function: Model, multifrequency measurements and applications,” *IET Science, Measurement & Technology*, vol. 9, no. 5, pp. 547–554, 2015.
- [13] “Electromagnetic compatibility of multimedia equipment—Emission requirements,” International Electrotechnical Commission Standard CISPR 32: 2015, March 2015.
- [14] “Electromagnetic compatibility of multimedia equipment—Immunity requirements,” International Electrotechnical Commission Standard CISPR 35: 2016, August 2016.
- [15] Reverberation chambers for MIMO OTA testing — BLUE-TEST.se, “Bluetest.se,” 2018, <https://bluetest.se>.
- [16] Accueil EN - siepel-www, “siepel-www,” 2018, <https://www.siepel.com>.
- [17] D. A. Hill, *Electromagnetic Field in Cavities: Deterministic and Statistical Theories*, John Wiley & Sons, Inc, New York, NY, USA, 2009.
- [18] M. L. Crawford and G. H. Koepke, “Design, evaluation, and use of a reverberation chamber for performing electromagnetic susceptibility/vulnerability measurements,” National Bureau of Standards NBS TN 1092, 1986.
- [19] FEKO simulation software, “Overview of FEKO,” <http://www.feko.info>.
- [20] M. Mehta and J. Johnson, *Architectural Acoustics Principles and Design*, Prentice Hall, 1999.
- [21] D. I. Wu and D. C. Chang, “The effect of an electrically large stirrer in a mode-stirred chamber,” *IEEE Transactions on Electromagnetic Compatibility*, vol. 31, no. 2, pp. 164–169, 1989.
- [22] CST MICROWAVE STUDIO software, “Overview of CST MICROWAVE STUDIO,” <http://www.cst.com>.
- [23] A. Kyei, D.-U. Sim, and Y.-B. Jung, “Compact log-periodic dipole array antenna with bandwidth-enhancement techniques for the low frequency band,” *IET Microwaves, Antennas & Propagation*, vol. 11, no. 5, pp. 711–717, 2017.